ISSN Application No. 21818

Journal of Mechanics and Structure

Volume No. 13

Issue No. 2

May - August 2025

ENRICHED PUBLICATIONS PVT.LTD

JE - 18,Gupta Colony, Khirki Extn,
Malviya Nagar, New Delhi - 110017.
E- Mail: info@enrichedpublication.com
Phone :- +91-8877340707

ISSN Application No. 21818

Journal of Mechanics and Structure

Aims and Scope

Journal of Mechanics and Structure is a journal which offers prompt publication of structural design; this journal publishes peer-reviewed technical papers on state-of-the-art topics and future developments of the profession. Engineers, consultants, and professors detail the physical properties of engineering materials (such as steel, concrete, and wood), develop methods of analysis, and examine the relative merits of various types of structures and methods of fabrication. Subjects include the design, erection, and safety of structures ranging from bridge to transmission towers and tall buildings; technical information on outstanding, innovative, and unique projects; and the impact of natural disasters and recommendations for damage mitigation.

ISSN Application No. 21818

Journal of Mechanics and Structure

ISSN Application No. 21818

Journal of Mechanics and Structure

(Volume No. 13, Issue No. 2, May - August 2025)

Contents

ISSN Application No. 21818

ON THE DETACHMENT OF PATCHED PANELS UNDER THERMOMECHANICAL LOADING

WILLIAM J. BOTTEGA AND PAMELA M. CARABETTA

The problem of propagation of interfacial failure in patched panels subjected to temperature change and transverse pressure is formulated from first principles as a propagating boundaries problem in the calculus of variations. This is done for both cylindrical and flat structures simultaneously. An appropriate geometrically nonlinear thin structure theory is incorporated for each of the primitive structures (base panel and patch) individually. The variational principle yields the constitutive equations of the composite structure within the patched region and an adjacent contact zone, the corresponding equations of motion within each region of the structure, and the associated matching and boundary conditions for the structure. In addition, the transversality conditions associated with the propagating boundaries of the contact zone and bond zone are obtained directly, the latter giving rise to the energy release rates in self-consistent functional form for configurations in which a contact zone is present as well as when it is absent. A structural scale decomposition of the energy release rates is established by advancing the decomposition introduced in W. J. Bottega, Int. J. Fract. 122 (2003), 89–100, to include the effects of temperature. The formulation is utilized to examine the behavior of several representative structures and loadings. These include debonding of unfettered patched structures subjected to temperature change, the effects of temperature on the detachment of beam-plates and arch-shells subjected to three-point loading, and the influence of temperature on damage propagation in patched beam-plates, with both hinged-free and clamped-free support conditions, subjected to transverse pressure. Numerical simulations based on closed form analytical solutions reveal critical phenomena and features of the evolving composite structure. It is shown that temperature change significantly influences critical behavior.

1. Introduction

The role of patched structures has expanded in modern engineering, as uses range from large-scale structural repair to sensors and actuators to small-scale electronic systems. Detachment of the constituent structures is thus an issue of concern as it may influence the effectiveness and integrity of the composite structure. By its nature, the structure possesses a geometrical discontinuity at the edge of the patch. Stress concentrations within the base structure-patch interface at this location (see, for example, [Wang and Rose 2000]) can lead to the initiation of debonding.1 As a result, a primary mode of failure of such structures under various loading conditions is edge debonding and its propagation. The characterization of edge debonding is thus of critical importance in preserving the useful life of this type of structure. The structures of interest are typically subjected to temperature variations from the reference state. Such temperature changes can influence the onset and extent of damage in these structures. In this light, Duong and Yu [2002] examined the thermal effects of curing on the stress intensity factor for an octahedralshaped composite repair patch bonded to a cracked rectangular plate. A general expression for the stress distribution was calculated analytically by adopting an "equivalent inclusion method" attributed to Rose [1981], assuming a second order polynomial distribution for the strains. The solution is used to analyze a sample problem and is compared with results using FEM. Related work includes that of Wang et al. [2000], who analyzed thermally-induced residual stresses due to curing in plates with circular patches. Structures were restricted to those with identical coaxial circular patches on the upper and lower faces of the plate so as to eliminate bending as an issue. Moore [2005], with an eye towards avoiding detachment of layers due to uniform temperature change, developed an analytical beam type model in the spirit of Timoshenko [1925] to describe peeling of a composite laminate under thermal load. In this context, he calculated the peeling moment that arises from the peel stress at any interface of the structure due to an applied uniform temperature change from the curing temperature. This was done via a force balance approach, where a decomposition of the moments into thermal and mechanical parts was utilized. The results were then applied to three- and four-layer beams. In a similar vein, Toya et al. [2005] employed a force balance based on classical beam theory to evaluate the energy release rate for a bilayer beam possessing an edge delamination when the structure is subjected to different temperatures at the top surface, bottom surface, and interface. They characterized the mode mix using a small-scale decomposition attributed to Toya [1992] which utilizes complex stress intensity factors and the crack closure method to characterize the energy release rate.

In related work, Karlsson and Bottega [2000a; 2000b] studied the effects of a uniform temperature f ield applied to a patched plate, where the base structure is fixed at both ends with regard to in-plane translation. In that work, the authors uncovered and explained the instability phenomenon they refer to as "slingshot buckling", whereby, at a critical temperature, the structure "slings" dynamically from an equilibrium configuration possessing deflections in one direction to another equilibrium configuration with deflections in the opposite direction. Rutgerson and Bottega [2002] examined the thermo-elastic buckling of multilayer shell segments. In that study, the layered shells are subjected to an applied transverse pressure in addition to a uniform temperature field. The nonlinear analysis therein showed "slingshot" buckling to occur for thermal loading of these types of structures as well, and at temperatures well below the conventional "limit point" (see also [Rutgerson and Bottega 2004]). The findings on slingshot buckling have since been unified [Bottega 2006]. It is concluded that this type of buckling is inherent to many types of composite structures and occurs due to competing mechanical and thermal elements of the loading. Most recently, Carabetta and Bottega [2008] studied the effects of geometric nonlinearities on the debonding of patched beam-plates subjected to transverse pressure. Analyses using both nonlinear and linearized models were conducted and compared. Significant discrepancies were seen to occur between behaviors predicted by the two models, both with respect to the onset of damage propagation and with regard to the stability of the process and to pre-growth behavior, demonstrating the influence of geometric nonlinearities on the phenomena of interest.

In the present work, we examine debonding of both initially flat and initially curved patched structures under uniform temperature alone and in consort with transverse pressure and three-point loading. Toward this end, the problem of propagation of interfacial debonds in patched panels subjected to temperature change and transverse pressure is formulated from first principles as a propagating boundaries problem in the calculus of variations, in the spirit of [Bottega 1995; Bottega and Loia 1996; 1997; Bottega and Karlsson 1999; Karlsson and Bottega 1999a; 1999b], where various issues, configurations, and loading conditions were studied. For the present study, temperature is accounted for. A region of sliding contact adjacent to the intact region is also considered, and the boundary of the intact region as well as the boundary between the contact zone and a region of separation of the patch and base panel are each allowed to vary along with the displacements within each region. This is done for both cylindrical and flat structures simultaneously. An appropriate geometrically nonlinear thin structure theory is incorporated for each of the primitive structures (base panel and patch) individually. The variational principle then yields the constitutive equations of the composite structure within the patched region and an adjacent contact zone, the corresponding equations of motion within each region of the structure, and the associated matching and boundary conditions for the structure. In addition, the transversality conditions associated with the propagating boundaries of the contact zone and bond zone are obtained directly, the latter giving rise to the energy release rates in self-consistent functional form for configurations in which a contact zone is present as well as when it is not. A structural scale decomposition of the energy release rates is established by advancing the decomposition of [Bottega 2003] to include the effects of temperature. The formulation is then utilized to examine the behavior of several representative structures and loadings. These include debonding of unfettered patched structures subjected to temperature change, the effects of temperature on the detachment of beam-plates and arch-shells subjected to three-point loading, and the influence of temperature on damage propagation in patched beam-plates, with both hinged-free and clamped-free support conditions, subjected to transverse pressure. (The latter is shown in Figure 1.) Numerical simulations based on exact analytical solutions to the aforementioned formulation are performed, the results of which are presented in load-damage size space. Interpretation of the corresponding “growth paths” admits characterization of the separation behavior of the evolving composite structure. It is shown that temperature change significantly influences critical behavior.

2. Formulation

Consider a thin structure (flat or cylindrical) comprised of a base panel (plate or shell) of normalized half-span L to which a patch of half-span $L_p \leq L$ is adhered over the region $S_1 : s \in [0, a]$ (shown in Figure 2 for a flat panel). The coordinate s runs parallel to the reference surface and originates at the centerspan of the structure, as shown. Further, let us consider the debonded portion of the patch to

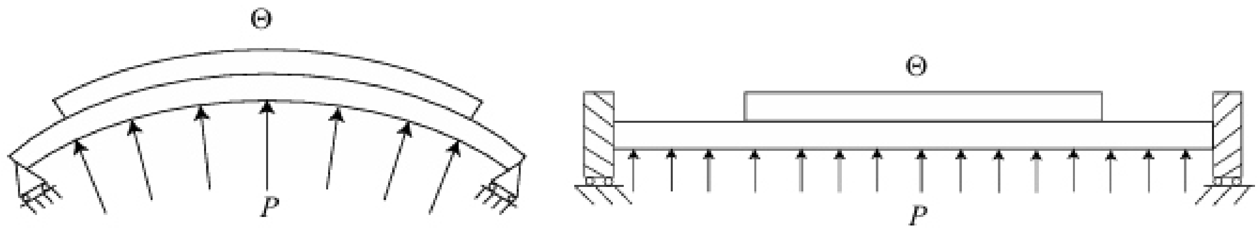

Figure 1. Patched structures subjected to transverse pressure and uniform temperature field. Left: cylindrical panel (arch-shell) with hinged-free supports. Right: flat panel (beam-plate) with clamped-free supports.

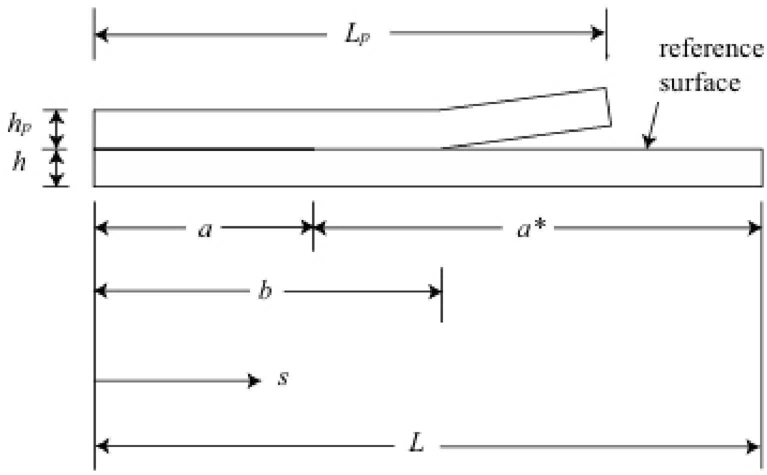

Figure 2. Dimensionless half-span of structure (shown for flat panel).

maintain sliding contact over the region $S_2 : s \in [a, b]$ adjacent to the bonded region, while a portion of the patch defined on $S_3 : s \in [b, L]$ is lifted away from the base structure. These three regions will be referred to as the "bond zone", "contact zone", and "lift zone", respectively. The domain of definition of the portion of the patch within the lift zone is $S_{3p} : s \in [b, L_p]$ such that $S_{3p} \subset S_3$. When referring to the portion of the patch in region S_3 it will be understood that the corresponding subregion is indicated. At this point, let us also define the "conjugate bond zone" $a^* \equiv L - a$ as indicated in the figure. We shall be interested in examining the evolution and response of the composite structure when it is subjected to a uniform temperature increase, Θ, above some reference temperature. In what follows, all length scales are normalized with respect to the dimensional half-span $\bar{L}$ (radius $\bar{R}$) of the undeformed plate (shell) structure, and the common surface or interface between the patch and base panel, and its extension, will be used as the reference surface. The temperature change, Θ, is normalized with respect to the reference temperature (and the coefficient of thermal expansion of the base structure). The corresponding relations for the normalized (centerline) membrane strains $e_i(s)$ and $e_{pi}(s)$ and the normalized curvature changes $\kappa_i(s)$ and $\kappa_{pi}(s)$ for the base structure and the patch in each region are thus given by

$$
\begin{aligned}
e_i &= u_i' - k w_i + \tfrac{1}{2} {w_i'}^2, & \kappa_i &= w_i'' + k w_i, & (s \in S_i) \\
e_{pi} &= u_{pi}' - k w_{pi} + \tfrac{1}{2} {w_{pi}'}^2, & \kappa_{pi} &= w_{pi}'' + k w_{pi}, & (s \in S_{ip})
\end{aligned} \tag{1}
$$

where $k = 0$ corresponds to the plate and $k = 1$ corresponds to the shell, and the variables are defined as follows: $u_i = u_i(s)$ (positive in the direction of increasing s) and $w_i = w_i(s)$ (positive downward/inward), respectively, correspond to the axial (circumferential) and transverse (radial) displacements of the centerline of the base panel in region S_i, and $u_{pi} = u_{pi}(s)$ and $w_{pi} = w_{pi}(s)$ correspond to the analogous displacements of the centerline of the patch. The primes indicate total differentiation with respect to s.

The displacements $u_i(s)$ and $u_{pi}(s)$, and the membrane strains $e_i(s)$ and $e_{pi}(s)$ of the substructure surface, by the relations

$$
\begin{aligned}
u_i^* &= u_i + \tfrac{1}{2} h w_i', & u_{pi}^* &= u_{pi} - \tfrac{1}{2} h_p w_{pi}' & (i = 1, 2, 3) \\
e_i^* &= e_i + \tfrac{1}{2} h \kappa_i, & e_{pi}^* &= e_{pi} - \tfrac{1}{2} h_p \kappa_{pi} & (i = 1, 2, 3)
\end{aligned}
$$

where $h \ll 1$ is the normalized thickness of the base panel and $h_p \ll 1$ is that of the patch. At this point let us also introduce the normalized membrane stiffness, C, and bending stiffness, D, of the base panel and the corresponding normalized membrane and bending stiffnesses, C_p and D_p, of the patch. The normalization of the stiffnesses of the primitive structures is based on the bending stiffness of the base panel and the half-span $\bar{L}$ (radius $\bar{R}$) of the system in the undeformed configuration. Hence,

$$
C = 12/h^2, \qquad D = 1, \qquad C_p = C E_0 h_0, \qquad D_p = E_0 {h_0}^3, \tag{2}
$$

where $h_0 = h_p/h$, and

$$
E_0 = \bar{E}_p/\bar{E} \quad \text{(plane stress)} \qquad \text{or} \qquad E_0 = \frac{\bar{E}_p/(1-\nu_p^2)}{\bar{E}/(1-\nu^2)} \quad \text{(plane strain)},
$$

where $\bar{E}$ and $\bar{E}_p$ correspond to the (dimensional) elastic moduli of the base panel and patch, respectively, and ν and ν_p are the associated Poisson's ratios.

The nondimensional coefficients of thermal expansion of the base structure and patch, α^0 and α_p^0, respectively, are the products of the dimensional coefficients and the reference temperature. We correspondingly define, for the present formulation, the augmented coefficients α and α_p such that

$$
\begin{aligned}
\alpha &= \alpha^0 & &\text{and} & \alpha_p &= \alpha_p^0 & &\text{(plane stress)}, \\
\alpha &= (1+\nu)\alpha^0 & &\text{and} & \alpha_p &= (1+\nu_p)\alpha_p^0 & &\text{(plane strain)}.
\end{aligned} \tag{3}
$$

We next introduce the normalized temperature scale, Θ, such that

$$
\tilde{\Theta} = \alpha \Theta = \alpha \frac{\bar{\Theta} - \bar{\Theta}_0}{\bar{\Theta}_0}, \tag{4}
$$

where $\bar{\Theta}$ is the dimensional temperature and $\bar{\Theta}_0$ is a reference temperature.

Paralleling the developments in [Bottega 1995], we next formulate an energy functional in terms of (i) the strain energies of each of the individual segments of both the base panel and patch, independently, and expressed in terms of the reference surface variables, (ii) the work done by the applied loading for each case of interest, (iii) constraint functionals which match the transverse displacements in the contact zone and both the transverse (radial) and in-plane (circumferential) displacements in the bond zone[2], and (iv) a delamination energy functional corresponding to the energy required to create a unit length of new disbond. To complete the formulation, we include a thermal energy functional. We thus formulate the energy functional Π as follows:

$$\Pi = \sum_{i=1}^{3} \left(U_B^{(i)} + U_{Bp}^{(i)} + U_M^{(i)} + U_{Mp}^{(i)} + U_T^{(i)} + U_{Tp}^{(i)} \right) - \Lambda - \mathcal{W} + \Gamma, \tag{5}$$

where

$$U_B^{(i)} = \int_{S_i} \tfrac{1}{2} D \kappa_i^2 \, ds, \quad \text{and} \quad U_{Bp}^{(i)} = \int_{S_i} \tfrac{1}{2} D_p {\kappa_{pi}}^2 \, ds \quad (i = 1, 2, 3), \tag{6}$$

correspond to the bending energies in the base panel and the patch in region S_i, while

$$U_M^{(i)} = \int_{S_i} \tfrac{1}{2} C (e_i - \alpha \Theta)^2 \, ds \quad \text{and} \quad U_{Mp}^{(i)} = \int_{S_i} \tfrac{1}{2} C_p (e_{pi} - \alpha_p \Theta)^2 \, ds \quad (i = 1, 2, 3)$$

are the corresponding stretching energies of the base panel and the patch. Further,

$$U_T^{(i)} = \int_{S_i} \left(c_\sigma - (1 + \Theta) c_e \right) \Theta \, ds, \quad U_{Tp}^{(i)} = \int_{S_i} \left(c_{\sigma p} - (1 + \Theta) c_{ep} \right) \Theta \, ds$$

represent the "thermal energies" of the base structure and the patch, respectively, such that the total bracketed expression in (5) corresponds to the (Helmholtz) free energy of the structure, and Θ is the normalized temperature change. The quantities c_σ, c_e ($c_{\sigma p}$, c_{ep}) correspond to the normalized specific heats of the base structure (patch) for constant stress and constant deformation, respectively. These terms are included for completeness. We remark that since we shall consider the normalized temperature change, Θ, as prescribed, the variation of these functionals will vanish identically. (The contribution of the convective type terms of these particular functionals for a given region, associated with the propagation of the interior boundaries $s = a$ and $s = b$, will cancel and hence will have no contribution to the overall variation of Π as well.) Further, if the process is considered to be adiabatic, these terms will vanish identically as the free energy goes to internal energy and may be interpreted as the adiabatic work given by the first four functionals.

The functional Λ appearing in (5) is a constraint functional given by

$$\Lambda = \sum_{i=1}^{2} \int_{S_i} \sigma_i (w_{pi} - w_i) \, ds + \int_{S_i} \tau (u_{p1}^* - u_1^*) \, ds,$$

where σ_1, σ_2 and τ are Lagrange multipliers (and $\sigma_2 < 0$). Further,

$$\mathcal{W} = -\sum_{i=1}^{3} \int_{S_i} p w_i \, ds$$

is the work done by the applied pressure, and

$$\Gamma = 2\gamma (a^* - a_0^*)$$

is the delamination energy[3], where

$$a^* = L - a$$

is the conjugate bond zone half-length as defined earlier, a_0^* corresponds to some initial value of a^*, and γ is the normalized bond energy (bond strength).

The normalized bond energy, γ, is related to its dimensional counterpart, $\bar{\gamma}$, by the relations

$$\gamma = \bar{\gamma} \bar{\ell}^2 / \bar{D},$$

where $\bar{D}$ is the dimensional bending stiffness of the base panel and $\bar{\ell} = \bar{L}, \bar{R}$ (plate, shell). Likewise, the normalized interfacial stresses σ_1,σ_2, and τ (the Lagrange multipliers), and the normalized applied pressure p, are related to their dimensional counterparts $\bar{\sigma}_1, \bar{\sigma}_2, \bar{\tau}$, and $\bar{p}$, respectively, by

$$\sigma_i = \bar{\sigma}_i \bar{\ell}^3/\bar{D} \quad (i = 1, 2), \qquad \tau = \bar{\tau}\bar{\ell}^3/\bar{D}, \, p = \bar{p}\bar{\ell}^3/\bar{D}.$$

We next invoke the principle of stationary potential energy which, in the present context, is stated as

$$\delta\Pi = 0.$$

Taking the appropriate variations, allowing the interior boundaries a and b to vary along with the displacements, we arrive at the corresponding differential equations, boundary and matching conditions, and *transversality conditions* (the conditions that establish values of the "moveable" interior boundaries a and b to be found as part of the solution, together with the associated displacement field, which correspond to equilibrium conditions of the evolving structure). After eliminating the Lagrange multipliers from the resulting equations, we arrive at a self-consistent set of equations and conditions (including the energy release rates) for the evolving composite structure. We thus have

$$M_i^{*\prime\prime} + k(M_i^* - N_i^*) - (N_i^* w_i^{*\prime})' = -p, \qquad N_i^{*\prime} = 0 \qquad (s \in S_i;\ i = 1, 2) \tag{7}$$

$$M_3'' + k(M_3 - N_3) - (N_3 w_3')' = -p, \qquad N_3' = 0 \qquad (s \in S_3) \tag{8}$$

$$M_{p3}'' + k(M_{p3} - N_{p3}) - (N_{p3} w_{p3}')' = 0, \qquad N_{p3}' = 0 \qquad (s \in S_{3p}) \tag{9}$$

with

$$\begin{aligned} w_i^*(s) &\equiv w_i(s) = w_{pi}(s) \qquad (s \in S_i;\ i = 1, 2), \\ \kappa_i^*(s) &\equiv \kappa_i(s) = \kappa_{pi}(s) \qquad (s \in S_i;\ i = 1, 2), \\ u_1^*(s) &= u_{p1}^*(s) \qquad (s \in S_1). \end{aligned}$$

Here

$$N_i(s) = C[e_i(s) - \alpha\Theta], \qquad N_{pi}(s) = C_p[e_{pi}(s) - \alpha_p\Theta] \qquad (i = 1, 2, 3)$$

are the normalized resultant membrane forces acting on a cross section of the base panel and patch within region S_i $(i = 1, 2, 3)$;

$$N_1^*(s) = C^* e_1^*(s) + B^*\kappa_1^*(s) - n^*\Theta = C^*[e_1^*(s) - \alpha^*\Theta] + B^*[\kappa_1^*(s) - \beta^*\Theta], \tag{10}$$

$$\begin{aligned} M_1^*(s) = A^*\kappa_1^*(s) + B^* e_1^*(s) - \mu^*\Theta &= A^*[\kappa_1^*(s) - \beta^*\Theta] + B^*[e_1^*(s) - \alpha^*\Theta] \\ &= D^*[\kappa_1^*(s) - \beta^*\Theta] + \rho^* N_1^*, \end{aligned} \tag{11}$$

respectively, correspond to the normalized membrane force and normalized bending moment acting on a cross section of the bonded portion of the composite structure;

$$N_2^*(s) = N_2 + N_{p2} \quad \text{and} \quad M_2^*(s) = D_c\kappa_2^*(s) + \tfrac{1}{2}(h_p N_{p2} - h N_2) \tag{12}$$

correspond to the normalized resultant membrane force and bending moment for the debonded portion of the composite structure within the contact zone; and

$$M_3(s) = D\kappa_3(s) - \tfrac{1}{2}hN_3 \quad \text{and} \quad M_{p3}(s) = D_p\kappa_{p3}(s) + \tfrac{1}{2}h_p N_3,$$

correspond to the normalized bending moments in the base panel and patch segments within the region of separation (or lift zone).

The stiffnesses and thermal coefficients of the composite structure defined by (10), (11), and (12) are found in terms of the stiffnesses and thicknesses of the primitive substructures as

$$\begin{aligned} A^* &= D + D_p + (h/2)^2 C + (h_p/2)^2 C_p, \qquad & B^* &= (h_p/2)C_p - (h/2)C, \\ C^* &= C + C_p, & D^* &= A^* - \rho^* B^* = D_c + (h^*/2)^2 C_s, \\ \alpha^* &= \alpha_1 - \rho^*\beta^*, & \beta^* &= m^*/D^*, \end{aligned} \tag{13}$$

where

$$\begin{aligned} &\rho^* = B^*/C^*, \qquad D_c = D + D_p, \qquad h^* = h + h_p, \qquad C_s = CC_p/C^*, \\ &\mu^* = \tfrac{1}{2}h_p C_p \alpha_p - \tfrac{1}{2}hC\alpha, \quad n^* = C_p\alpha_p + C\alpha, \quad m^* = \mu^* - \rho^* n^*, \quad \alpha_1 = n^*/C^*. \end{aligned} \tag{14}$$

The quantity ρ^* is seen to give the transverse (radial) location of the centroid of the composite structure with respect to the reference surface, D_c is the bending stiffness of the debonded segment of the composite structure in the contact zone, $h^* \ll 1$ is the normalized thickness of the composite structure and C_s is an effective (series) membrane stiffness. In addition, the parameters α^* and β^* are seen to correspond to the thermal expansion coefficients of the intact portion of the composite structure and correspond to the thermally-induced membrane strain at the reference surface and the associated curvature change, respectively, per unit normalized temperature change for a free unloaded structure The thermal expansion coefficient α_1 is seen to be the corresponding strain per unit temperature at the centroid of the intact segment of an unloaded composite structure.

The associated boundary and matching conditions are obtained similarly:

$$u_1^*(0) = 0, \qquad w_1^{*\prime}(0) = 0, \qquad [M_1^{*\prime} - N_1^* w_1^{*\prime}]_{s=0} = 0 \qquad \text{(symmetric deformation)} \tag{15a}$$

$$u_0^*(0) \equiv u_1^*(0) + \rho^* w_1^{*\prime}(0) = 0, \qquad w_1^*(0) = 0, \quad \kappa_1^*(0) = 0 \qquad \text{(antisymmetric deformation)} \tag{15b}$$

$$u_1^*(a) = u_2^*(a) = u_{p2}^*(a), \qquad N_1^*(a) = N_2^*(a) \qquad (a = a_L, -a_R) \tag{16}$$

$$w_1^*(a) = w_2^*(a), \qquad w_1^{*\prime}(a) = w_2^{*\prime}(a) \qquad (a = a_L, -a_R) \tag{17}$$

$$[M_1^{*\prime} - N_1^* w_1^{*\prime}]_{s=a} = [M_2^{*\prime} - N_2^* w_2^{*\prime}]_{s=a}, \quad M_1^*(a) = M_2^*(a) \qquad (a = a_L, -a_R) \tag{18}$$

$$u_2^*(b) = u_3^*(b), \qquad N_2(b) = N_3(b) \qquad (b = b_L, -b_R) \tag{19}$$

$$u_{p2}^*(b) = u_{p3}^*(b), \qquad N_{p2}(b) = N_{p3}(b) \qquad (b = b_L, -b_R) \tag{20}$$

$$w_2^*(b) = w_3(b) = w_{p3}(b), \qquad w_2^{*\prime}(b) = w_3'(b) = w_{p3}'(b) \qquad (b = b_L, -b_R) \tag{21}$$

$$M_2^*(b) = M_3(b) + M_{p3}(b) \qquad (b = b_L, -b_R) \tag{22}$$

$$[M_2^{*\prime} - N_2^* w_2^{*\prime}]_{s=b} = [M_3' - N_3 w_3']_{s=b} + [M_{p3}' - N_{p3} w_{p3}']_{s=b} \qquad (b = b_L, -b_R) \tag{23}$$

$$N_{p3}(\pm L_p) = \kappa_{p3}(\pm L_p) = [M_{p3}' - N_{p3} w_{p3}']_{s=\pm L_p} = 0 \tag{24}$$

$$u_3(\pm L) = 0 \qquad \text{or} \qquad N_3(\pm L) = 0 \tag{25}$$

$$w_3'(\pm L) = 0 \qquad \text{or} \qquad \kappa_3(\pm L) = 0 \tag{26}$$

$$w_3(\pm L) = 0 \tag{27}$$

The transversality condition for the propagating bond zone boundaries, $a = a_L, -a_R$, with the associated propagating contact zone boundaries, $b = b_L, -b_R$, take the following forms depending upon the presence or absence of a contact zone:

$$\mathcal{G}^{(2)}\{a\} = 2\gamma \quad (b > a), \qquad \mathcal{G}^{(3)}\{a\} = 2\gamma \quad (b = a). \tag{28}$$

In these expressions, the quantities

$$\mathcal{G}^{(i)}\{a\} \equiv G_{MM}^{(i)} + G_{MT}^{(i)} + G_{TM}^{(i)} + G_{TT} \quad (i = 2, 3)$$

are the energy release rates, whose components are given by

$$G_{MM}^{(2)} \equiv \left[\tfrac{1}{2}D_c\kappa_2^{*2} + \tfrac{1}{2C}N_2^2 + \tfrac{1}{2C_p}N_{p2}{}^2\right]_{s=a} - \left[\tfrac{1}{2}D^*(\kappa_1^* - \beta^*\Theta)^2 + \tfrac{1}{2C^*}N_1^{*2}\right]_{s=a}, \tag{29}$$

$$G_{MM}^{(3)} \equiv \left[\tfrac{1}{2}D\kappa_3{}^2 + \tfrac{1}{2}D_p\kappa_{p3}{}^2 + \tfrac{1}{2C}N_3^2 + \tfrac{1}{2C_p}N_{p3}{}^2\right]_{s=a} - \left[\tfrac{1}{2}D^*(\kappa_1^* - \beta^*\Theta)^2 + \tfrac{1}{2C^*}N_1^{*2}\right]_{s=a}, \tag{30}$$

$$G_{MT}^{(i)} \equiv \left[\tfrac{1}{2}N_i e_T + \tfrac{1}{2}N_{pi}e_{pT}\right]_{s=a} - \left[\tfrac{1}{2}N_1^* e_T^* + \tfrac{1}{2}M_1^*\kappa_T^*\right]_{s=a} \quad (i = 2, 3), \tag{31}$$

$$G_{TM}^{(i)} \equiv \left[\tfrac{1}{2}N_T e_{pi}^{\circ} + \tfrac{1}{2}N_{pT}e_i^{\circ}\right]_{s=a} - \left[\tfrac{1}{2}N_T^* e_0^* + \tfrac{1}{2}M_T^*\kappa_0^*\right]_{s=a} \quad (i = 2, 3), \tag{32}$$

$$G_{TT} \equiv \left[\tfrac{1}{2}N_T e_T + \tfrac{1}{2}N_{pT}e_{pT}\right]_{s=a} - \left[\tfrac{1}{2}N_T^* e_T^* + \tfrac{1}{2}M_T^*\kappa_T^*\right]_{s=a}, \tag{33}$$

where the following measures have been introduced:

$$e_i^{\circ} \equiv e_i - \alpha\Theta, \qquad e_{pi}^{\circ} \equiv e_{pi} - \alpha_p\Theta \qquad (i = 2, 3), \tag{34}$$

$$e_T \equiv \alpha\Theta, \qquad e_{pT} = \alpha_p\Theta, \qquad N_T = C\alpha\Theta, \qquad N_{pT} = C_p\alpha_p\Theta, \tag{35}$$

$$e_0^* \equiv e_1^* - \alpha^*\Theta, \qquad \kappa_0^* \equiv \kappa_1^* - \beta^*\Theta, \qquad e_T^* \equiv \alpha^*\Theta, \qquad \kappa_T^* \equiv \beta^*\Theta, \tag{36}$$

$$N_T^* \equiv C^*\alpha_1\Theta = C^*e_T^* + B^*\kappa_T^*, \qquad M_T^* \equiv \mu^*\Theta = D^*\kappa_T^* + \rho^* N_T^*. \tag{37}$$

The conditions established by those equations suggest the following *delamination criterion*:

If, for some initial value $a = a_0$ of the bond zone boundary, the state of the structure is such that $\mathcal{G}^{(i)}\{a\} \geq 2\gamma$, then delamination growth occurs and the system evolves (a decreases, a^* increases) in such a way that the corresponding equality in (28) is satisfied. If $\mathcal{G}^{(i)}\{a\} < 2\gamma$, delamination growth does not occur.

For a propagating contact zone ($s = b$), the associated transversality condition reduces to the form

$$\kappa_2^*(b) = \kappa_3(b) = \kappa_{p3}(b) \qquad (b = b_L < L_p, -b_R > -L_p), \tag{38}$$

to which we add the qualification

$$\kappa_3(b^+) > \kappa_{p3}(b^+) \tag{39}$$

in order to prohibit penetration of the base panel and patch for $s \in S_{3p}$. It is thus seen that such a boundary is defined by the point where the curvature changes of the respective segments of the structure are continuous.

The equations introduced so far define the class of problems of interest.

The boundary conditions (24), together with (9), indicate that the "flap" (the segment of the debonded portion of the patch that is lifted away from the base structure) is unloaded, and hence that

$$N_{p3}(s) = \kappa_{p3}(s) = M'_{p3}(s) = 0 \qquad (s \in S_{3p}). \tag{40}$$

Further, integration of $(7)_2$ and $(8)_2$, imposition of the associated matching conditions stated by $(16)_3$, $(19)_2$, and $(20)_2$, and incorporation of $(40)_1$ yield the results that

$$N_1^* = N_2 = N_3 = N_0 = \text{ constant}, \qquad N_{p2} = 0. \tag{41}$$

The remaining equations are modified accordingly, with the transversality conditions stated in (28) and (38) taking the forms

$$\left.\begin{array}{l} \mathcal{G}^{(2)}\{a\} \longrightarrow \left[\tfrac{1}{2}D_c\kappa_2^{*2} - \tfrac{1}{2}D^*\kappa_1^{*2} + \tfrac{1}{2}N_0^2/C_e + N_0(\alpha - \alpha_1)\Theta + \tfrac{1}{2}\eta\Theta^2\right]_{s=a} = 2\gamma \quad (b > a) \\ \mathcal{G}^{(3)}\{a\} \longrightarrow \left[\tfrac{1}{2}D\kappa_3^2 - \tfrac{1}{2}D^*\kappa_1^{*2} + \tfrac{1}{2}N_0^2/C_e + N_0(\alpha - \alpha_1)\Theta + \tfrac{1}{2}\eta\Theta^2\right]_{s=a} = 2\gamma \quad (b = a) \end{array}\right\} \tag{42}$$

and

$$\kappa_2^*(b) = \kappa_3(b) = 0, \qquad \kappa_3(b^+) > 0 \qquad (b < L_p), \tag{43}$$

where

$$\frac{1}{C_e} \equiv \frac{C_p/C}{C^*}, \qquad \eta \equiv \alpha^2 C + \alpha_p^2 C_p - \alpha_1^2 C^*. \tag{44}$$

It may be seen from (43) that a propagating or intermediate contact zone boundary may occur only if conditions are such that an inflection point or pseudo-inflection point occurs on the interval $a < s < L_p$ If not, the system will possess either a full contact zone ($b = L_p$), or no contact zone ($b = a$). For the former case, the lifted segment of the flap (region S_{3p}) will not exist and the condition

$$\kappa_2(a^+) < 0 \qquad (b = L_p) \tag{45}$$

must be satisfied.

Integrating the strain-displacement relations and imposing the boundary and matching conditions for the axial (circumferential) displacements results in the following *integrability condition*:

$$u_3(L) - u_0 = N_0\left(\frac{a^*}{C} + \frac{a}{C^*}\right) + (a^*\alpha + a\alpha_1)\Theta - \left(\frac{h}{2} + \rho^*\right)w'(a) + \sum_{i=1}^{3}\int_{S_i}\left(k(1-\rho^*\delta_{i1})w_i - \tfrac{1}{2}w_i'^2\right)ds, \tag{46}$$

where

$$u_0 \equiv [u_1{}^* + \rho^* w_1']_{s=0} \tag{47}$$

is the axial (circumferential) deflection of the neutral surface of the composite structure at the origin, and δ_{ij} is Kronecker's delta. The counterparts of $(7)_1$ and $(8)_1$ and the corresponding boundary and matching conditions obtained upon substitution of (38)–(40), together with the transversality conditions stated in (42) and (43), and the integrability condition, (46), transform the problem statement into a *mixed formulation* in terms of the transverse displacements $w_i(s)$ ($i = 1, 2, 3$), the membrane force N_0, and the moving boundaries a and b.

3. Delamination mode mix

The bond energy (that is, interfacial toughness) is generally dependent upon the mix of "delamination modes". To assess this influence for the system under consideration, we adopt the structural scale decomposition of the energy release rate for long thin-layered structures established by Bottega [2003] and extend it to include the thermal effects considered for the present study. In the aforementioned reference, the decomposition is established for a general structure and is then applied to selected specific structural configurations, including patched structures. The presence of a contact zone is taken to imply pure mode-II delamination, while the absence of contact is considered to (generally) imply mixed modeI and mode-II delamination. The mixed mode decomposition is based on the energy release rates for contact and no contact together with a "curvature of contact" defined therein. The decomposition for the present problem follows directly from the aforementioned reference and the inclusion of the thermal terms as follows. The last three terms of the energy release rates given by (42) are seen to constitute the relative thermomechanical membrane energy at the bond zone boundary and thus contribute to the mode-II delamination energy release rate. Incorporating the last two of these (the first is already included in the original) into the resulting partitioning of the energy release rate for the class of patched structures currently under consideration [Bottega 2003, Section 5.3] gives the following decomposition for the present structure:

$$G_I = \tfrac{1}{2} D_I \kappa_3^2(a), \quad G_{II} = \tfrac{1}{2}\left[D_{II}\kappa_3^2 - D^*\kappa_1^{*2}\right]_{x=a} + \left(\tfrac{1}{2}N_0^2/C_e + N_0(\alpha-\alpha_1)\Theta + \tfrac{1}{2}\eta\Theta^2\right), \tag{48}$$

where G_I and G_{II} are, respectively, the mode-I (opening mode) and mode-II (sliding mode) energy release rates, and

$$D_I = D_p D/D_c, \qquad D_{II} = D^2/D_c. \tag{49}$$

The mode ratio G_{II}/G_I can be readily evaluated using (48) for any configuration determined by the formulation established in this section.

4. Analysis

The mixed formulation presented in the previous section admits analytical solutions to within a numer ically determined membrane force parameter. (7)–(9) together with the matching conditions, (16)–(23), and the pertinent boundary conditions of (15) and (24)–(27), can be readily solved to yield analytical solutions for the transverse displacement in terms of the membrane force. For given material and geometric properties, the membrane force can be evaluated numerically by substituting the corresponding analytical solutions into the integrability condition, (46), and finding roots (values of N0) of the resulting transcendental equation using root solving techniques. Each root is associated with an equilibrium configuration of the evolving structure for given values of the temperature, pressure, damage size, and length of the contact zone. Once obtained, these values can be substituted back into the solution for the transverse deflection and the result then substituted into the transversality conditions (42) to generate the delamination growth paths for the evolving structure.4 The onset, stability, and extent of propagation can be assessed from these paths. (As a special case, it may be noted from (25)2 and (41)1 that when the edges of the base structure are free to translate in the axial (circumferential) direction, the uniform membrane force vanishes identically .N0 0/. For this case, the analytical solutions may be obtained by direct integration, and substituted into the transversality condition. The corresponding integrability condition will then simply yield the axial (circumferential) displacement of the edge of the base structure.) Finally, the issue of a propagating contact zone may be examined by evaluating a solution for a given value of b (associated with a given value of a) and checking to insure that the resulting displacements satisfy the kinematic inequality (43)2. The energy release rates for configurations with valid contact zones may then be plotted as a function of the contact zone boundary coordinate, b, for selected values of the bond zone size, a. (It was shown in [Bottega 1995] that for a certain class of problems a propagating contact zone is not possible. Rather, if contact of the detached segment of the patch with the base structure is present it is either in the form of a full contact zone—that is, the entire debonded segment of the patch maintains sliding contact with the base structure—or edge point contact, where only the “free” edge of the patch maintains sliding contact [Karlsson and Bottega 1999b]. If, for this class, neither of these configurations is possible then contact does not occur: a contact zone does not exist.)

For the case of no contact zone, a relatively simple growth path can be determined in the load-bond zone boundary space and the deflection-bond zone boundary space, or equivalently in the load-deflection space. Various scenarios can be predicted from examination of these paths as follows. Consider the generic growth path shown in Figure 3, where represents the generalized “load”, say the temperature change or the applied transverse pressure, and a corresponds to the size of the damaged region. For a given initial damage size (say point A, C, or F on the horizontal axis), no growth occurs as the load is increased until the load level is such that the growth path is intercepted. At that point growth ensues and may proceed according to several scenarios, depending upon the initial value of a . These scenarios include stable growth (BEH), where an increment in load produces an increment in damage size; unstable growth .D !E/ followed by stable growth (EH), where the damage propagates dynamically (that is, “jumps”) to an alternate stable configuration and then proceeds in a stable manner thereafter; and unstable, catastrophic growth .G ! H0/, where the damage propagates dynamically through the entire length of the patch, resulting in complete detachment of the patch from the base structure.

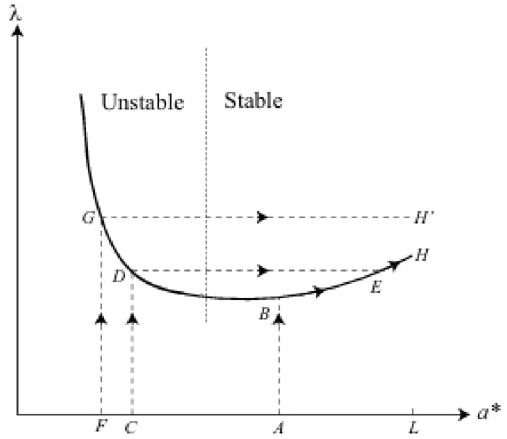

Figure 3. A generic debond growth path.

The formulation discussed in Section 2 and the procedure outlined in the current section are applied to examples of axially (circumferentially) unfettered structures in the next section.

5. Results for axially unfettered structures

In this section, we present results for structures that are completely unfettered and for those whose edges are free to translate in the axial (circumferential) direction. Specifically, in Section 5.1 we consider completely unfettered structures, flat or curved, subjected to temperature change alone. In Section 5.2

we consider the influence of temperature on edge debonding of both flat and curved structures subjected to three-point loading, and in Section 5.3 we examine the effects of temperature on the detachment of axially unfettered patched beam-plates subjected to transverse pressure.

5.1. Unfettered structures in a uniform temperature field. In this section, we examine the behavior of structures, flat or curved, that are completely unfettered (that is, those whose edges are free). The results discussed also hold for the case of pinned-free supports. That is, for structures for which the edges of the base panel are free to translate with regard to axial (circumferential) translation and pinned with regard to rotation.

For this case, a free-body diagram of segments of the structure in each of the regions shows that

$$\kappa_1{}^* = \beta^*\Theta, \qquad \kappa_2{}^* = \kappa_3 = 0. \tag{50}$$

It follows from earlier discussions that for the present case passive contact occurs . 2 D 0/ for the entire detached segment of the patch, regardless of the sign of the thermally-induced curvature in the bond zone. In this case, the transversality conditions given by (42) reduce to the same form,

$$\mathcal{G} = \tfrac{1}{2}\left(\eta/\beta^{*2} - D^*\right)(\beta^*\Theta)^2 = 2\gamma. \tag{51}$$

Since the bond zone boundary does not appear explicitly in the equation (51) for the growth path, the energy release rate is independent of the location of the bond zone boundary. It follows that when growth occurs it is catastrophic. That is, when the critical temperature change is achieved, the entire patch detaches from the base structure in an unstable manner. Substitution of (44)2, (13), and (14) into (51) renders the transversality condition for this case to the form

$$(\beta^*\Theta^*)^2 = \frac{2C_s h^{*2}}{D^*(4D^* - C_s h^{*2})}, \tag{52}$$

$$\Theta^* \equiv \Theta/\sqrt{2\gamma}. \tag{53}$$

It is seen from (52) that the critical renormed thermal curvature, $\beta^*\Theta^*$, is independent of the coefficients of thermal expansion of the constituent layers. The dependence of the critical thermal moment on the modulus ratio, E_0, is displayed in Figure 4 for the case $h_p = h = 0.05$. The peak value of the critical curvature occurs for $E_0 \simeq 0.25$. (For later reference, we note that for $E_0 = 1$, $\|\beta^*\Theta^*\|_{\mathrm{cr}} = 0.8660$.) We remark that, during the thermal loading, deformation, and evolution processes, the entire debonded segment of the patch maintains sliding contact with the base structure regardless of the sign of the renormed thermal curvature, $\beta^*\Theta^*$.

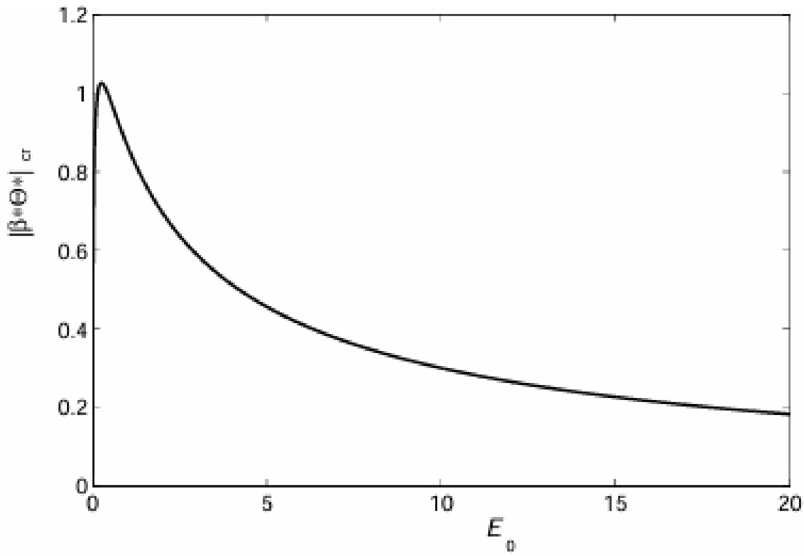

Figure 4. Critical renormed thermal curvature as a function of modulus ratio for a completely unfettered structure subjected to temperature change. ($h_p = h = 0.05$).

5.2. ***Temperature change and three-point loading.*** We next consider structures, both flat ($k = 0$) or cylindrical ($k = 1$), that are subjected to three-point loading and a uniform temperature field. For this case, the upwardly directed (normalized) transverse load at the center of the span is taken to be $2Q_0$, and the supports at the edges of the base panel are pinned-free. Equivalently, the edges of the base panel may each be considered to be loaded with a downwardly directed (normalized) transverse load Q_0 and the center of the span considered to be sitting on a knife edge (Figure 5). The normalized load, Q_0, is related to its dimensional counterpart, $\overline{Q}_0$, as follows:

$$Q_0 = \bar{Q}_0 \bar{\ell}^2 / \overline{D}, \tag{54}$$

where, as defined earlier, $\bar{\ell} = \overline{L}, \overline{R}$ (plate, shell). Consideration of the equilibrium of regions 2 and 3 of the structure shows that (43) is violated, and hence that no contact zone is present.

Patched plate. A region-wise moment balance for the patched beam-plate yields

$$\kappa_1{}^*(a) = \beta^* \Theta + \frac{Q_0}{D^*}(L - a), \qquad \kappa_3(a) = \frac{Q_0}{D}(L - a). \tag{55}$$

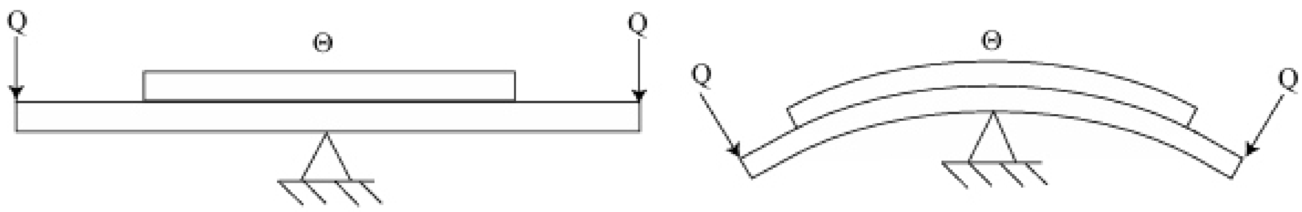

Figure 5. Three-point loading of patched structure. Left: patched beam-plate. Right: patched arch-shell.

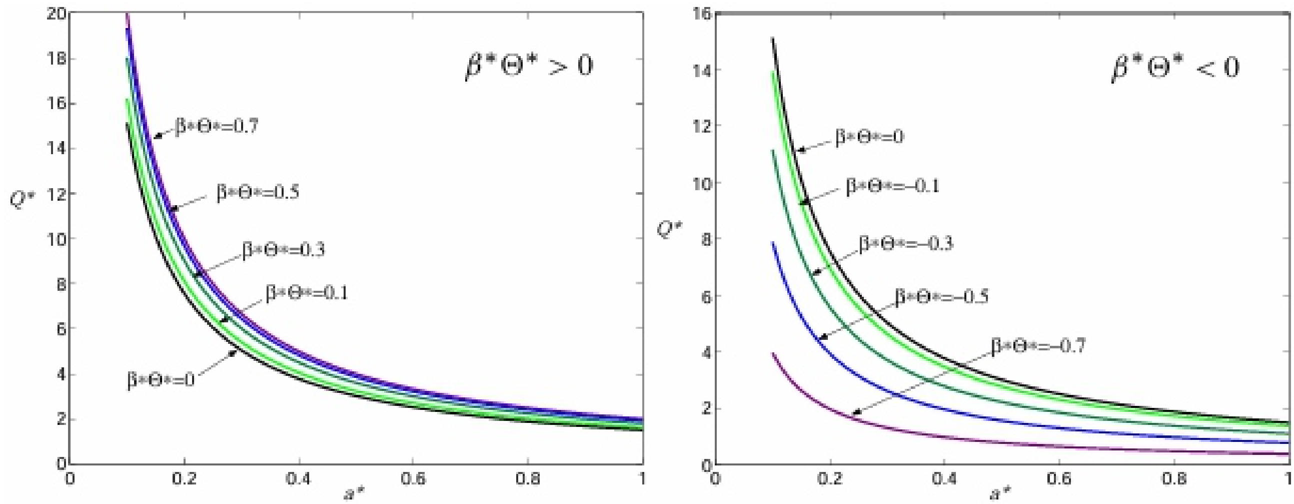

Figure 6. Growth paths for a patched plate subjected to three-point loading for various renormed temperatures (thermal curvatures). $\alpha_p/\alpha = 0.5$ or 2; $E_0 = 1$; $h = h_p = 0.05$.

It may be seen from these equations that a pseudo-inflection point may exist at $x = a$ when $\beta^*\Theta < 0$ and $\|\beta^*\Theta\| > Q_0(L-a)/D^*$. Substitution of (55) into $(42)_2$ reduces the transversality condition for the present case to the form

$$Q^{*2}a^{*2}\Big(\frac{1}{D} - \frac{1}{D^*}\Big) - 2Q^*a^*(\beta^*\Theta^*) + \Big(\frac{\eta}{\beta^{*2}} - D^*\Big)(\beta^*\Theta^*)^2 - 2 = 0, \tag{56}$$

where

$$Q^* \equiv Q/\sqrt{2\gamma}, \qquad \text{and} \qquad \Theta^* \equiv \Theta/\sqrt{2\gamma}. \tag{57}$$

The debond growth paths are easily generated from (56) for any structure of interest. Such paths are displayed in Figure 6 for a structure with the properties $E_0 = 1$, $h_p = h = 0.05$, $\alpha_p/\alpha = 0.5$, and $\alpha_p/\alpha = 2.0$. We note from Figure 4 that, for thermal loading alone, $\|\beta^*\Theta^*\|_{\rm cr} = 0.8660$ when $E_0 = 1$. Thus, propagation will occur due to temperature change alone for this condition. To examine the effects of three-point loading we therefore consider temperature changes for which $\|\beta^*\Theta^*\|_{\rm cr} < 0.8660$.

It may be seen from Figure 6 that, for any initial conjugate bond zone size, once the critical value of Q_0 is achieved it is sufficient for all larger conjugate bond zone sizes. Therefore, growth is catastrophic for all initial damage sizes. That is, once propagation ensues it continues unimpeded, with the patch ultimately completely separated from the base structure. To interpret these results further, we note the following. For the case $\alpha_p/\alpha = 2.0$, $\beta^* > 0$. Thus, for this case, the results displayed in Figure 6, left, correspond to positive temperature changes while those in Figure 6, right, correspond to negative temperature changes. For the case $\alpha_p/\alpha = 0.5$, $\beta^* < 0$, the interpretation is the reverse of that for $\alpha_p/\alpha = 2.0$. That is, for $\alpha_p/\alpha = 0.5$, the results shown on the left are associated with negative temperature changes while those on the right correspond to positive temperature changes. For negative thermally-induced curvature ($\beta^*\Theta^* < 0$), the intact segment of the composite structure is concave up, while the transverse load Q_0 tends to bend the detached segment concave downward thus encouraging “opening”. In this way, the temperature changes are seen to encourage detachment (Figure 6, right), lowering the critical level of the transverse load well below that for vanishing temperature, with increasing magnitude of the temperature change. In contrast, for positive thermally-induced curvature ($\beta^*\Theta^* > 0$), the intact segment of the composite structure is concave down in the same sense as the curvature change of the detached segment as induced by Q_0. The thermal effect here is to oppose “opening” and hence to resist detachment. In this sense, the critical level of the transverse load is seen to increase with increasing thermally-induced moment, as seen in Figure 6, left, though these effects are observed to be less dramatic than those associated with negative thermal moments.

Patched shell. We next consider the analogous problem of a patched panel subjected to three-point loading. Recall that for curved structures, length scales are normalized with respect to the *radius* of the undeformed structure. Normalized arc lengths are then angles. Proceeding as for the beam-plate, a region-wise moment balance for the patched panel yields

$$\kappa_1{}^*(a) = \beta^*\Theta + \frac{Q_0}{D^*}F(a), \qquad \kappa_3(a) = \frac{Q_0}{D}F(a), \tag{58}$$

where

$$F(a) = \cos L(\sin L - \sin a) + \sin L(\cos a - \cos L). \tag{59}$$

It is seen from the above equations that a pseudo-inflection point may exist at $x = a$ when $\beta^*\Theta < 0$ and $\|\beta^*\Theta\| > F(a)/D^*$. Substitution of (58) into the second line of (42) reduces the transversality condition for the present case to the form

$$Q^{*2}[F(a)]^2\left(\frac{1}{D} - \frac{1}{D^*}\right) - 2Q^*F(a)(\beta^*\Theta^*) + \left(\frac{\eta}{\beta^{*2}} - D^*\right)(\beta^*\Theta^*)^2 - 2 = 0, \tag{60}$$

where Q^* and Θ^* are defined by (57).

For the purposes of comparison, we shall examine the behavior of a specific structure having the same proportions as those of the beam-plate considered earlier. Toward this end we consider the structure for which $L = 0.4$ radians, $h_p = h = 0.02$ (same thickness to length ratio as the plate), $E_0 = 1$ and $\alpha_p/\alpha = 0.5$ and 2.0. Corresponding results for a patched shell segment subjected to three-point loading (Figure 5, right) are displayed in Figure 7. It is seen that the behavior is very similar to that of the patched plate. (Recall that the load is normalized via (54).)

5.3. ***Temperature change and transverse pressure.*** In this section, we examine symmetric edge debonding of a patched beam-plate ($k = 0$) for cases where the edges of the base plate are free to translate in the axial direction. It follows from $(25)_2$ and (41) that, for these support conditions, $N_0 = 0$. This renders the governing differential equations for the transverse displacement $w(s)$, resulting from $(7)_1$, $(8)_1$, and $(9)_1$, linear. The solutions may thus be obtained by direct integration, with the constants of integration evaluated by imposing the boundary and matching conditions for transverse motion given by $(15a)_{2,3}$, (17), (18), (21)–(23), $(24)_{2,3}$, (26) and (27). We consider two extreme support conditions at the edges of the base plate: pinned-free and clamped-free. Based on these analytical solutions, numerical simulations are performed for structures possessing the representative properties $h_p = h = 0.05$, $E_0 = 1$, and $2\gamma = 0.1$. The first two properties render $B^* = \beta^* = 0$ and thus eliminate mechanical material bending-stretching coupling within the bonded region. We shall consider two complementary cases of

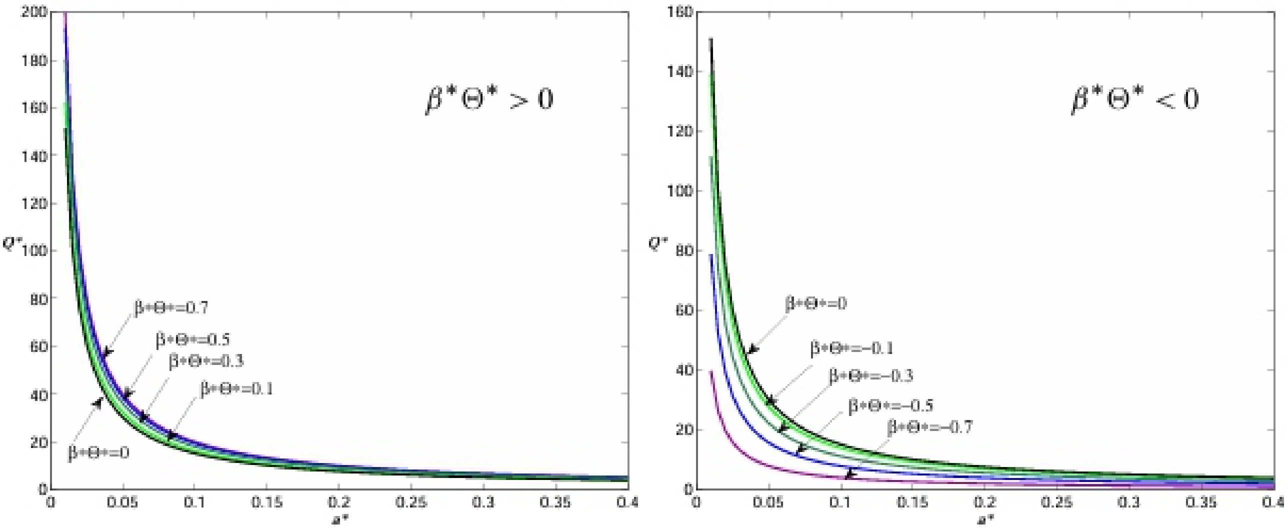

Figure 7. Growth paths for a patched shell subjected to three-point loading for various renormed temperatures (thermal curvatures). $\alpha_p/\alpha = 0.5$ or 2; $E_0 = 1$; $h = h_p = 0.02$; $L = 0.4$.

thermal mismatch: $\alpha_p/\alpha = 0.5$ and $\alpha_p/\alpha = 2.0$. For the purposes of presentation and interpretation of results, we introduce the characteristic deflection $\Delta_0 \equiv -w_1(0)$.

Hinged-free supports. We first examine the behavior of a structure with *hinged-free* supports. That is, a beam-plate for which the edges of the base-plate are hinged with respect to rotation and free with respect to in-plane translation (see Figure 1, left). For such support conditions, it may be anticipated that the deformed structure will not exhibit an inflection point or pseudo-inflection point, under the loading considered when deflections are upward. It follows, from the discussion preceding (45), that if a contact zone is present it will be a full contact zone. Moreover, a contact zone may be present only if the deflection of the structure is downward. However, for the supports and loading under consideration, the curvature of the bonded region will be concave upward during negative deflection, but the curvature of the base plate in the unpatched and detached regions will be concave downward regardless of the sign of the deflection. Thus, there will be a pseudo-inflection point at the bond zone boundary for downward deflections of the structure. Since the curvature of the patch in the detached region must be zero or concave upward, a contact zone is not possible.

Debond growth paths for the ratio $\alpha_p/\alpha = 0.5$ are displayed in Figure 8 for various values of the renormalized temperature $\tilde{\Theta} = \alpha\Theta$. The growth paths are presented in $p - a^*$ space (left half of the figure) and in $\Delta_0 - a^*$ space (right half).

For this ratio of thermal expansion coefficients, the influence of the temperature is greater for the base plate than for the patch, which results in a "concave up" curvature ($\beta^*\Theta < 0$) within the bond zone for positive temperature changes. This opposes the concave down curvature induced by the pressure and thus tends to "flatten" the structure within this region. In contrast, since the unbonded and debonded regions of the base plate are bent by the pressure alone, with the temperature change simply extending that segment of the structure, the curvature in these regions is concave downward. When the pressure

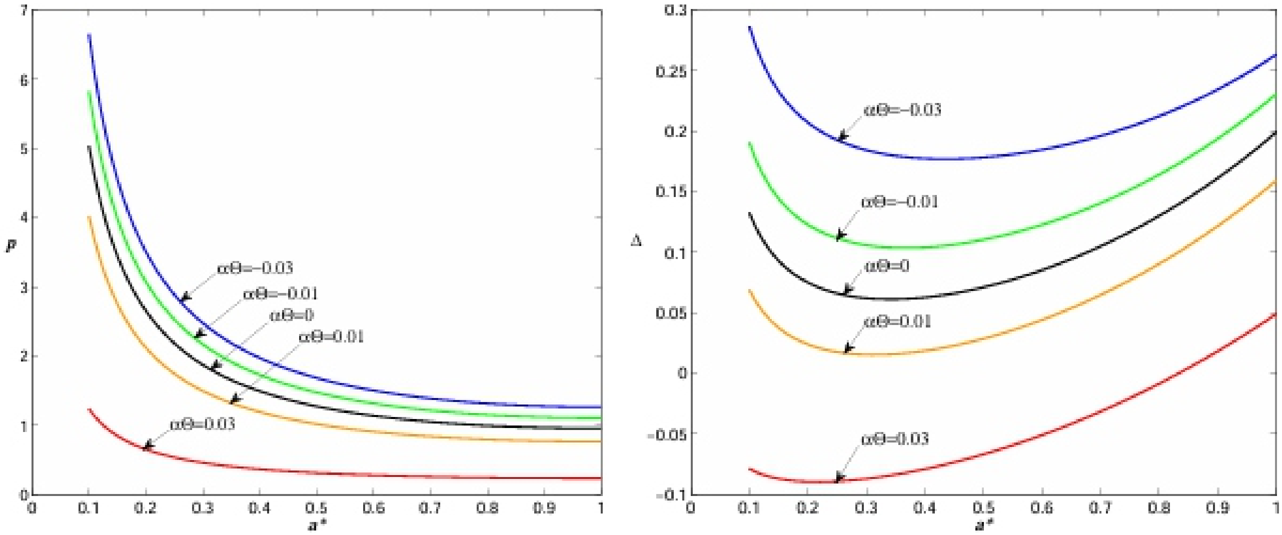

Figure 8. Debond growth paths for structures possessing hinged-free supports, with $\alpha_p/\alpha = 0.5$. Left: p versus a^*. Right: Δ_0 versus a^*.

effect dominates over the thermal moment, the curvature of the bond zone is concave down resulting in an upward deflection of the structure. For pressure-temperature combinations such that the deflection of the structure is upward, the "flattening" of the bond zone (by the temperature change) increases the relative bending of the unpatched segment of the base plate and hence the energy release rate for a given pressure, resulting in a lowering of the threshold pressure with increasing temperature change, as indicated. Moreover, when the temperature is sufficiently large such that the effects of the thermal moments dominate over those due to the pressure, then the curvature within the bond zone will be concave upward and the deflection of the structure will be downward. For these situations, the curvatures of the structure within the bonded and unbonded/debonded regions are of opposite sign, further increasing the relative bending between the detached and bonded segments at the bond zone boundary, and thus increasing the energy release rate at a given pressure level. This, in turn, results in further decreasing of the threshold pressure. Conversely, the threshold pressure increases with decreasing temperature. As the temperature change becomes negative, the thermal moment becomes positive ($\beta^*\Theta > 0$) and reinforces the mechanical moment rendering the curvature of the structure within the bond zone concave down — the same sense as within the detached/unbonded region. As a result, the relative bending at the bond zone boundary is reduced for a given value of the applied pressure and, consequently, the energy release rate. The threshold pressure, therefore, increases accordingly. In this sense, the effect of the thermal moment may be viewed as a reduction of the effective stiffness of the composite structure within the bonded region. At some point, the thermal effect reduces the "effective local stiffness" to the extent that the curvature of the structure within the bond zone is comparable with that of the detached segment of the base plate.

The debond growth paths for a mechanically and geometrically identical structure with $\alpha_p/\alpha = 2.0$ are displayed in Figure 9 for various values of the normalized temperature change. For ratios of the coefficients of thermal expansion greater than one, the thermal moment is positive ($\beta^*\Theta > 0$) for positive temperature changes. The scenarios for structures with this property are therefore the reverse of those for $\alpha_p/\alpha = 0.5$ discussed previously.

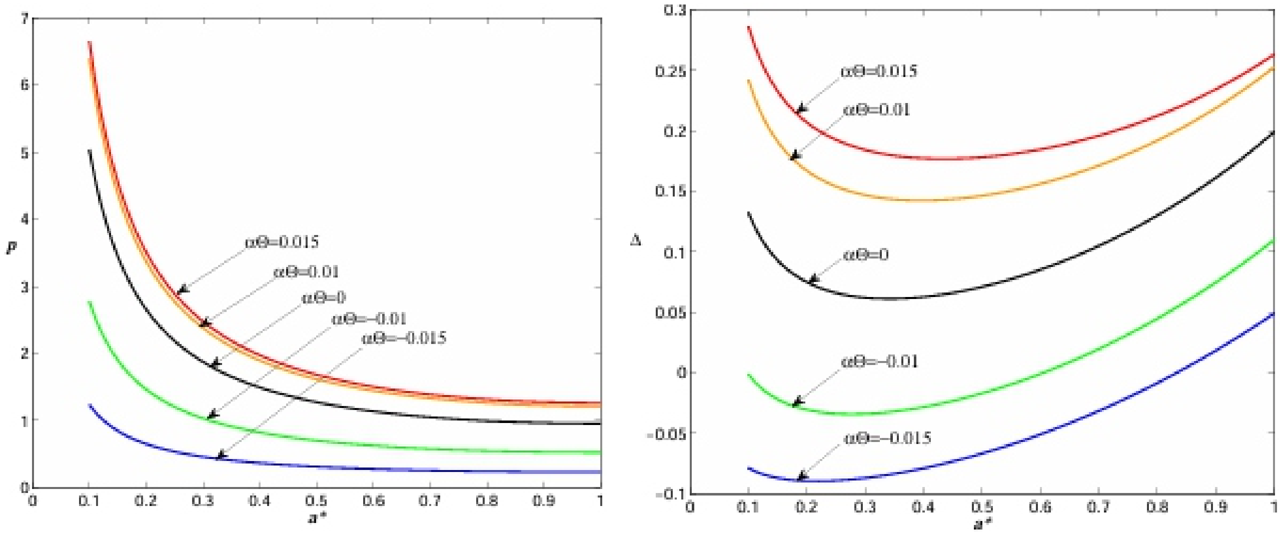

Figure 9. Debond growth paths for structures possessing hinged-free supports, with $\alpha_p/\alpha = 2.0$. Left: p versus a^*. Right: Δ_0 versus a^*.

Clamped-free supports. We next examine the behavior of a structure with *clamped-free* supports. That is, a beam-plate for which the edges of the base-plate are clamped with respect to rotation and free with respect to in-plane translation (see Figure 1, right). The arguments put forth when discussing the previous case, regarding the effects of the competition between the thermal and mechanical moments within the bond zone and their implications regarding curvature of the structure within that region, are paralleled for the present case. However, the constraints imposed on the rotations at the supports for the present case induce a pseudo-inflection point at the bond zone boundary and/or, at least, one inflection point along the half-span [0, 1] for the type of loading considered. For the purposes of the present argument, we consider one inflection or pseudo-inflection point to be present on the half-span. It follows that the curvature of the segment of the structure nearest the support will be concave up when the deflection of the structure is upward. In this light, we deduce the following possible configuration scenarios from (43) and (45). When the deflection is upward, a pseudo-inflection point at the edge of the bonded region or an inflection point within the bond zone will be accompanied by a full contact zone. However, if an inflection point occurs within the unpatched/detached region then it will be accompanied by, at most, contact of the free edge of the patch with the detached segment of the base plate ("edge-point contact"). Conversely, when the deflection is downward, the curvature of the unpatched region will be concave down. For this situation, no contact zone will be present when a pseudo-inflection point is present at the bond zone boundary or an inflection point occurs within the bonded region. A partial propagating contact zone will be present when an inflection point occurs within the detached region and $\Delta_0 < 0$. Situations in which more than one critical point occurs along the span may be considered individually using the criterion established in Section 2 and discussed further in Section 3.

Growth paths for vanishing temperature are presented in Figure 10. Growth paths for structures with the property $\alpha_p/\alpha = 0.5$ are presented in Figure 11, and those for which $\alpha_p/\alpha = 2.0$ are shown in Figure 12, for selected values of the renormed temperature change. It is found, for the geometry and material ratios considered, that a full contact zone is possible for structures for which $L_p \geq 0.79$, depending upon

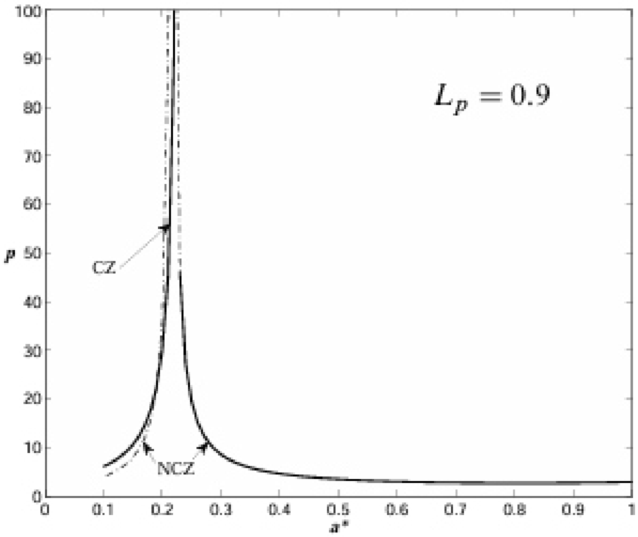

Figure 10. Contact zone (CZ) and no contact zone (NCZ) growth paths for structures subjected to pressure loading only ($\Theta = 0$) and possessing clamped-free supports.

the initial size of the damage. Structures possessing shorter patches have no contact zone regardless of the size of the damage.

Growth paths for a structure possessing a patch of length $L_p = 0.9$ for vanishing temperature change are presented in Figure 10, left. Those for a structure with a patch of length $L_p = 0.8$ are displayed in Figure 10, right. In these figures, the path labeled 'CZ' indicates the presence of a contact zone, and paths labeled 'NCZ' correspond to configurations with no contact zone. Invalid segments of the no contact paths are shown as dashed lines. Both legs of the NCZ path approach an asymptote at $a^* = 0.216$, while the CZ path for $L_p = 0.9$ approaches an asymptote at $a^* = 0.230$. It is seen that, when the contact zone is present, debonding is stable and that growth arrests as the asymptote is approached. It is also seen that the threshold values predicted with a contact zone present are lower than those predicted if it were neglected, for a range of values of a^*. For initial damage size to the right of the asymptote, growth is seen to be catastrophic for relatively small initial conjugate bond zone lengths, unstable followed by stable for intermediate initial damage sizes, and stable for relatively large initial conjugate bond zone sizes and/or patch half-lengths.

The effects of temperature are examined in Figures 11 and 12. The growth paths corresponding to selected temperature changes are displayed in p-a^* space and in Δ_0-a^* space in Figure 11 for structures where $\alpha_p/\alpha = 0.5$. In each case, dashed segments of the paths correspond to equilibrium configurations for which a contact zone is present, ($L_p = 0.9$), while solid lines indicate configurations with no contact zone. Upon consideration of the figures, it is seen that the qualitative debonding behavior under force-controlled loading for moderate to large flaw sizes is very similar to that previously discussed for structures with hinged-free support conditions, but shows slight stabilization for very large debonds. (This stabilization depends on the temperature, as stable debonding is recovered for smaller flaw sizes as the temperature increases.) For this range, no contact zone is present, $\Delta_0 > 0$, and an inflection point occurs in the unpatched/detached region. For long patches, a contact zone is present, reducing the relative bending at the bond zone boundary and thus raising the threshold pressure, stabilizing the process, and

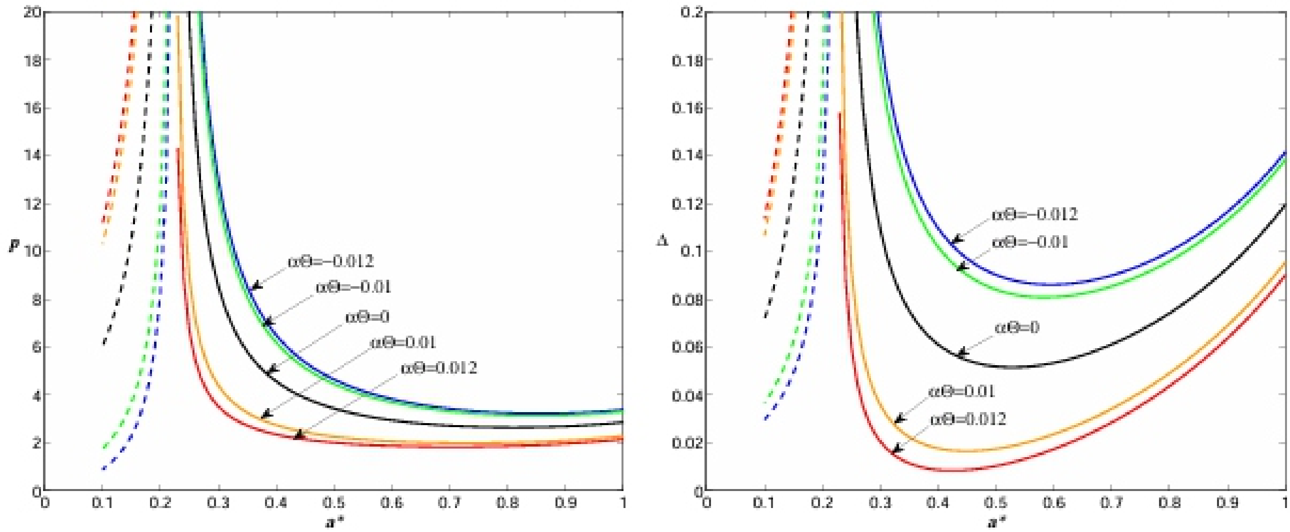

Figure 11. Growth paths corresponding to selected temperatures, for structures with clamped-free supports, with $\alpha_p/\alpha = 0.5$. Dashed lines indicate contact zone configurations for $L_p = 0.9$. Solid lines indicate no contact zone.

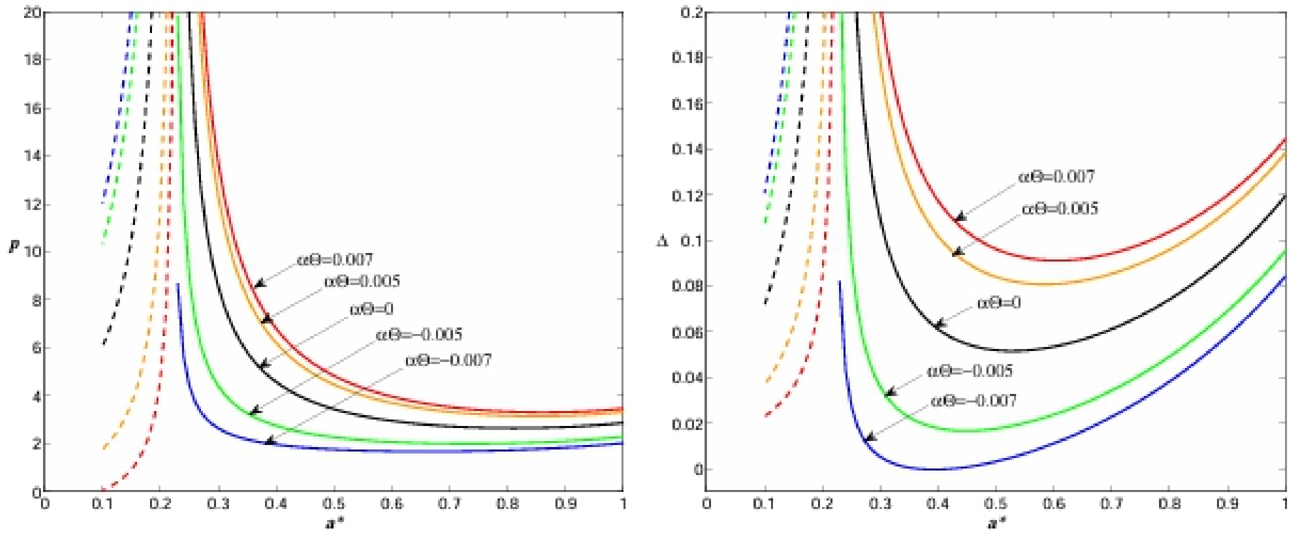

Figure 12. Growth paths corresponding to selected temperatures, for structures with clamped-free supports, with $\alpha_p/\alpha = 2.0$. Dashed lines indicate contact zone configurations for $L_p = 0.9$. Solid lines indicate no contact zone.

leading to eventual (asymptotic) arrest. The scenarios for deflection-controlled loading parallel those discussed for the hinged-free case, for moderate to large disbonds as well. For long patches with small initial debonds, stable growth and asymptotic arrest is indicated as for force-controlled loading. Similar results are shown in Figure 12 for structures with $\alpha_p/\alpha = 2.0$, but the effects of temperature are reversed.

Mode mix. Lastly, we examine the ratio of the mode-II energy release rate to the mode-I energy release rate using the structural scale decomposition presented in Section 3. Configurations for which a contact

Hinged-free support conditions				Clamped-free support conditions			
$\alpha_p/\alpha = 0.5$		$\alpha_p/\alpha = 2$		$\alpha_p/\alpha = 0.5$		$\alpha_p/\alpha = 2$	
$\bar{\Theta}$	G_{II}/G_I	$\bar{\Theta}$	G_{II}/G_I	$\bar{\Theta}$	G_{II}/G_I	$\bar{\Theta}$	G_{II}/G_I
−0.03	0.0019	−0.015	2.9389	−0.012	0.2488	−0.007	2.5102
−0.01	0.3059	−0.010	4.7497	−0.010	0.3059	−0.005	1.7409
0	0.7500	0	0.7500	0	0.7500	0	0.7500
0.01	1.7409	0.010	0.0870	0.010	1.7409	0.005	0.3059
0.03	27.939	0.015	0.0019	0.012	2.0822	0.007	0.1991

Table 1. Dependence of delamination mode ratio on temperature change for structures with hinged-free and clamped-free support conditions.

zone is present correspond to pure mode-II debonding ($G_{II}/G_I \to \infty$). For situations in which no contact zone is present, results for both hinged-free and clamped-free support conditions show that the mode partition ratio is independent of the debond size. Therefore, the qualitative debond scenarios for a given temperature discussed earlier are not altered due to the dependence of bond strength on mode mix the exception being the comparison of contact zone and no contact zone configurations. The threshold levels for contact zone configurations will be relatively higher than indicated for a given temperature since γ will be higher for pure mode-II. For either support condition considered, it is seen that when $\alpha_p/\alpha = 0.5$, the ratio increases with increasing temperature, and vice versa. The reverse is seen when $\alpha_p/\alpha = 2.0$. The dependence of G_{II}/G_I on $\bar{\Theta} \equiv \alpha\Theta$ is summarized in Table 1.

6. Concluding remarks

The problem of debonding of patched panels subjected to temperature change and transverse pressure has been formulated from first principles as a propagating boundaries problem in the calculus of variations. This is done for both cylindrical and flat structures simultaneously. An appropriate geometrically nonlinear thin structure theory is incorporated for each of the primitive structures (base panel and patch) individually. The variational principle then yields the constitutive equations of the composite structure within the patched region and an adjacent contact zone, the corresponding equations of motion within each region of the structure, and the associated matching and boundary conditions for the structure. In addition, the transversality conditions associated with the propagating boundaries of the contact zone and bond zone are obtained directly, the latter giving rise to the energy release rates in self-consistent functional form for configurations in which a contact zone is present, as well as when it is absent. Further, a structural scale decomposition of the energy release rates is established by advancing earlier work of the f irst author to include the effects of temperature. The formulation is utilized to examine the behavior of several representative structures and loadings. These include debonding of completely unfettered patched structures subjected to temperature change, the effects of temperature on the detachment of beam-plates and arch-shells subjected to three-point loading, and the effects of temperature on damage propagation in beam-plates, with both hinged-free and clamped-free support conditions, subjected to transverse pressure. For the unfettered structures subjected to thermal load, the dependence of the critical thermal moment is found as a function of the ratio of elastic moduli, E0, for the patch and base structure. The critical moment is found to increase rapidly as the modulus ratio is increased, to a peak value for a modulus ratio about E0D0:25, and then to decrease as the modulus ratio increases beyond this value. Damage propagation for both plate and shell structures subjected to three-point loading is seen to occur in a catastrophic manner once the critical load level is achieved. The critical load level is seen to be significantly influenced by the temperature field, especially for the shell structures. Similar qualitative behavior was seen for forcecontrolled loading of patched beam-plates subjected to transverse pressure and uniform temperature for the case of hinged-free support conditions. However, for displacement-controlled loading, debond propagation was seen to be stable, unstable followed by stable, or catastrophic, depending on the initial damage size and the temperature. For the case of clamped-free supports, a contact zone is present for very long patches for a limited range of damage sizes. For these situations, growth was seen to be stable, with minor propagation of the damaged region, and to lead to asymptotic arrest. For shorter patches, and for long patches with moderate to large initial damage, no contact zone was present. For these situations, propagation was seen to be catastrophic for moderately small initial damage or moderately large patch size, unstable followed by stable for still larger initial damage and stable for very large initial damage or small patch lengths. The threshold levels of the applied pressure and the stability of debond growth were seen to be strongly influenced by temperature for force-controlled loading. This behavior and its dependence on temperature was accentuated for displacement-controlled loading.

To close, we remark that the membrane force vanishes identically for the axially unfettered structures discussed in Section 5, thus nullifying the contributions of the geometric nonlinearities for these support configurations. It was shown in [Carabetta and Bottega 2008], however, that retention of geometric nonlinearities is essential to adequately model debonding phenomena in thin structures for configurations in which the membrane force does not vanish identically. This is so regardless of whether or not buckling is an issue. In this light, the formulation and analytical procedure developed in the present work (Sections 2–4) is a geometrically nonlinear one, designed to study debonding behavior in structures possessing such configurations. This includes the study of the interaction of thermally-induced buckling and debond propagation as well. Extensive work in this area is currently in progress and will be presented in a forthcoming article by the authors.

Dedication

It is with great pleasure and honor that we contribute this paper to this special issue of JoMMS dedicated to Professor George J. Simitses, a true gentleman and scholar.

References

[Bottega 1995] W. J. Bottega, "Separation failure in a class of bonded plates", Compos. Struct. 30:3 (1995), 253–269.

[Bottega 2003] W. J. Bottega, "Structural scale decomposition of energy release rates for delamination propagation", Int. J. Fract. 122:1–2 (2003), 89–100.

[Bottega 2006] W. J. Bottega, "Sling-shot buckling of composite structures under thermo-mechanical loading", Int. J. Mech. Sci. 48:5 (2006), 568–578.

[Bottega and Karlsson 1999] W. J. Bottega and A. M. Karlsson, "On the detachment of step-tapered doublers, 1: Foundations", Int. J. Solids Struct. 36:11 (1999), 1597–1623

[Bottega and Loia 1996] W. J. Bottega and M. A. Loia, "Edge debonding in patched cylindrical panels", Int. J. Solids Struct. 33:25 (1996), 3755–3777.

[Bottega and Loia 1997] W. J. Bottega and M. A. Loia, "Axisymmetric edge debonding in patched plates", Int. J. Solids Struct. 34:18 (1997), 2255–2289.

[Carabetta and Bottega 2008] P. M. Carabetta and W. J. Bottega, "Effects of geometric nonlinearities on damage propagation in patched beam-plates subjected to pressure loading", Int. J. Fract. 152:1 (2008), 51–62.

[Duong and Wang 2007] C. N. Duong and C. H. Wang, "Bond-line analysis at patch ends", Chapter 7, pp. 248–279 in Composite repair: theory and design, Elsevier, Amsterdam, 2007.

[Duong and Yu 2002] C. N. Duong and J. Yu, "An analytical estimate of thermal effects in a composite bonded repair: plane stress analysis", Int. J. Solids Struct. 39:4 (2002), 1003–1014.

[Karlsson and Bottega 1999a] A. M. Karlsson and W. J. Bottega, "On the detachment of step-tapered doublers, 2: Evolution of pressure loaded structures", Int. J. Solids Struct. 36:11 (1999), 1625–1651.

[Karlsson and Bottega 1999b] A. M. Karlsson and W. J. Bottega, "The presence of edge contact and its influence on the debonding of patched panels", Int. J. Fract. 96:4 (1999), 381–406.

[Karlsson and Bottega 2000a] A. M. Karlsson and W. J. Bottega, "On thermal buckling of patched beam-plates", Int. J. Solids Struct. 37:34 (2000), 4655–4690.

[Karlsson and Bottega 2000b] A. M. Karlsson and W. J. Bottega, "Thermo-mechanical response of patched plates", AIAA J. 38:6 (2000), 1055–1062.

[Moore 2005] T. D. Moore, "Thermomechanical peeling in multilayer beams and plates: a solution from first principles", Int. J. Solids Struct. 42:1 (2005), 271–285.

[Rose 1981] L. R. F. Rose, "An application of the inclusion analogy for bonded reinforcements", Int. J. Solids Struct. 17:8 (1981), 827–838.

[Rutgerson and Bottega 2002] S. E. Rutgerson and W. J. Bottega, "Thermo-elastic buckling of layered shell segments", Int. J. Solids Struct. 39:19 (2002), 4867–4887.

[Rutgerson and Bottega 2004] S. E. Rutgerson and W. J. Bottega, "Pre-limit-point buckling of multilayer cylindrical panels under pressure", AIAA J. 42:6 (2004), 1272–1275.

[Timoshenko 1925] S. Timoshenko, "Analysis of bi-metal thermostats", J. Opt. Soc. Am. 11:3 (1925), 233–255. [Toya 1992] M. Toya, "On mode I and mode II energy release rates of an interface crack", Int. J. Fract. 56:4 (1992), 345–352.

[Toya et al. 2005] M. Toya, M. Oda, A. Kado, and T. Saitoh, "Enegy release rates for an edge delamination of a laminated beam subjected to thermal gradient", J. Appl. Mech. .ASME/ 72:5 (2005),

[Wang and Rose 2000] C. H. Wang and L. R. F. Rose, "Compact solutions for the corner singularity in bonded lap joints", Int. J. Adhes. Adhes. 20:2 (2000), 145–154.

[Wang et al. 2000] C. H. Wang, L. R. F. Rose, R. Callinan, and A. A. Baker, "Thermal stresses in a plate with circular reinforcement", Int. J. Solids Struct. 37:33 (2000), 4577–4599. *Received 11 Sep 2008. Revised 23 Dec 2008. Accepted 31 Dec 2008.*

WILLIAM J. BOTTEGA: bottega@rci.rutgers.edu

Department of Mechanical and Aerospace Engineering, Rutgers University, 98 Brett Road, Piscataway, NJ 08854-8058, United States

PAMELA M. CARABETTA: pamc@eden.rutgers.edu

Department of Mechanical and Aerospace Engineering, Rutgers University, 98 Brett Road, Piscataway, NJ 08854-8058, United States

ISSN Application No. 21818

EXPONENTIAL SOLUTIONS FOR A LONGITUDINALLY VIBRATING INHOMOGENEOUS ROD

IVO CALIÒ AND ISAAC ELISHAKOFF

A special class of closed form solutions for inhomogeneous rods is investigated, arising from the follow ing problem: for a given distribution of the material density, find the axial rigidity of an inhomogeneous rod so that the exponential mode shape serves as the vibration mode. Specifically, for a rod clamped at one end and free at the other, the exponentially varying vibration mode is postulated and the associated semi-inverse problem is solved. This yields distributions of axial rigidity which, together with a specific law of material density, satisfy the governing eigenvalue problem. The results obtained can be used in the context of functionally graded materials for vibration tailoring, that is, for the design of a rod with a given natural frequency according to a postulated vibration mode.

1. Introduction

Recently, several closed-form solutions have been derived by the semi-inverse method [Elishakoff 2005] for the problem of eigenvalues of inhomogeneous structures. In particular Candan and Elishakoff [2001] solved the problem of construction of a bar with a specified mass density and a preselected polynomial mode shape, while Ram and Elishakoff [2004] solved the analogous problem in the discrete setting. It turns out that a bar with a tip mass [Elishakoff and Perez 2005] or with a translational spring [Elishakoff and Yost 2009] can also possess a polynomial mode shape.

In a personal communication to the second author (2007), Dr. A. R. Khvoles posed the question of whether or not an inhomogeneous rod may possess an exponential mode shape. This question is elucidated in the present study. The solution can serve as a benchmark for the validation of various approximate analyses and numerical techniques.

Formulation of problem. Let us consider an inhomogeneous rod of length L, cross-sectional area A.x/, varying modulus of elasticity E.x/, and varying material density .x/. The governing differential equa tion of the dynamic behavior of such an inhomogeneous rod is given by

$$\frac{\partial}{\partial x}\left[E(x)A(x)\frac{\partial u(x,t)}{\partial x}\right]-\rho(x)A(x)\frac{\partial u^2(x,t)}{\partial t^2}=0, \tag{1}$$

where x is the axial coordinate, t the time, and $u(x,t)$ the axial displacement.

For simplicity, the nondimensional coordinate $\xi = x/L$ is introduced. Harmonic vibration is studied so that the displacement $u(x,t)$ is represented as

$$u(\xi,t)=U(\xi)e^{i\omega t}, \tag{2}$$

where $U(\xi)$ is the postulated mode shape and ω the corresponding natural frequency which has to be determined. Upon substitution of Equation (2) into (1), the latter becomes

$$\frac{d}{d\xi}\left[E(\xi)A(\xi)\frac{dU(\xi)}{d\xi}\right]+L^2\rho(\xi)A(\xi)\omega^2U(\xi)=0. \tag{3}$$

The semi-inverse eigenvalue problem is posed as follows: Find an inhomogeneous rod that with reference to a specified exponential mode, $U(\xi)$, satisfies its boundary conditions and the governing dynamic equation of motion. This semi-inverse problem requires the determination of the distribution of axial rigidity, $D(\xi)=E(\xi)A(\xi)$, that together with a prespecified law for the mass distribution, $m(\xi)=A(\xi)\rho(\xi)$, satisfies (3).

We postulate the following form for the mode shape:

$$U(\xi)=A_0+A_1\xi\exp(\lambda\xi). \tag{4}$$

In this study, the differential equation (1) will be solved in a closed form for a rod that is clamped at one end and free at the other.

2. Clamped-free rod

We consider an inhomogeneous rod for which the following boundary conditions must be satisfied:

$$U(0)=0, \qquad U'(0)\neq 0, \tag{5}$$

$$U(1)\neq 0, \qquad N(1)=0, \tag{6}$$

where $N(1)$ is the axial force at $\xi=1$, namely $N(1)=E(1)A(1)U'(1)/L$. Therefore in order to satisfy the boundary condition the mode shape assumes the form

$$U(\xi)=A_1\xi\exp(-\xi), \qquad U'(\xi)=A_1(1-\xi)\exp(-\xi), \tag{7}$$

whose graph, for $A_1=1$, is shown in Figure 1.

Assuming that the mode shape is known, by integrating (3) we obtain

$$E(\xi)A(\xi)\frac{dU(\xi)}{d\xi}=-\omega^2L^2\int_0^{\xi}\rho(\eta)A(\eta)U(\eta)d\eta+N(0)L, \tag{8}$$

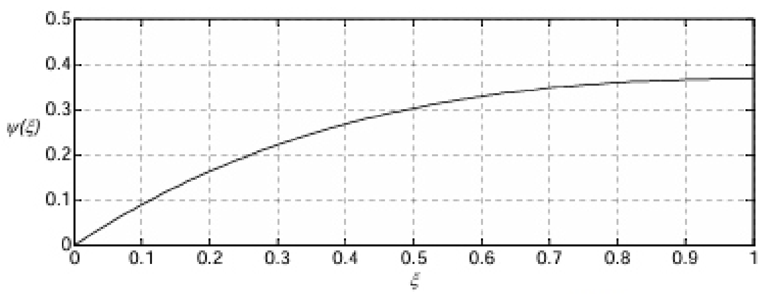

Figure 1. Postulated mode shape, (7).

where N.0 / is the amplitude of the axial loading at the cross-section 0.For the clamped-free bar the boundary conditions (6) become

$$N(1) = \frac{E(1)A(1)}{L} \left. \frac{dU}{d\xi} \right|_{\xi=1} = 0. \tag{9}$$

By evaluating (8) at $\xi = 1$ and employing the boundary condition (9) the following value of $N(0)$ is obtained:

$$N(0) = \omega^2 L \int_0^1 \rho(\alpha)A(\alpha)U(\alpha)\,d\alpha. \tag{10}$$

This condition coincides with [Elishakoff et al. 2001, equation 23]. Substitution of (10) into (8) yields

$$E(\xi)A(\xi)\frac{dU}{d\xi} = \omega^2 L^2 \int_\xi^1 \rho(\alpha)A(\alpha)U(\alpha)\,d\alpha. \tag{11}$$

In the semi-inverse formulation, the mode shape $U(\xi)$ is a postulated function, that is,

$$U(\xi) = \psi(\xi). \tag{12}$$

Substitution into (11) yields the desired axial rigidity

$$D(\xi) = E(\xi)A(\xi) = \frac{\omega^2 L^2}{\psi'(\xi)} \int_\xi^1 \rho(\alpha)A(\alpha)\psi(\alpha)\,d\alpha. \tag{13}$$

The candidate mode shape ought to satisfy the boundary conditions. Considering the candidate mode shape $\psi(\xi) = \xi \exp(-\xi)$, the following particular cases arise:

Case 1: Constant cross-sectional area and constant material density. When

$$A(\xi) = \text{const} = A_0, \qquad \rho(\xi) = \text{const} = \rho_0, \tag{14}$$

then (13) becomes

$$D(\xi) = A_0\rho_0\omega^2 L^2 \frac{e - 2e^\xi + e\xi}{e(1-\xi)}. \tag{15}$$

It is easy to verify that $D(0) > 0$ at $\xi = 0$. By applying L'Hospital's rule at $\xi = 1$, we observe that $D(1) > 0$. Therefore, assuming the distribution of axial rigidity reported in Figure 2a,

$$D(\xi) = D_0 \frac{e - 2e^\xi + e\xi}{e(1-\xi)} \tag{16}$$

in conjunction with the postulated mode shape in (7), shown in Figure 1, and the axial distribution

$$N(\xi) = D_0 \frac{e - 2e^\xi + e\xi}{e(1-\xi)} \psi'(\xi), \tag{17}$$

represented in Figure 2b, the following eigenvalue parameter is obtained: $\omega^2 = D_0/A_0\rho_0 L^2$.

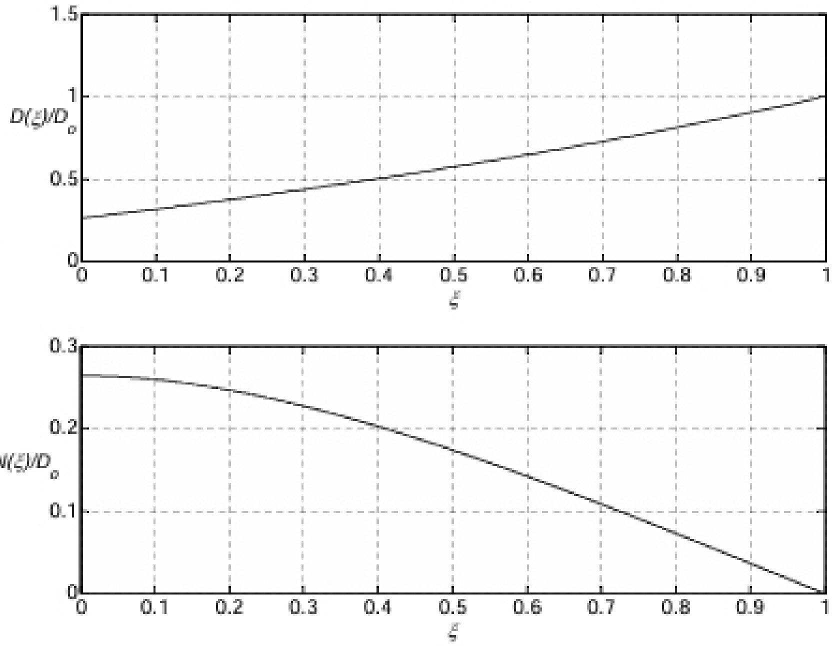

(a)

(b)

Figure 2. Variation in the axial modulus (a) and axial force (b) in an inhomogeneous bar, corresponding to the mode shape in Figure 1.

Case 2: Variable cross-sectional area and constant material density. When

$$A(\xi) \neq \text{const}, \qquad \rho(\xi) = \text{const} = \rho_0, \tag{18}$$

then (13) gives

$$E(\xi) = \frac{\omega^2 L^2}{A(\xi)\psi'(\xi)} \int_{\xi}^{1} \rho(\eta) A(\eta) U(\eta)\, d\eta. \tag{19}$$

As an example we assume the following form for $A(\xi)$:

$$A(\xi) = A_0\big(1 + \alpha\xi \exp(-\xi)\big), \tag{20}$$

with $A_0 > 0$ and $\alpha > -1$. Integrating (19), we obtain for the Young's modulus

$$E(\xi) = \omega^2 L^2 \rho_0 \frac{4e^{1+\xi}\left(2e^{\xi} - e(1+\xi)\right) + \alpha\left(5e^{2\xi} - e^2(1+2\xi+2\xi^2)\right)}{4e^2(\xi-1)(e^{\xi}+\alpha\xi)}. \tag{21}$$

In view of (20) and (21), the axial stiffness becomes

$$D(\xi) = A_0\rho_0\omega^2 L^2 \frac{4 - 8e^{\xi-1} + 4\xi + \alpha e^{-\xi-2}\left(-5e^{2\xi} + e^2(1+2\xi+2\xi^2)\right)}{4(1-\xi)}. \tag{22}$$

In Figure 3, the area variability $A(\xi)$, the Young modulus $E(\xi)$, the axial stiffness $D(\xi)$, and the axial force $N(\xi)$ are reported for the case $\alpha = 1$.

It is worth noticing that the solution that has been derived is not reducible to the case where the variation of elastic modulus, density, and cross sectional area are constants.

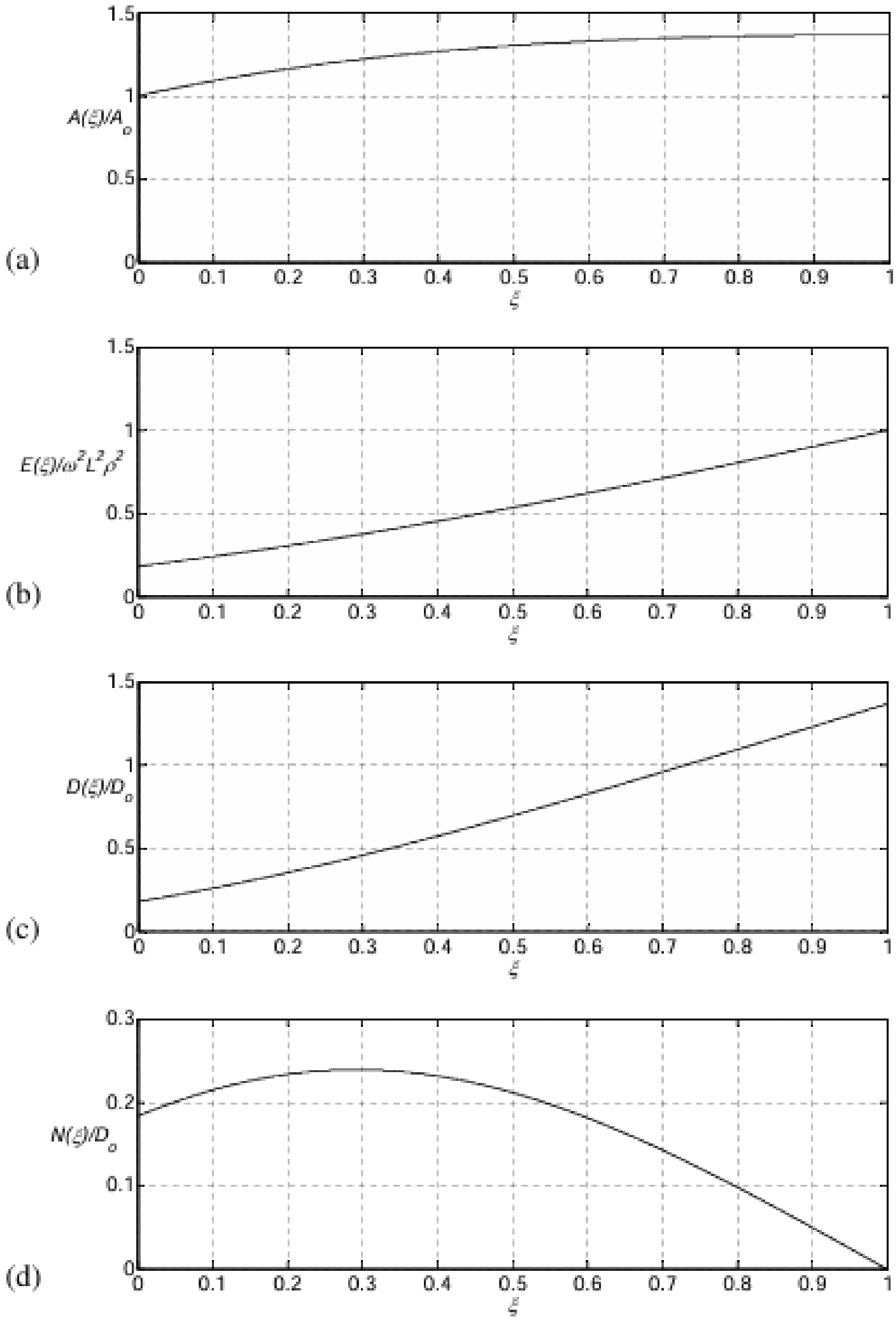

Figure 3. Variation of the cross-sectional area (a), modulus of elasticity (b), axial rigidity (b) and axial force (d) versus a nondimensional coordinate.

3. Conclusion

Apparently for the first time in the literature, it is shown that an inhomogeneous rod can possess an exponential mode shape. The derived closed-form solution can be utilized as a model solution for verification purposes.

References

[Candan and Elishakoff 2001] S. Candan and I. Elishakoff, "Constructing the axial stiffness of longitudinally vibrating rod from fundamental mode shape", Int. J. Solids Struct. 38:19 (2001), 3443–3452.

[Elishakoff 2005] I. Elishakoff, Eigenvalues of inhomogeneous structures: unusual closed-form solutions, CRC Press, Boca Raton, FL, 2005.

[Elishakoff and Perez 2005] I. Elishakoff and A. Perez, "Design of a polynomially inhomogeneous bar with a tip mass for specified mode shape and natural frequency", J. Sound Vib. 287:4–5 (2005), 1004–1012.

[Elishakoff and Yost 2009] I. Elishakoff and J. Yost, "Vibration tailoring of a polynomially inhomogeneous bar with a translational spring". In preparation.

[Elishakoff et al. 2001] I. Elishakoff, M. Baruch, and R. Becquet, "Turning around a method of successive iterations to yield closed-form solutions for vibrating inhomogeneous bars", Meccanica .Milano/ 36:5 (2001), 573–786.

[Ram and Elishakoff 2004] Y. M. Ram and I. Elishakoff, "Reconstructing the cross-sectional area of an axially vibrating non uniform rod from one of its mode shapes", Proc. R. Soc. Lond. A 460:2046 (2004), 1583–1596.

Received 11 Nov 2008. Revised 18 Jan 2009. Accepted 19 Jan 2009.

IVO CALIÒ: icalio@dica.unict.it

Dipartimento di Ingegneria Civile e Ambientale, Università di Catania, Catania, Italy

ISAAC ELISHAKOFF: elishako@fau.edu

Department of Mechanical Engineering, Florida Atlantic University, P.O. Box 3091, Boca Raton, FL 33431-0991, United State

ISSN Application No. 21818

INFLUENCE OF CORE PROPERTIES ON THE FAILURE OF COMPOSITE SANDWICH BEAMS

ISAAC M. DANIEL

The initiation of failure in composite sandwich beams is heavily dependent on properties of the core material. Several core materials, including PVC foams and balsa wood were characterized. The various failure modes occurring in composite sandwich beams are described and their relationship to the relevant core properties is explained and discussed. Under flexural loading of sandwich beams, plastic yielding or cracking of the core occurs when the critical yield stress or strength (usually shear) of the core is reached. Indentation under localized loading depends principally on the square root of the core yield stress. The critical stress for facesheet wrinkling is related to the core Young's and shear moduli in the thickness direction. Experimental mechanics methods were used to illustrate the failure modes and verify analytical predictions.

1. Introduction

The overall performance of sandwich structures depends in general on the properties of the facesheets, the core, the adhesive bonding the core to the skins, and geometric dimensions. Sandwich beams under general bending, shear and in-plane loading display various failure modes. Their initiation, propagation, and interaction depend on the constituent material properties, geometry, and type of loading. Failure modes and their initiation can be predicted by conducting a thorough stress analysis and applying appropriate failure criteria in the critical regions of the beam. This analysis is difficult because of the nonlinear and inelastic behavior of the constituent materials and the complex interactions of failure modes. Possible failure modes include tensile or compressive failure of the facesheets, debonding at the core/facesheet interface, indentation failure under localized loading, core failure, wrinkling of the compression facesheet, and global buckling. Following initiation of a particular failure mode, this mode may trigger and interact with other modes and final failure may follow a different failure path. A general review of failure modes in composite sandwich beams was given in [Daniel et al. 2002]. Individual failure modes in sandwich columns and beams are discussed in [Abot et al. 2002; Gdoutos et al. 2002b; 2003]. Of all the factors influencing failure initiation and mode, the properties of the core material are the most predominant.

Commonly used materials for facesheets are composite laminates and metals, while cores are made of metallic and nonmetallic honeycombs, cellular foams, balsa wood, or truss.

The facesheets carry almost all of the bending and in-plane loads while the core helps to stabilize the facesheets and defines the flexural stiffness and out-of-plane shear and compressive behavior. A number of core materials, including aluminum honeycomb, various types of closed-cell PVC foams,

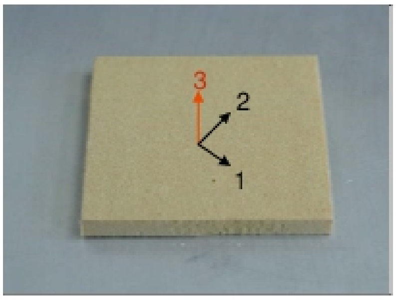

Figure 1. Material coordinate system for sandwich cores.

a polyurethane foam, foam-filled honeycomb and balsa wood, were characterized under uniaxial and biaxial states of stress. In the present work, failure modes were investigated experimentally in axially loaded composite sandwich columns and sandwich beams under bending. Failure modes observed and studied include indentation failure, core failures, and facesheet wrinkling. The transition from one failure mode to another for varying loading or state of stress and beam dimensions was discussed. Experimental results were compared with analytical predictions.

2. Characterization of core materials

The core materials characterized were four types of a closed-cell PVC foam (Divinycell H80, H100, H160 and H250, with densities of 80, 100, 160 and 250kg/m3, respectively), an aluminum honeycomb (PAMG 8.1-3/16 001-P-5052, Plascore Co.), a polyurethane foam, a foam-filled honeycomb, and balsa wood. Of these, the low density foam cores are quasi-isotropic, while the high density foam cores, the honeycombs, and balsa wood are orthotropic with the 1-2 plane parallel to the facesheets being a plane of isotropy and the through-thickness direction (3-direction) a principal axis of higher stiffness, as shown in x Figure 1. All core materials were characterized in uniaxial tension, compression, and shear along the inplane and through-thickness directions. Typical stress-strain curves are shown in Figures 2 and 3. Some

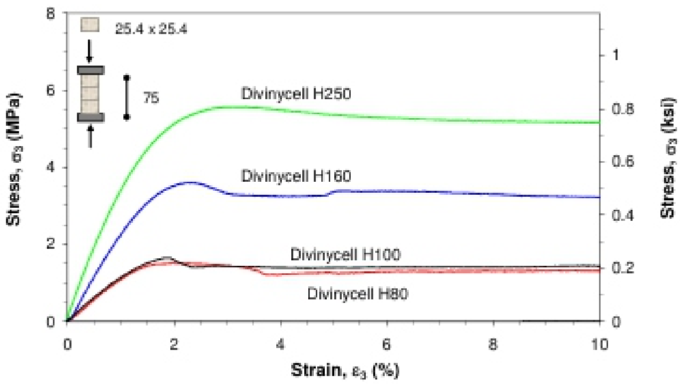

Figure 2. Stress-strain curves of PVC foam cores under compression in the through-thickness direction.

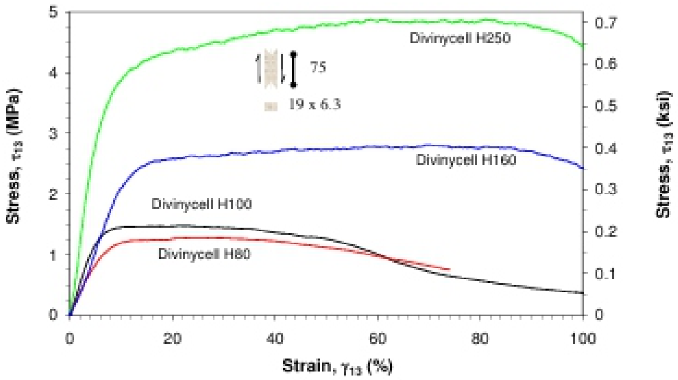

Figure 3. Shear stress-strain curves of PVC foam cores under through-thickness shear.

of their characteristic properties are tabulated in Table 1. The core materials (honeycomb or foam) were provided in the form of 25.4mm thick plates. The honeycomb core was bonded to the top and bottom facesheets with FM73 M film adhesive and the assembly was cured under pressure in an oven following the recommended curing cycle for the adhesive. The foam cores were bonded to the facesheets using a commercially available epoxy adhesive (Hysol EA 9430) [Daniel and Abot 2000]. Beam specimens 25.4mm wide and of various lengths were cut from the sandwich plates.

Two core materials, Divinycell H100 and H250 were fully characterized under multiaxial stress con ditions [Gdoutos et al. 2002a]. A series of biaxial tests were conducted including constrained strip specimens in tension and compression with the strip axis along the through-thickness and in-plane directions; constrained thin-wall ring specimens in compression and torsion; thin-wall tube specimens in tension and torsion; and thin-wall tube specimens under axial tension, torsion and internal pressure. From these tests and uniaxial results in tension, compression, and shear, failure envelopes were constructed. It

Sandwich core material	ρ	E_1	E_2	E_3	G_{13}	F_{1c}	F_{1t}	F_{2c}	F_{3c}	F_5
Divinycell H80	80	77	77	110	18	1.0	2.3	1.0	1.4	1.1
Divinycell H100	100	95	95	117	25	1.4	2.7	1.4	1.6	1.4
Divinycell H160	160	140	140	250	26	2.5	3.7	2.5	3.6	2.8
Divinycell H250	250	255	245	360	73	4.5	7.2	4.5	5.6	4.9
Balsa Wood CK57	150	110	110	4600	60	0.8	1.2	0.8	9.7	3.7
Aluminum Honeycomb PAMG 5052	130	8.3	6.0	2200	580	0.2	1.2	0.2	11.8	3.5
Foam Filled Honeycomb Style 20	128	25	7.6	240	8.7	0.4	0.5	0.3	1.4	0.75
Polyurethane FR-3708	128	38	38	110	10	1.2	1.1	1.1	1.8	1.4

Table 1. Properties of sandwich core materials: the density, ρ (in units of kg/m^3); and the in-plane moduli, E_1 and E_2, the out of plane modulus, E_3, the transverse shear modulus, G_{13}, the in-plane compressive strength, F_{1c}, the in-plane tensile strength, F_{1t}, the in-plane compressive strength, F_{2c}, the out of plane compressive strength, F_{3c}, and the transverse shear strength, F_5 (all in units of MPa).

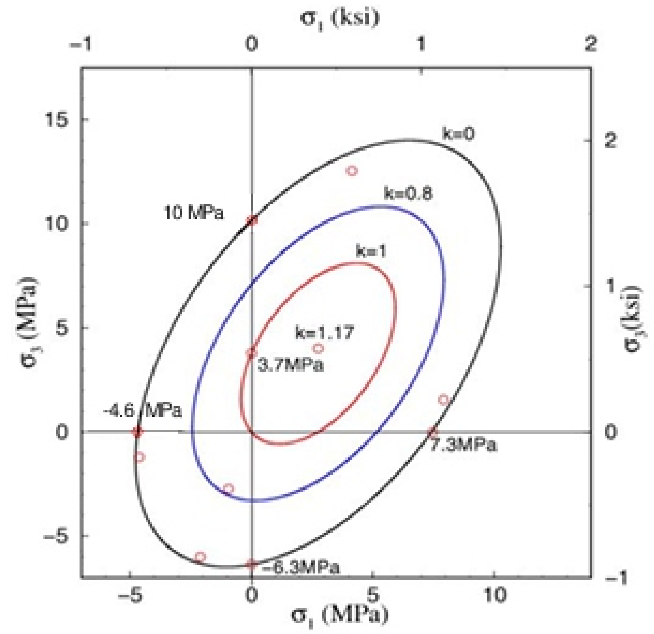

Figure 4. Failure envelopes predicted by the Tsai–Wu failure criterion for PVC foam (Divinycell H250) for $k = 0$, 0.8 and 1, and experimental results ($k = \tau_{13}/F_{13} = \tau_5/F_5$).

was shown that the failure envelopes were described well by the Tsai–Wu criterion [1971], as shown in Figure 4.

The Tsai–Wu criterion for a general two-dimensional state of stress on the 1-3 plane is expressed as

$$f_1\sigma_1 + f_3\sigma_3 + f_{11}\sigma_1^2 + f_{33}\sigma_3^2 + 2f_{13}\sigma_1\sigma_3 + f_{55}\tau_5^2 = 1, \quad (1)$$

where

$$f_1 = \frac{1}{F_{1t}} - \frac{1}{F_{1c}}, \qquad f_3 = \frac{1}{F_{3t}} - \frac{1}{F_{3c}}, \qquad f_{11} = \frac{1}{F_{1t}F_{1c}},$$

$$f_{33} = \frac{1}{F_{3t}F_{3c}}, \qquad f_{13} = -\frac{1}{2}(f_{11}f_{33})^{1/2}, \qquad f_{55} = \frac{1}{F_5^2}.$$

Here F_{1t}, F_{1c}, F_{3t}, and F_{3c} are the tensile and compressive strengths in the in-plane (1, 2) and out-of-plane (3) directions, and F_5 is the shear strength on the 1-3 plane.

Setting $\tau_5 = kF_5$, we can rewrite (1) as

$$f_1\sigma_1 + f_3\sigma_3 + f_{11}\sigma_1^2 + f_{33}\sigma_3^2 + 2f_{13}\sigma_1\sigma_3 = 1 - k^2. \quad (2)$$

It was assumed that the failure behavior of all core materials can be described by the Tsai–Wu criterion Failure envelopes of all core materials constructed from the values of F_{1t}, F_{1c} and F_5 are shown in Figure 5. Note that the failure envelopes of all Divinycell foams are elongated along the σ_1-axis, which indicates that these materials are stronger under normal longitudinal stress than in-plane shear stress. Aluminum honeycomb and balsa wood show the opposite behavior. For all materials, the most critical combinations of shear and normal stress fall in the second and third quadrants (the failure envelopes are symmetrical with respect to the σ_1-axis).

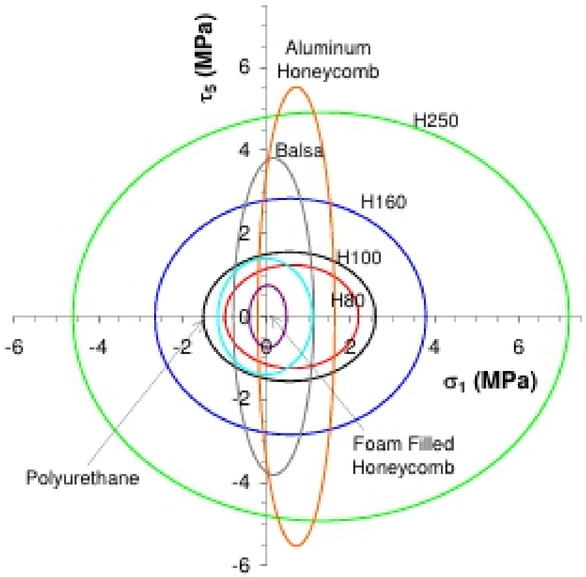

Figure 5. Failure envelopes for various core materials based on the Tsai–Wu failure criterion for interaction of normal and shear stresses.

3. Core failures

The core is primarily selected to carry the shear loading. Core failure by shear is a common failure mode in sandwich construction [Allen 1969; Hall and Robson 1984; Zenkert and Vikström 1992; Zenkert 1995; Daniel et al. 2001a; 2001b; Sha et al. 2006]. In short beams under three-point bending the core is mainly subjected to shear, and failure occurs when the maximum shear stress reaches the critical value (shear strength) of the core material. In long-span beams the normal stresses become of the same order of magnitude as, or even higher than the shear stresses. In this case, the core in the beam is subjected to a biaxial state of stress and fails according to an appropriate failure criterion. It was shown earlier that failure of the PVC foam core Divinycell H250 can be described by the Tsai–Wu failure criterion [Gdoutos et al. 2002a; Bezazi et al. 2007].

For a sandwich beam of rectangular cross section, with facesheets and core materials displaying linear elastic behavior, subjected to a bending moment, M, and shear force, V, the in-plane maximum normal stress, σ, and shear stress, τ, in the core, for a low stiffness core and thin facesheets are given by [Daniel et al. 2001a]

$$\sigma = \frac{PL}{C_1 b d^2}\left(\frac{E_c}{E_f}\right)\frac{h_c}{h_f}, \qquad \tau = \frac{P}{C_2 b h_c}, \tag{3}$$

where

$$M = \frac{PL}{C_1}, \qquad V = \frac{P}{C_2}, \tag{4}$$

P being the applied concentrated load, L the length of beam, E_f and E_c the Young's moduli of the facesheet and core material, h_f and h_c the thicknesses of the facesheets and core, d the distance between the centroids of the facesheets, b the beam width, and C_1 and C_2 constants depending on the loading configuration ($C_1 = 4$, $C_2 = 2$ for three-point bending; $C_1 = C_2 = 1$ for a cantilever beam).

The maximum normal stress, σ, for a beam under three-point bending occurs under the load, while for a cantilever beam under end loading it occurs at the support. The shear stress, τ, is constant along the beam span and through the core thickness, as verified experimentally [Daniel and Abot 2000; Daniel et al. 2002].

When the normal stress in the core is small relative to the shear stress, it can be assumed that core failure occurs when the shear stress reaches a critical value. Furthermore, failure in the facesheets occurs when the normal stress reaches its critical value, usually the facesheet compressive strength. Under such circumstances we obtain from (3) that failure mode transition from shear core failure to compressive facesheet failure occurs when

$$\frac{L}{h_f} = C\frac{F_f}{F_{cs}}, \tag{5}$$

where F_f is the facesheet strength in compression or tension, F_{cs} is the core shear strength, and C is a constant ($C = 2$ for a beam under three-point bending; $C = 1$ for a cantilever beam under an end load).

When the left-hand term of (5) is smaller than the right hand term, failure occurs by core shear, whereas in the reverse case failure occurs by facesheet tension or compression.

The deformation and failure mechanisms in the core of sandwich beams have been studied experimentally by means of moiré gratings and photoelastic coatings [Daniel and Abot 2000; Daniel et al. 2001a; 2001b; Gdoutos et al. 2001; 2002b; Abot and Daniel 2003]. Figure 6 shows moiré fringe patterns in the core of a sandwich beam under three-point bending for an applied load that produces stresses in the core within the linear elastic range. The moiré fringe patterns corresponding to the u (horizontal) and w (through-the-thickness) displacements away from the applied load consist of nearly parallel and equidistant fringes from which it follows that

$$\varepsilon_x = \frac{\partial u}{\partial x} \cong 0, \qquad \varepsilon_z = \frac{\partial w}{\partial z} \cong 0, \qquad \gamma_{xz} = \frac{\partial u}{\partial z} + \frac{\partial w}{\partial x} = \text{constant}. \tag{6}$$

Thus, the core is under nearly uniform shear stress. This is true only in the linear range, as will be illustrated below.

Figure 7 shows photoelastic coating fringe patterns for a beam under three-point bending. The fringe pattern for a low applied load (2.3 kN) is nearly uniform, indicating that the shear strain (stress) in the

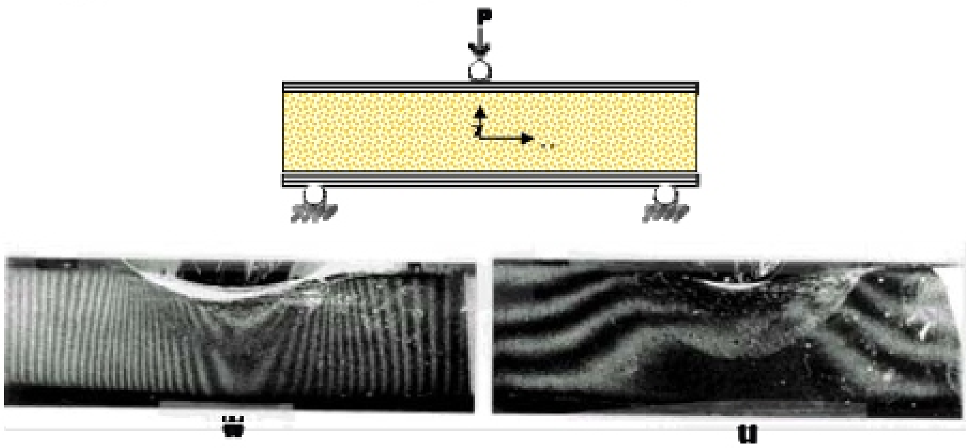

Figure 6. Moiré fringe patterns corresponding to horizontal and vertical displacements in sandwich beam under three-point bending (12 lines/mm, Divinycell H250 core).

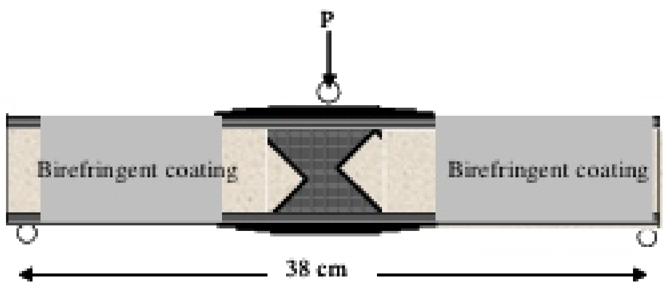

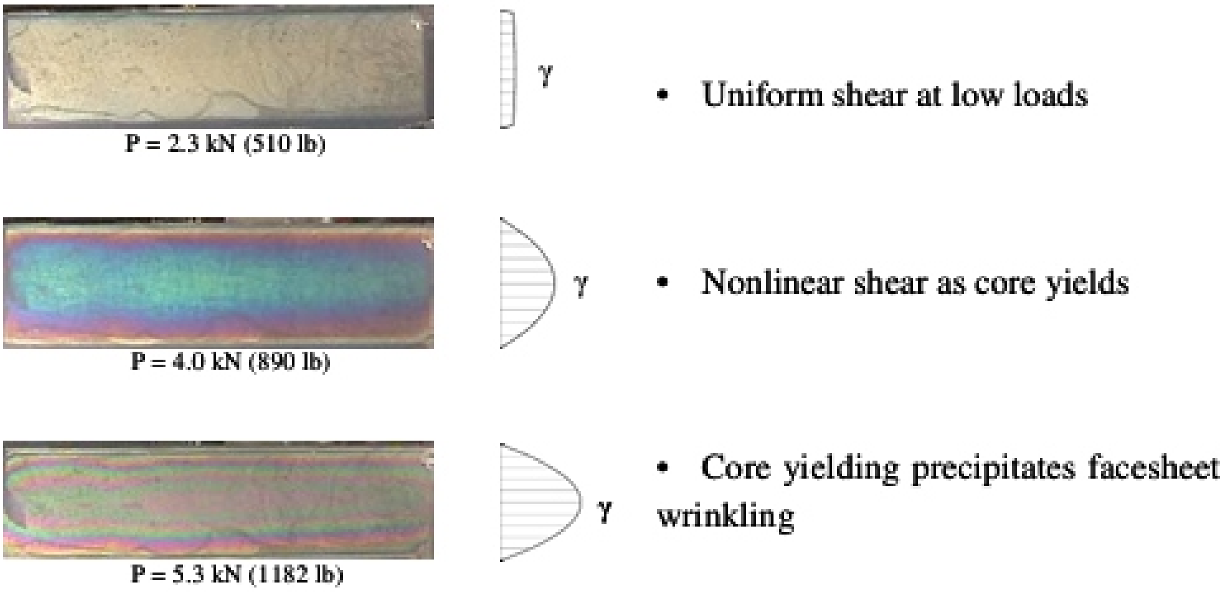

Figure 7. Isochromatic fringe patterns in birefringent coating of sandwich beam under three-point bending (Divinycell H250 core).

core is constant. This pattern remains uniform up to an applied load of 3.3kN which corresponds to an average shear stress in the core of 2.55MPa. This is close to the proportional limit of the shear stressstrain curve of the core material (Figure 3). For higher loads, the core begins to yield and the shear strain becomes highly nonuniform peaking at the center and causing plastic flow. The onset of core failure in beams is directly related to the core yield stress in the thickness direction. A critical condition for the core occurs at points where shear stress is combined with compressive stress.

The deformation and failure of the core is obviously dependent on its properties and especially its anisotropy. Honeycomb and balsa wood cores are highly anisotropic with much higher stiffness and strength in the thickness direction, a desirable property. Figure 8 shows isochromatic fringe patterns in the photoelastic coating and the corresponding load deflection curve for a composite sandwich beam under three-point bending. The beam consists of glass/vinylester facesheets and balsa wood core. The fringe patterns indicate that the shear deformation in the core is initially nearly uniform, but it becomes nonuniform and concentrated in a region between the support and the load at a distance of approximately one beam depth from the support. The pattern at the highest load shown is indicative of a vertical crack along the cells of the balsa wood core. The loads corresponding to the fringe patterns are marked on the load deflection curve. It is seen that the onset of nonlinear behavior corresponds to the beginning of fringe concentration and failure initiation in the critical region of the core. Figure 9 shows the damaged region of the beam. Although the fringe patterns did not show that, it appears that a crack was initiated near the upper facesheet/core interface and propagated parallel to it.

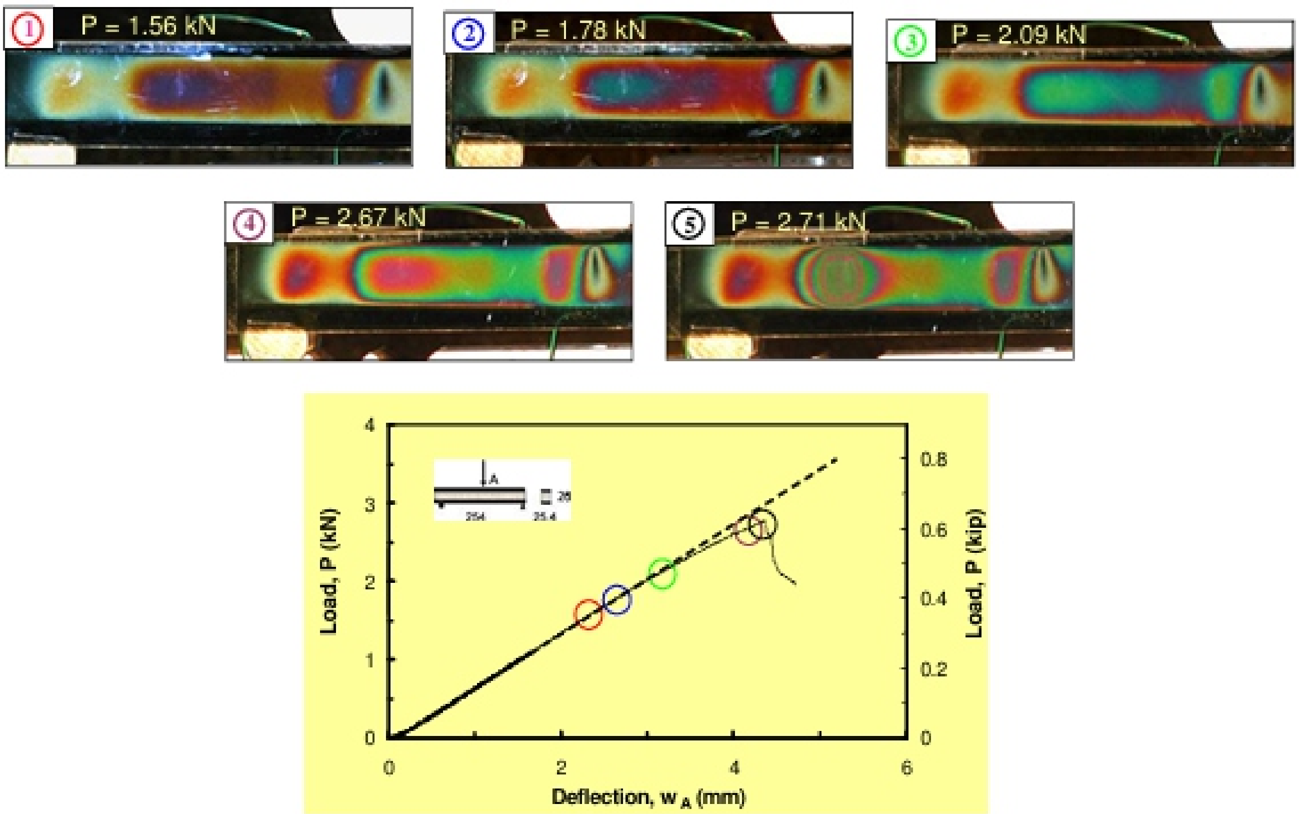

Figure 8. Isochromatic fringe patterns in photoelastic coating and load deflection curve of a composite sandwich beam under three-point bending (glass/vinylester facesheets; balsa wood core).

Figure 9. Cracking in balsa wood core of sandwich beam under three-point bending

The crack traveled for some distance and then turned downwards along the cell walls of the core until it approached the lower interface. It then traveled parallel to the interface towards the support point.

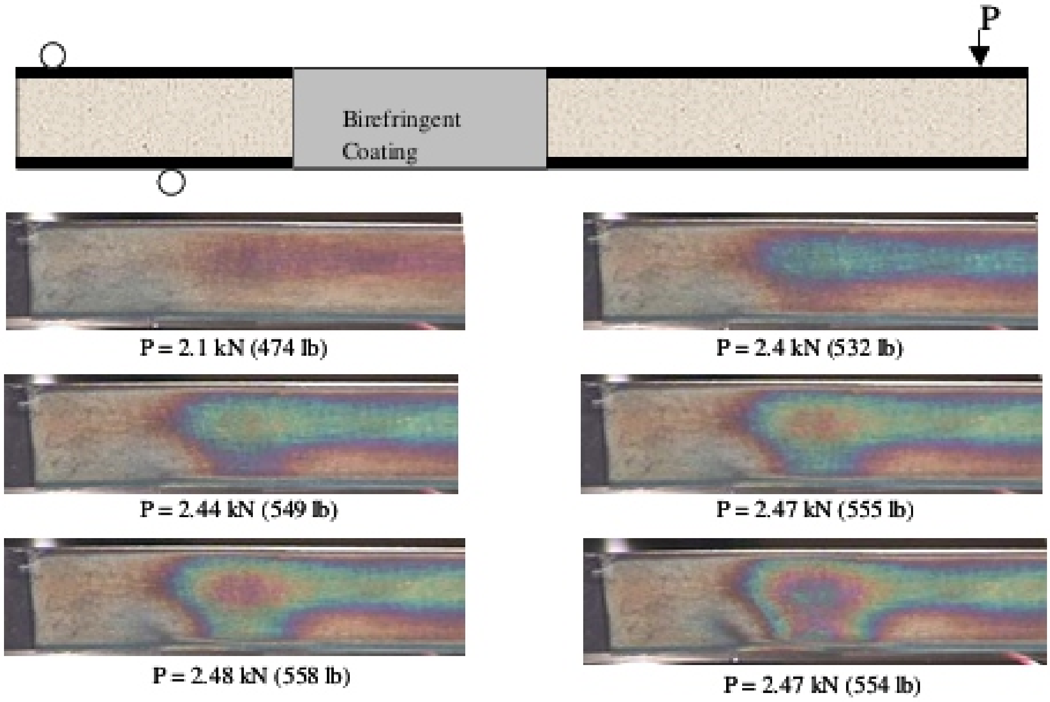

Figure 10. Isochromatic fringe patterns in birefringent coating of cantilever sandwich beam under end loading.

Core failure is accelerated when compressive and shear stresses are combined. This critical combination is evident from the failure envelope of Figure 4. The criticality of the compression/shear stress biaxiality was tested with a cantilever sandwich beam loaded at the free end. The isochromatic fringe patterns of the birefringent coating in Figure 10 show how the peak birefringence moves towards the fixed end of the beam at the bottom where the compressive strain is the highest and superimposed on the shear strain. Plastic deformation of the core, whether due to shear alone or a combination of compression and shear, degrades the supporting role of the core and precipitates other more catastrophic failure modes, such as facesheet wrinkling.

4. Indentation failure

Indentation failure in composite sandwich beams occurs under concentrated loads, especially in the case of soft cores. Under such conditions, significant local deformation takes place of the loaded facesheet into the core, causing high local stress concentrations. The indentation response of sandwich panels was first modeled by [Meyer-Piening 1989] who assumed linear elastic bending of the loaded facesheet resting on a Winkler foundation (core). Soden [1996] modeled the core as a rigid-perfectly plastic foundation, leading to a simple expression for the indentation failure load. Shuaeib and Soden [1997] predicted indentation failure loads for sandwich beams with glass-fiber-reinforced plastic facesheets and thermoplastic foam cores. The problem was modeled as an elastic beam, representing the facesheet, resting on an elastic-plastic foundation representing the core. Thomsen and Frostig [1997] studied the local bending effects in sandwich beams experimentally and analytically. The indentation failure of composite sandwich beams was also studied by [Anderson and Madenci 2000; Petras and Sutcliffe 2000; Gdoutos et al. 2002b].

For linear elastic behavior, the core is modeled as a layer of linear tension/compression springs. The stress at the core/facesheet interface is proportional to the local deflection w, $\sigma = kw$, where the foundation modulus k is given by

$$k = 0.64 \frac{E_c}{h_f} \sqrt[3]{\frac{E_c}{E_f}}, \tag{7}$$

and where E_f and E_c are the facesheet and core moduli, respectively, and h_f is the facesheet thickness. Initiation of indentation failure occurs when the core under the load starts yielding. The load at core yielding was calculated as

$$P_{cy} = 1.70 \sigma_{cy} b h_f \sqrt[3]{\frac{E_f}{E_c}}, \tag{8}$$

where σ_{cy} is the yield stress of the core, and b is the beam width.

Core yielding causes local bending of the facesheet which, combined with global bending of the beam, results in compression failure of the facesheet. The compressive failure stress in the facesheet is related to the critical beam loading P_{cr} by

$$\sigma_f = F_{fc} = \frac{9 P_{cr}^2}{16 b^2 h_f^2 F_{cc}} + \frac{P_{cr} L}{4 b h_f (h_f + h_c)}, \tag{9}$$

where h_c is the core thickness, L the span length, b the beam width, and F_{cc}, F_{fc} the compressive strengths of the core (in the thickness direction) and facesheet materials, respectively. In the above equation, the first term on the right hand side is due to local bending following core yielding and indentation and the second term is due to global bending.

The onset and progression of indentation failure is illustrated by the moiré pattern for a sandwich beam under three-point bending (Figure 11).

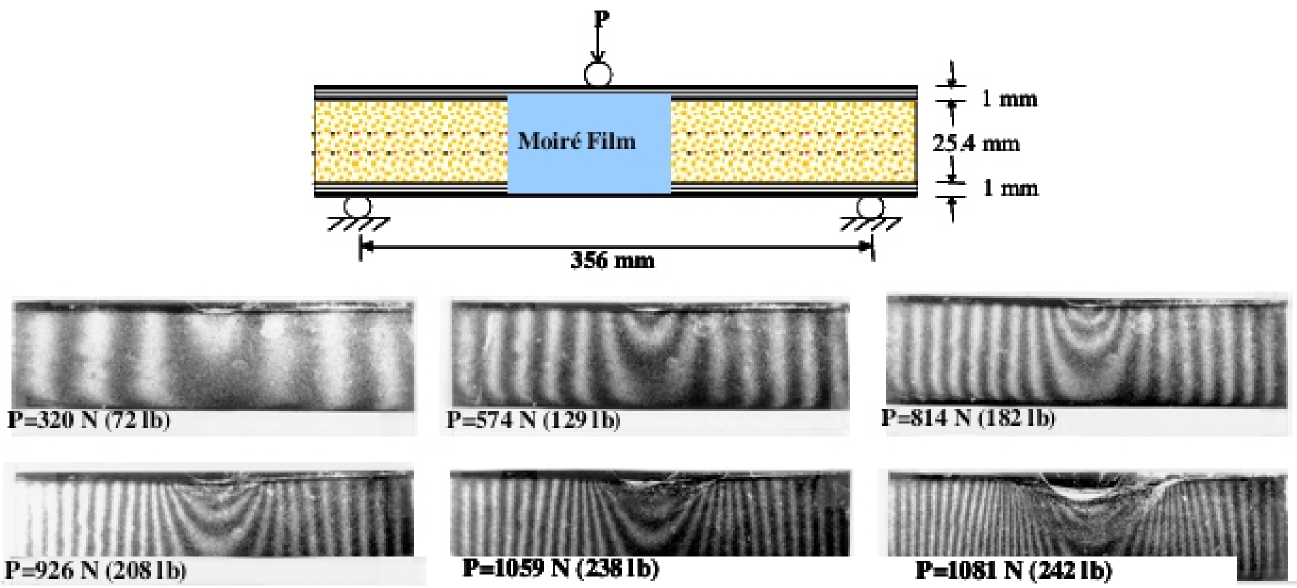

Figure 11. Moiré fringe patterns in sandwich beam with foam core corresponding to vertical displacements at various applied loads (11.8 lines/mm grating; carbon/epoxy facesheets; Divinycell H100 core).

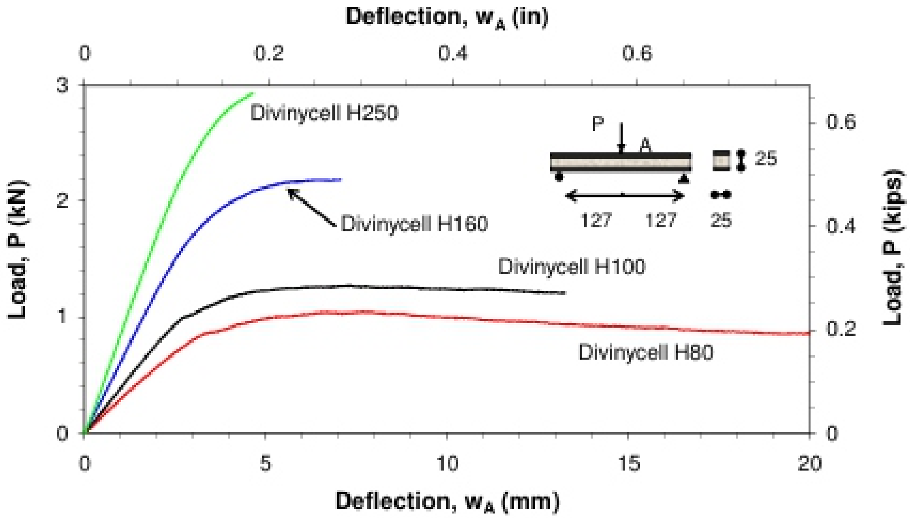

Figure 12. Load versus deflection under load of sandwich beam under three-point bending (carbon/epoxy facesheets, Divinycell cores).

Figure 12 shows load displacement curves for beams of the same dimensions but different cores. The displacement in these curves represents the sum of the global beam deflection and the more dominant local indentation. Therefore, the proportional limit of the load-displacement curves is a good indication of initiation of indentation.

The measured critical indentation loads in Figure 12 were compared with predicted values using (9), which can be approximated as [Soden 1996]

$$P_{\mathrm{cr}} \cong \tfrac{4}{3} b h_f \sqrt{F_{fc}\sigma_{cy}}. \tag{10}$$

Thus, the critical indentation load is proportional to the square root of the core material yield stress. The results obtained are compared in Table 2. The approximate theory with the assumption of rigid-perfectly plastic behavior overestimates the indentation failure load for soft cores, but it underestimates it for stiff cores.

5. Facesheet wrinkling failure

Wrinkling of sandwich beams subjected to compression or bending is defined as a localized short-wave length buckling of the compression facesheet. Wrinkling may be viewed as buckling of the compression facesheet supported on an elastic or elastoplastic continuum [Gdoutos et al. 2003]. It is a common failure mode leading to loss of the beam stiffness. The wrinkling phenomenon is characterized by the interaction

Indentation Load (N)	H80	H100	H160	H250
Measured	1050	1250	2150	2900
Calculated	1370	1500	2000	2380

Table 2. Critical indentation loads for sandwich beams with different cores under three-point bending.

between the core and the facesheet of the sandwich panel. Thus, the critical wrinkling load is a function of the stiffnesses of the core and facesheet, the geometry of the structure, and the applied loading.

A large number of theoretical and experimental investigations has been reported on wrinkling of sandwich structures. Some of the early works were presented and compiled in [Plantema 1966; Allen 1969]. Hoff and Mautner [1945] tested sandwich panels in compression and gave an approximate formula for the wrinkling stress, which depends only on the elastic moduli of the core and facesheet materials. Heath [1960] extended the theory for end loaded plates and proposed a simple expression for facesheet wrinkling in sandwich plates with isotropic components. The theory does not account for shear interaction between the facesheets and the core and thus is more applicable to compressively loaded sandwich columns and to beams under pure bending. Benson and Mayers [1967] developed a unified theory for the study of both general instability and facesheet wrinkling simultaneously for sandwich plates with isotropic facesheets and orthotropic cores. This theory was extended in [Hadi and Matthews 2000] to solve the problem of wrinkling of anisotropic sandwich panels. More studies on the wrinkling of sandwich plates are found in [Vonach and Rammerstorfer 2000; Fagerberg 2004; Birman and Bert 2004; Meyer-Piening 2006; Lopatin and Morozov 2008]. The critical wrinkling stress given in [Hoff and Mautner 1945] is

$$\sigma_{\mathrm{cr}} \cong c\sqrt[3]{E_{f1}E_{c3}G_{c13}}, \tag{11}$$

where E_{f1} and E_{c3} are the Young's moduli of facesheet and core, in the axial and through-thickness directions, respectively, G_{c13} is the shear modulus of the core on the 1-3 plane, and c is a coefficient, usually varying in the range of 0.5–0.9.

In the relation above, the core moduli are the initial ones while the material is in the linear range. After the core yields and its stiffnesses degrade (E'_c, G'_c), it does not provide adequate support for the facesheet, thereby precipitating facesheet wrinkling. The reduced critical stress after core degradation is

$$\sigma_{\mathrm{cr}} \cong c\sqrt[3]{E_f E'_c G'_c}. \tag{12}$$

Heath's original expression was modified here for a one-dimensional beam and by considering only the facesheet modulus along the axis of the beam and the core modulus in the through-thickness direction. The critical wrinkling stress can then be obtained by

$$\sigma_{\mathrm{cr}} = \left[\frac{2}{3}\frac{h_f}{h_c}E_{c3}E_f\right]^{1/2}. \tag{13}$$

Sandwich columns were subjected to end compression and strains were measured on both faces. The stress-strain curves for three columns with aluminum honeycomb, Divinycell H100 and Divinycell H250 cores are shown in Figure 13. Photographs of these columns after failure are shown in Figure 14. The wrinkling stress is defined as the stress at which the strain on the convex side of the panel reaches a maximum value. Note that the column with the honeycomb core failed by facesheet compression and not by wrinkling. The measured failure stress of 1,550 MPa is much lower than the critical wrinkling stresses of 2,850 MPa and 2,899 MPa predicted by (11) and (13), the former for $c = 0.5$. The columns with Divinycell H100 and H250 foam cores failed by facesheet wrinkling, as seen in the stress-strain curves of Figure 13. The measured wrinkling stresses at maximum strain for the Divinycell H100 and H250 cores were 627 MPa and 1,034 MPa, respectively, and are close to the values of 667 MPa and

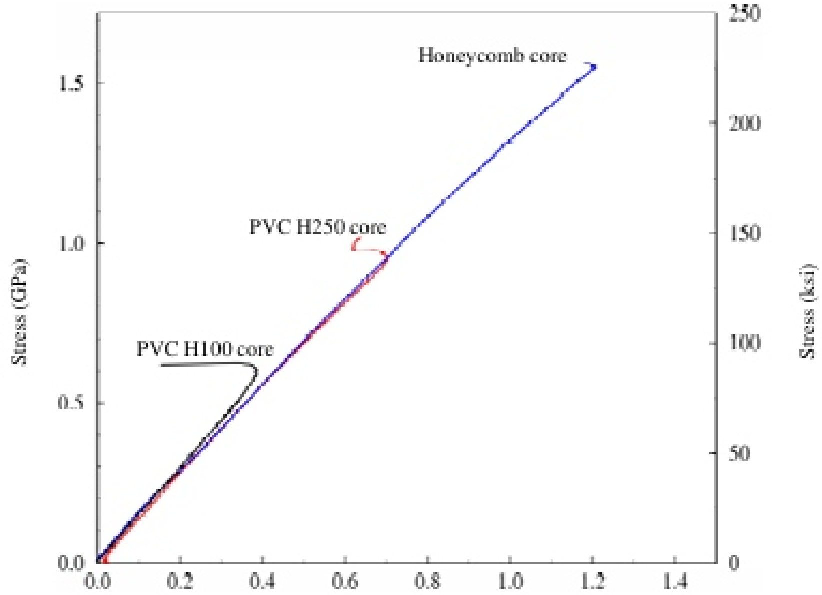

Figure 13. Compressive stress-strain curves for sandwich columns with different cores.

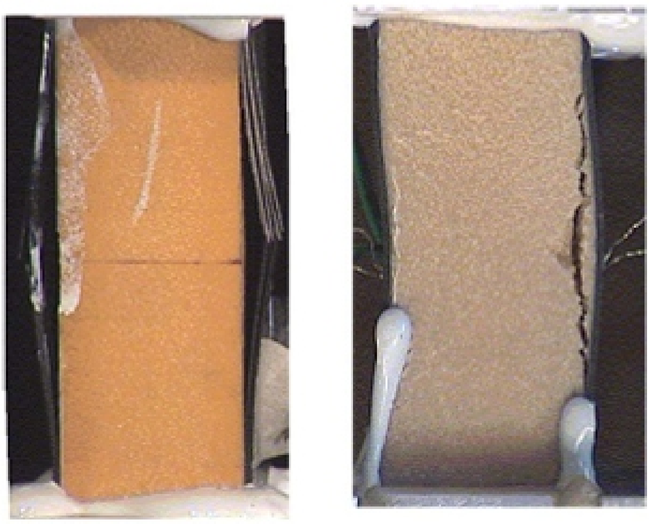

Figure 14. Failure of sandwich columns with two different cores.

1170 MPa predicted by (13). Agreement with the [Hoff and Mautner 1945] prediction would require coefficient values of $c = 0.834$ and $c = 0.662$ in (11).

Figure 15 shows moment versus strain results for two different tests of sandwich beams with Divinycell H100 foam cores under four-point bending. Evidence of wrinkling is shown by the sharp change in recorded strain on the compression facesheet, indicating inward and outward wrinkling in the two tests. In both cases the critical wrinkling stress was $\sigma_{\mathrm{cr}} = 673$ MPa. Heath's relation (13) [Heath 1960] was selected because of the lack of shear interaction due to the pure bending loading. The predicted critical wrinkling stress of 667 MPa is very close to the experimental value.

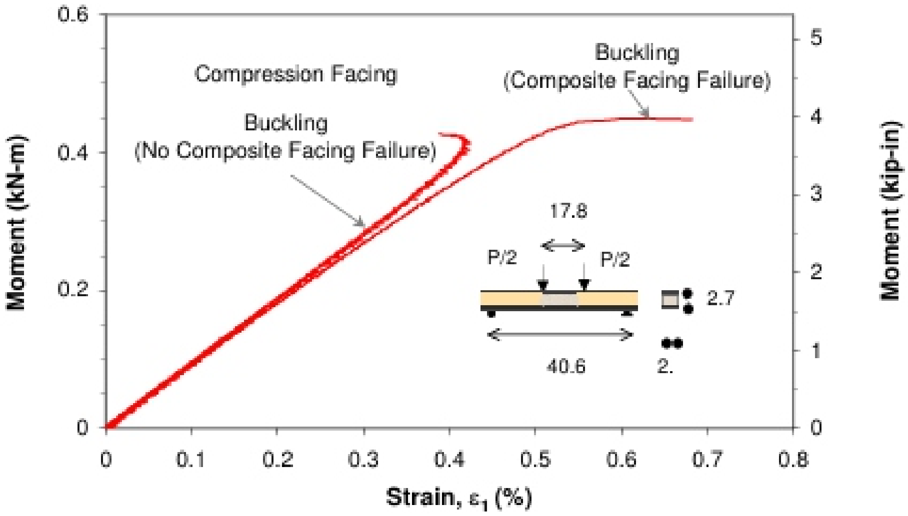

Figure 15. Facesheet wrinkling in sandwich beam under four-point bending (Divinycell H100 foam core; dimensions are in cm).

Sandwich beams were also tested in three-point bending and as cantilever beams. The moment-strain curves shown in Figure 16 illustrate the onset of facesheet wrinkling. Critical stresses obtained from the figure for the maximum moment for specimens 1 and 2 are $\sigma_{cr} = 860$ MPa and 947 MPa, respectively. The predicted value by (11) would agree with the average of the two measurements, 903 MPa, for $c = 0.578$. In the case of the short beam (specimen 3), core failure preceded wrinkling. The measured wrinkling stress was 517 MPa. The core shear stresses at wrinkling for specimens 2 and 3 are 3.2 MPa and 4.55 MPa, respectively. Thus, the core material for specimen 2 is in the linear elastic region, whereas for specimen 3 it is close to the yield point. Equation (14) predicts the measured wrinkling stress with a reduced core shear modulus of $G'_{c13} = 21.2$ MPa for $c = 0.5$.

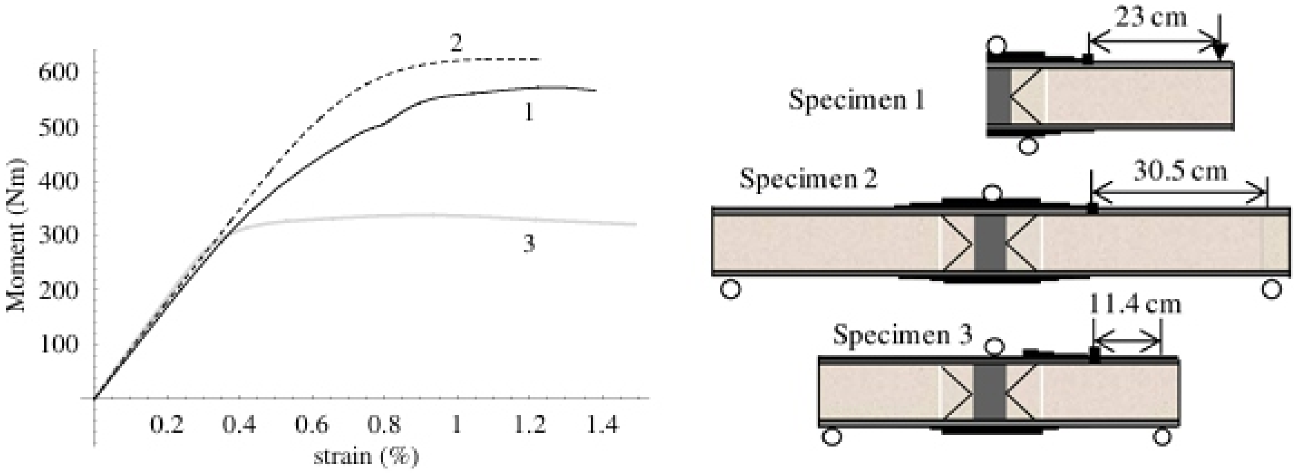

Figure 16. Facesheet wrinkling failure in sandwich beams with Divinycell H250 cores. Curve numbers correspond to specimen numbers on the right.

6. Conclusions

The initiation of failure in composite sandwich beams is heavily dependent on properties of the core material. Plastic yielding or cracking of the core occurs when the critical yield stress or strength (usually shear) of the core is reached. Indentation under localized loading depends principally on the square root of the core yield stress. Available theory predicts indentation failure approximately, overestimating it for soft cores and underestimating it for stiffer ones. The critical facesheet wrinkling stress is predicted fairly closely by Heath's formula for cases not involving shear interaction between the facesheets and the core, such as compressively loaded columns and beams under pure bending. In the case of cantilever beams or beams under three-point bending, entailing shear interaction between the facesheets and core, the Hoff and Mautner formula predicts a value for the critical wrinkling stress which is proportional to the cubic root of the product of the core Young's and shear moduli in the thickness direction. The ideal core should be highly anisotropic with high stiffness and strength in the thickness direction.

References

[Abot and Daniel 2003] J. L. Abot and I. M. Daniel, "Failure modes in glass/vinylester-balsa wood sandwich beams", pp. 851 859 in 6th International Conference on Sandwich Structures .ICSS-6/ (Fort Lauderdale, FL, 2003), edited by J. R. Vinson et al., CRC Press, Boca Raton, FL, 2003.

[Abot et al. 2002] J. L. Abot, I. M. Daniel, and E. E. Gdoutos, "Contact law for composite sandwich beams", J. Sandw. Struct. Mater. 4:2 (2002), 157–173.

[Allen 1969] H. G. Allen, Analysis and design of structural sandwich panels, Pergamon, London, 1969.

[Anderson and Madenci 2000] T. Anderson and E. Madenci, "Graphite/epoxy foam sandwich panels under quasi-static inden tation", Eng. Fract. Mech. 67:4 (2000), 329–344.

[Benson and Mayers 1967] A. S. Benson and J. Mayers, "General instability and face wrinkling of sandwich plates: unified theory and applications", AIAA J. 5:4 (1967), 729–739.

[Bezazi et al. 2007] A. Bezazi, A. El Mahi, J.-M. Berthelot, and B. Bezzazi, "Experimental analysis of behavior and damage of sandwich composite materials in three-point bending, 1: Static tests and stiffness degradation at failure studies", Strength Mater. 39:2 (2007), 170–177.

[Birman and Bert 2004] V. Birman and C. W. Bert, "Wrinkling of composite-facing sandwich panels under biaxial loading", J. Sandw. Struct. Mater. 6:3 (2004), 217–237.

[Daniel and Abot 2000] I. M. Daniel and J. L. Abot, "Fabrication, testing and analysis of composite sandwich beams", Compos. Sci. Technol. 60:12–13 (2000), 2455–2463.

[Daniel et al. 2001a] I. M. Daniel, E. E. Gdoutos, J. L. Abot, and K.-A. Wang, "Core failure modes in composite sandwich beams", pp. 293–303 in Contemporary research in engineering mechanics (New York, 2001), edited by G. A. Kardomateas and V. Birman, Aerospace Division/Applied Mechanics Division 65/249, ASME, New York, 2001.

[Daniel et al. 2001b] I. M. Daniel, E. E. Gdoutos, J. L. Abot, and K.-A. Wang, "Effect of loading conditions on deformation and failure of composite sandwich structures", pp. 1–17 in Three-dimensional effects in composite and sandwich structures (New York, 2001), edited by Y. D. S. Rajapakse, ASME, New York, 2001. Paper #AMD-25412.

[Daniel et al. 2002] I. M. Daniel, E. E. Gdoutos, K.-A. Wang, and J. L. Abot, "Failure modes of composite sandwich beams", Int. J. Damage Mech. 11:4 (2002), 309–334.

[Fagerberg 2004] L. Fagerberg, "Wrinkling and compression failure transition in sandwich panels", J. Sandw. Struct. Mater. 6:2 (2004), 129–144.

[Gdoutos et al. 2001] E. E. Gdoutos, I. M. Daniel, K.-A. Wang, and J. L. Abot, "Nonlinear behavior of composite sandwich beams in three-point bending", Exp. Mech. 41:2 (2001), 182–189.

[Gdoutos et al. 2002a] E. E. Gdoutos, I. M. Daniel, and K.-A. Wang, "Failure of cellular foams under multiaxial loading", Compos. A Appl. Sci. Manuf. 33:2 (2002), 163–176.

[Gdoutos et al. 2002b] E. E. Gdoutos, I. M. Daniel, and K.-A. Wang, "Indentation failure in composite sandwich structures", Exp. Mech. 42:4 (2002), 426–431.

[Gdoutos et al. 2003] E. E. Gdoutos, I. M. Daniel, and K.-A. Wang, "Compression facing wrinkling of composite sandwich structures", Mech. Mater. 35:3–6 (2003), 511–522.

[Hadi and Matthews 2000] B. K. Hadi and F. L. Matthews, "Development of Benson–Mayers theory on the wrinkling of anisotropic sandwich panels", Comput. Struct. 49:4 (2000), 425–434.

[Hall and Robson 1984] D. J. Hall and B. L. Robson, "A review of the design and materials evaluation programme for the GRP/foam sandwich composite hull of the RAN minehunter", Composites 15:4 (1984), 266–276.

[Heath 1960] W. G. Heath, "Sandwich construction: correlation and extension of existing theory of flat panels subjected to lengthwise compression", Aircr. Eng. Aerosp. Technol. 32:8 (1960), 230–235.

[Hoff and Mautner 1945] N. J. Hoff and S. E. Mautner, "The buckling of sandwich-type panels", J. Aeronaut. Sci. 12:3 (1945), 285–297.

[Lopatin and Morozov 2008] A. V. Lopatin and E. V. Morozov, "Symmetrical facing wrinkling of composite sandwich panels", J. Sandw. Struct. Mater. 10:6 (2008), 475–497.

[Meyer-Piening 1989] H.-R. Meyer-Piening, "Remarks on higher order sandwich stress and deflection analysis", pp. 107–127 in Sandwich constructions 1: proceedings of the 1st International Conference on Sandwich Construction (Stockholm, 1989), edited by K.-A. Olsson and R. P. Reichard, Engineering Materials Advisory Services, Cradley Heath, 1989.

[Meyer-Piening 2006] H.-R. Meyer-Piening, "Sandwich plates: stresses, deflection, buckling and wrinkling loads– a case study", J. Sandw. Struct. Mater. 8:5 (2006), 381–394.

[Petras and Sutcliffe 2000] A. Petras and M. P. F. Sutcliffe, "Indentation failure analysis of sandwich beams", Compos. Struct. 50:3 (2000), 311–318.

[Plantema 1966] F. J. Plantema, Sandwich construction: the bending and buckling of sandwich beams, plates, and shells, Airplane, Missile, and Spacecraft Structures 3, Wiley, New York, 1966.

[Sha et al. 2006] J. B. Sha, T. H. Yip, and J. Sun, "Responses of damage and energy of sandwich and multilayer beams composed of metallic face sheets and aluminum foam core under bending loading", Metall. Mater. Trans. A 37:8 (2006), 2419–2433.

[Shuaeib and Soden 1997] F. M. Shuaeib and P. D. Soden, "Indentation failure of composite sandwich beams", Compos. Sci. Technol. 57:9–10 (1997), 1249–1259.

[Soden 1996] P. D. Soden, "Indentation of composite sandwich beams", J. Strain Anal. Eng. Des. 31:5 (1996), 353–360.

[Thomsen and Frostig 1997] O. T. Thomsen and Y. Frostig, "Localized bending effects in sandwich panels: photoelastic investigation versus high-order sandwich theory results", Compos. Struct. 37:1 (1997), 97–108.

[Tsai and Wu 1971] S. W. Tsai and E. M. Wu, "A general theory of strength for anisotropic materials", J. Compos. Mater. 5:1 (1971), 58–80.

[Vonach and Rammerstorfer 2000] W. K. Vonach and F. G. Rammerstorfer, "The effects of in-plane core stiffness on the wrinkling behavior of thick sandwiches", Acta Mech. 141:1–2 (2000), 1–10.

[Zenkert 1995] D. Zenkert, An introduction to sandwich construction, Chameleon, London, 1995.

[Zenkert and Vikström 1992] D. Zenkert and M. Vikström, "Shear cracks in foam core sandwich panels: nondestructive testing and damage assessment", J. Compos. Tech. Res. 14:2 (1992), 95–103.

Received 17 Mar 2009. Accepted 18 Jun 2009.

ISAAC M. DANIEL: imdaniel@northwestern.edu

Departments of Civil and Mechanical Engineering, Northwestern University, 2137 Tech Drive, Evanston, IL, 60208-3020, United States

ISSN Application No. 21818

DIRECT DAMAGE-CONTROLLED DESIGN OF PLANE STEEL MOMENT-RESISTING FRAMES USING STATIC INELASTIC ANALYSIS

GEORGE S. KAMARIS, GEORGE D. HATZIGEORGIOU AND DIMITRI E. BESKOS

A new direct damage-controlled design method for plane steel frames under static loading is presented. Seismic loading can be handled statically in the framework of a push-over analysis. This method, in contrast to existing steel design methods, is capable of directly controlling damage, both local and global, by incorporating continuum damage mechanics for ductile materials in the analysis. The design process is accomplished with the aid of a two-dimensional finite element program, which takes into account material and geometric nonlinearities by using a nonlinear stress-strain relation through the beam-column f iber modeling and including P-and P-effects, respectively. Simple expressions relating damage to the plastic hinge rotation of member sections and the interstorey drift ratio for three performance limit states are derived by conducting extensive parametric studies involving plane steel moment-resisting frames under static loading. Thus, a quantitative damage scale for design purposes is established. Using the proposed design method one can either determine damage for a given structure and loading, or dimension a structure for a target damage and given loading, or determine the maximum loading for a given structure and a target damage level. Several numerical examples serve to illustrate the proposed design method and demonstrate its advantages in practical applications.

1. Introduction

Current steel design codes, such as AISC [1998] and EC3 [2005], are based on ultimate strength and the associated failure load. In both codes, member design loads are usually determined by global elastic analysis and inelasticity is taken into account indirectly through the interaction equations involving design loads and resistances defined for every kind of member deformation. Instability effects are also taken in an indirect and approximate manner through the use of the effective length buckling factor, while displacements are checked for serviceability at the end of the design process. Seismic design loads are obtained with the aid of seismic codes, such as AISC [2005] and EC8 [2004]. In this case the global analysis can be elastostastic as before, spectral dynamic, static inelastic (push-over) or nonlinear dynamic.

Damage of materials, members, and structures is defined as their mechanical degradation under loading. Control of damage is always desirable by design engineers. Even though current methods of design [AISC 1998; EC3 2005; AISC 2005; EC8 2004] are associated with ultimate strength and consider inelastic material behavior indirectly or directly, they are force-based and cannot achieve an effective control of damage, which is much better related to displacements than forces. For example, the percentage of the interstorey drift ratio (IDR) of seismically excited buildings is considered a solid basic indicator of the level of damage, as suggested by the HAZUS99-SR2 User's Manual [FEMA 2001]. Even the displacement-based seismic design method [Priestley et al. 2007], in which displacements play the fundamental role in design and are held at a permissible level (target displacements), does not lead into a direct and transparent control of damage.

To be sure, there are many works in the literature dealing with the determination of damage in members and structures, especially in connection with the seismic design of reinforced concrete structures. More specifically, damage determination of framed buildings at the local and global level can be done with the aid of damage indices computed on the basis of deformation and/or energy dissipation, as shown by Park and Ang [1985] and Powell and Allahabadi [1988], for example. On the other hand, the finite element method has been employed in the analysis of steel and reinforced concrete structures in conjunction with a concentrated inelasticity (plasticity and damage) beam element in [Florez-Lopez 1998]. Damage determination in reinforced concrete and masonry structures has also been done by employing continuum theories of distributed damage in the framework of the finite element method [Cervera et al. 1995; Hatzigeorgiou et al. 2001; Hanganu et al. 2002]. Note that in all these references, the approach is to determine damage as additional structural design information, and cannot lead to a structural design with controlled damage.

Here we extend the direct damage-controlled design (DDCD) method, first proposed in Hatzigeorgiou and Beskos [2007] for concrete structures, to structural steel design. The basic advantage of DDCD is the dimensioning of structures with damage directly controlled at both local and global levels. In other words, the designer can select a priori the desired level of damage in a structural member or a whole structure and direct his design in order to achieve this preselected level of damage. Thus, while the DDCD deals directly with damage, inelastic design approaches, such as [AISC 1998; EC3 2005; AISC 2005; Ec8 2004; Priestley et al. 2007] are concerned indirectly with damage. Furthermore, the a priori knowledge of damage, as it is the case with DDCD, ensures a controlled safety level, not only in strength but also in deflection terms. Thus, the present work, unlike all previous works on damage of steel structures, develops for the first time a direct damage-controlled steel design method, which is not just restricted to damage determination as an additional structural design information.

More specifically, the present work develops a design method for plane steel moment-resisting frames under static monotonic loading capable of directly controlling damage, both at local and global level. Seismic loading can be handled statically in the framework of a push-over analysis. Local damage is def ined pointwise and expressed as a function of deformation on the basis of continuum damage mechanics theory for ductile materials [Lemaitre 1992]. On the other hand, global damage definition is based on the demand-and-capacity-factor design format as well as on various member damage combination rules. The method is carried out with the aid of the two-dimensional finite element program DRAIN–2DX

[Prakash et al. 1993], which takes into account material and geometric nonlinearities, modified by the authors to employ damage as a design criterion in conjunction with appropriate damage levels. Material nonlinearities are implemented in the program by combining a nonlinear stress-strain relation for steel with the beam-column fibered plastic hinge modeling. Geometric nonlinearities involve P-and Peffects. Thus, the proposed method belongs to the category of design methods using advanced methods of analysis [Chen and Kim 1997; Kappos and Manafpour 2001; Vasilopoulos and Beskos 2006; 2009], which presents significant advantages over the code-based methods. Local buckling can be avoided by using only class 1 European steel sections, something which is compatible with the inelastic analysis employed herein. Furthermore, all structural members are assumed enough laterally braced in order to avoid lateral-torsional buckling phenomena. Using the proposed design method one can either determine damage for a given structure and loading, or dimension a structure for a target damage and given loading, or determine the maximum loading for a given structure and a target damage level.

2. Stress-strain relations for steel

Essential features of a steel constitutive model applicable to practical problems should be, on the one hand the accurate simulation of the actual steel behavior and on the other hand the simplicity in formulation and efficiency in implementation in a robust and stable nonlinear algorithmic manner. In this work, a multilinear stress-strain relation for steel characterized by a good compromise between simplicity and accuracy and a compatibility with experimental results, is adopted. The stress-strain . relation in tension for this steel model is of the form

$$\sigma = E\varepsilon \ \text{ for } \varepsilon \le \varepsilon_y, \qquad \sigma = \sigma_y + E_h(\varepsilon - \varepsilon_y) \ \text{ for } \varepsilon_y < \varepsilon \le \varepsilon_u, \qquad \sigma = \sigma_u \ \text{ for } \varepsilon_u < \varepsilon. \qquad (1)$$

Equation (1) describes a trilinear stress-strain relation representing elastoplastic behavior with hardening, as shown in Figure 1, with E and E_h being the elastic and the inelastic moduli, respectively, ε_y and ε_u the yield and the ultimate strains, respectively and σ_y and σ_u the yield and ultimate stress, respectively. The negative counterpart to (1) can be adopted for the compression stress state, as shown in Figure 1. Similar stress-strain curves have been proposed earlier by, for example, [Gioncu and Mazzolani 2002]; European and American steels exhibit a stress-strain behavior similar to that of Figure 1. Thus, the model (1) can effectively depict the true behavior of structural steel.

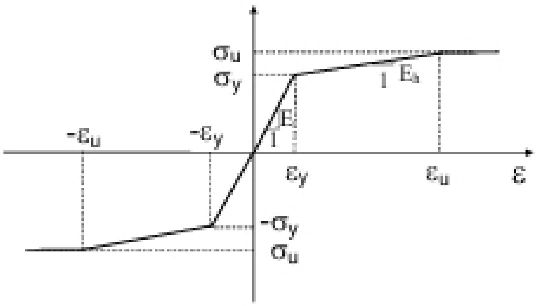

Figure 1. Stress-strain relation for steel.

3. Local damage

Local damage is usually referred to a point or a part of a structure and is one of the most appropriate indicators about their loading capacity. In the framework of continuum damage mechanics, the term "local" is associated with damage indices describing the state of the material at particular points of the structure, and the term "global" with damage indices describing the state of any finite material volume of the structure. Thus, global damage indices can be referred to any individual section, member, substructure, or the whole structure. This categorization of damage in agreement with continuum mechanics principles stipulating that constitutive models are defined at point level and all other quantities are obtained by integrating pointwise information.

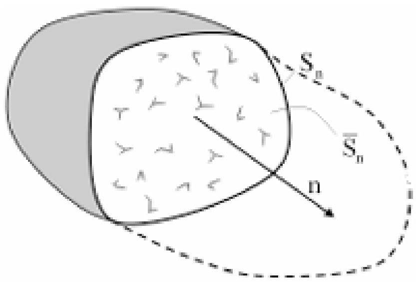

Figure 2. Cross section of a damaged material.

Continuum damage mechanics has been established for materials with brittle or ductile behavior and attempts to model macroscopically the progressive mechanical degradation of materials under different stages of loading. For structural steel, damage results from the nucleation of cavities due to decohesions between inclusions and the matrix followed by their growth and their coalescence through the phenomenon of plastic instability. The theory assumes that the material degradation process is governed by a damage variable d, the local damage index, which is defined pointwise, following Lemaitre [1992],

$$d = \lim_{S_n \to 0} \frac{S_n - \bar{S}_n}{S_n}, \tag{2}$$

where S_n stands for the overall section in a damage material volume, $\bar{S}_n$ for the effective or undamaged area, while $(S_n - \bar{S}_n)$ denotes the inactive area of defects, cracks, and voids (Figure 2). This index corresponds to the density of material defects and voids and has a zero value when the material is in the undamaged state and a value of unity at material rupture or failure.

The main goal of continuum damage mechanics is the determination of initiation and evolution of the damage index d during the deformation process. Lemaitre [1992], by assuming that damage evolution takes place only during plastic loading (plasticity induced damage) was able to propose a simple damage evolution law, as shown in Figure 3, which can successfully simulate the behavior of steel or other ductile materials. Damage index d is represented by a straight line in damage-strain space, with end points at $d = 0$ for $\varepsilon = \varepsilon_y$, and $d = 1$ for $\varepsilon = \varepsilon_u$, where strain values are assumed to be absolute. This damage evolution law can be expressed as

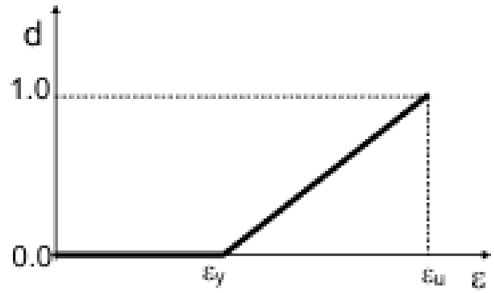

Figure 3. Damage-strain curve for steel.

A similar linear damage evolution law was proposed in [Florez-Lopez 1998]. Both laws are supported by experiments. One can observe that while the damage evolution law for concrete [Hatzigeorgiou and Beskos 2007] was derived by appropriately combining basic concepts of damage mechanics and a nonlinear stress-strain equation for plain concrete, the damage evolution law (3) for steel was taken directly from the literature [Lemaitre 1992].

4. Global damage

Global damage is referred to a section of a member, a member, a substructure, or a whole structure and constitutes one of the most suitable indicators about their loading capacity. Several methods to determine an indicator of damage at the global level have been presented in the literature. In general, these methods can be divided into four categories involving the following structural demand parameters: stiffness degradation, ductility demands, energy dissipation, and strength demands. According to the first approach, one of the most popular ways is to relate damage to stiffness degradation indirectly, that is, to the variation of the fundamental frequency of the structure during deformation [DiPasquale and Cakmak 1990]. However, this approach is inappropriate for the evaluation of the global damage of a substructure or its impact on the overall behavior. Furthermore, in order to evaluate the complete evolution of global damage with loading, a vast computational effort is needed due to the required eigenvalue analysis at every loading step. An alternative way to determine global damage is by computing the variation of the structural stiffness during deformation, as in [Ghobarah et al. 1999]; but again, evaluation of the global damage evolution requires heavy computations at every loading step. Many researchers determine damage in terms of the IDR. Whereas macroscopic quantities such as IDRs are good indicators of global damage in regular structures, this is not generally the case in more complex and/or irregular structures. Damage determination has also been done with the aid of damage indices computed on the basis of ductility (defined in terms of displacements, rotations or curvatures) and/or energy dissipation, as is evident in the method of [Park and Ang 1985] for framed concrete buildings or in the review article [Powell and Allahabadi 1988]. For the computation of damage in steel structures under seismic loading, one can mention [Vasilopoulos and Beskos 2006; Benavent-Climent 2007]. Note that all these indices are appropriate for seismic analyses only. They are not applicable to other types of problems, such as static ones; see [Hanganu et al. 2002].

In this work, for the section damage index Ds of a steel member, the following expression is proposed

$$D_S = \frac{c}{d} = \frac{\sqrt{(M_S - M_A)^2 + (N_S - N_A)^2}}{\sqrt{(M_B - M_A)^2 + (N_B - N_A)^2}}. \tag{4}$$

In the above, the bending moments MA, MS, and MB and the axial forces NA, NS, and NB as well as the distances c and d are those shown in the moment M– axial force N interaction diagram of Figure 4 for a plane beam-column element. The bending moment MS and axial force NS are design loads incorporating the appropriate load factors in agreement with EC3 [2005].

Figure 4 includes a lower bound damage curve, the limit between elastic and inelastic material behavior and an upper bound damage curve, the limit between inelastic behavior and complete failure. Thus, damage at the former curve is zero, while at the latter curve is one. Equation (4) is based on the assumption that damage evolution varies linearly between the above two damage bounds. These

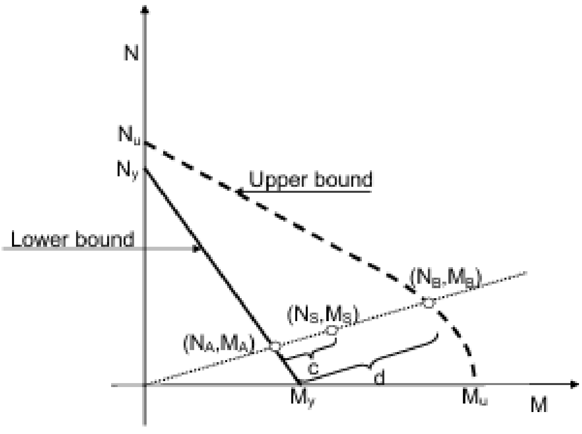

Figure 4. Section damage definition.

lower and upper bound curves can be determined accurately with the aid of the beam-column fibered plastic hinge modeling described in the next section. For their determination, the resistance safety factors are taken into account in agreement with EC3. The bound curves of Figure 4 can also be determined approximately by code type of formulae. Thus, the lower bound curve can be expressed as

$$\frac{M}{M_y} + \frac{N}{N_y} = 1, \tag{5}$$

where N_y and M_y are the minimum axial force and bending moment, respectively, which cause yielding, while the upper bound curve can be expressed as

$$\frac{M}{M_u} + \left(\frac{N}{N_u}\right)^2 = 1, \tag{6}$$

where N_u and M_u are the ultimate axial force and bending moment, respectively, which cause failure of the section. Equations (5) and (6) can be used for the construction of the bounding curves of Figure 4. The provisions in EC3 give a M-N interaction formula similar to (6), with the hardening effect not taken into account, that is, with $\sigma_u = \sigma_y$ or equivalently, $N_u = N_y$. Furthermore, since EC3 allows inelastic analysis only for section class 1, the proposed method is limited to sections of that class.

The section damage index proposed in (4) represents an extension of (3) from strains (or stresses) to forces and moments, i.e., stress resultants. Expressions for damage in terms of stress resultants are also mentioned in [Lemaitre 1992]. By contrast, Florez-Lopez [1998] uses *generalized effective stress*, which corresponds to bending moment, by analogy with the definition of *effective stress*, which corresponds to inelastic stress. His formulation, however, includes only bending moments, without any interaction with axial forces.

It should be noted that the proposed section damage index corresponds to the aforementioned fourth type of damage indicators, which are related to the strength demand approach. More specifically, this index is based on the demand-and-capacity-factor design format. There is an analogy or correspondence between the capacity ratio of interaction equations of EC3 and the proposed damage index; see Figure 4. This format is similar to the one implemented for performance evaluation of new and existing steel moment-resisting structures in the FEMA standards 350 and 351, respectively [FEMA 2000a; 2000b]. The member damage index D_M is taken as the largest section damage index, along the member. This is a traditional and effective assumption in structural design; see [Kappos and Manafpour 2001].

Therefore,

$$D_M = \max(D_S). \tag{7}$$

To provide an overall damage index that is representative of the damage state of a complex structure, the member damage indices must be combined in a rational manner to reflect both the severity of the member damage and the geometric distribution of damage within the overall structure. Various weighted-average procedures have been proposed for combining the member damage indices into an overall damage index. Thus, for a structure composed of m members, the overall damage index, D_O, has the form

$$D_O = \left(\frac{\sum_{i=1}^{m} D_{M,i}^2 W_i}{\sum_{i=1}^{m} W_i} \right)^{1/2}, \tag{8}$$

where $D_{M,i}$ and W_i denote the damage and weighting factor of the i-th member. This expression is in agreement with the fact that the most damaged members affect the overall damage much more than the undamaged (elastic) members. Park and Ang [1985], assuming that the distribution of damage is correlated with the distribution of plastic strain energy dissipation, applied (8) with the weighting factors to correspond to the amount of plastic strain energy dissipation. Similar assumptions have been proposed elsewhere; e.g., in [Powell and Allahabadi 1988]. However, all these approaches are exclusively applied to seismic problems where the external loads have a cyclic form. It is evident that the amount of plastic strain energy dissipation is an inappropriate measure for static monotonic problems. For this reason, the overall damage index D_O is assumed here to be of the form [Cervera et al. 1995]

$$D_O = \left(\frac{\sum_{i=1}^{m} D_{M,i}^2 \Omega_i}{\sum_{i=1}^{m} \Omega_i} \right)^{1/2}, \tag{9}$$

where Ω_i denotes the volume of the i-th member. This relation reflects both the severity of the member damage and the geometric distribution of damage within the structure.

5. Global damage levels

5.1. *Introduction.* Damage is used here as a design criterion. Thus, the designer, in addition to a method for determining damage, also needs a scale of damage in order to decide which level of damage is acceptable for his design. Many damage scales can be proposed in order to select desired damage levels associated with the strength degradation and capacity of a structure to resist further loadings. Table 1 provides the three performance levels, immediate occupancy (IO), life safety (LS), and collapse prevention (CP), associated with modern performance-based seismic design with the corresponding limit response values (performance objectives) in terms of interstorey drift ratio (IDR), θ_{pl} (plastic rotation at member end), μ_θ (local ductility), and d (damage) as well as the relevant references. The selection of the appropriate damage level depends on various factors, such as the importance factor or the "weak beams – strong columns" rule in seismic design of structures. Thus, for example, nuclear power plants should be designed with zero damage and plane frames with 60% and 30% maximum damage in beams and columns, respectively. The proposed design method uses the damage level scale that has been derived

Index	Source	Performance level IO	LS	CP
IDR	[Leelataviwat et al. 1999]	1–2%	2–3%	3–4%
	[SEAOC 1999]	1.5%	3.2%	3.8%
	[Vasilopoulos and Beskos 2006]	0.5%	1.5%	3%
(transient)	[FEMA 1997]	0.7%	2.5%	5%
(permanent)	[FEMA 1997]	negligible	1%	5%
θ_{pl}/θ_y	[FEMA 1997]	≤ 1	≤ 6	≤ 8
μ_θ	[FEMA 1997]	2	7	9
damage	[Vasilopoulos and Beskos 2006]	$\leq 5\%$	$\leq 20\%$	$\leq 50\%$
	[ATC 1985]	0.1–10%	10–30%	30–60%

Table 1. Performance levels and corresponding limit response values given by several sources.

with the aid of extensive parametric studies on plane frames and corresponds to the three performance levels of the FEMA 273 code [FEMA 1997]. It should be noted that damage characterizations (such as minor and major) given by modern seismic codes are qualitative and very general, and hence inappropriate for use in practical design. In contrast to them, the proposed values of damage indices can be easily used in practical design.

The following subsections provide details concerning the parametric studies conducted herein for the derivation of simple expressions relating damage to the plastic hinge rotation of the member sections and the IDR of the plane steel frames considered to be used for the construction of a practical quantitative damage scale.

5.2. *Frame geometry and loading.* A set of 36 plane steel moment-resisting frames was employed for the parametric studies. These frames are regular and orthogonal with storey heights and bay widths equal to 3 m and 5 m, respectively. Furthermore, they are characterized by a number of storeys n_s with values 3, 6, 9, 12, 15, and 20 and a number of bays n_b with values 3 and 6. The frames were subjected to constant uniform vertical loads $1.35G + 1.5Q = 30\,\text{kN/m}$ and horizontal variable loads $1.35W$, where G, Q, and W correspond to dead, live, and wind loads, respectively. The material properties taken from structural steel grade S235, were divided by a factor of 1.10 for compatibility with EC3 provisions. The frames were designed in accordance with EC3 [2005] and EC8 [2004].

Data for the frames, including values for n_s, n_b, beam and column sections, and first and second natural periods, are presented in the table on the next two pages, taken from [Karavasilis et al. 2007].

5.3. ***Proposed global damage level values.*** The previously described plane steel frames were analyzed by the computer program DRAIN–2DX [Prakash et al. 1993]. Use was made of its beam-column element with two possible plastic hinges at its ends modeled by fibers. During the analyses, the vertical loads of the frames remained constant, while the horizontal ones were progressively increased in order to identify the damage corresponding to each performance level of Table 1. Damage was calculated at section and structural levels by using expressions (4), (7), and (9). In addition, the interstorey drift ratio and the plastic hinge rotation at the end of each member were computed. The latter was computed in the form

#	n_s	n_b	columns and beams (see caption on next page)	T_1/sec	T_2/sec
1	3	3	240-330(1-3)	0.73	0.26
2	3	3	260-330(1-3)	0.69	0.21
3	3	3	280-330(1-3)	0.65	0.19
4	3	6	240-330(1-3)	0.75	0.23
5	3	6	260-330(1-3)	0.70	0.21
6	3	6	280-330(1-3)	0.66	0.20
7	6	3	280-360(1-4) 260-330(5-6)	1.22	0.41
8	6	3	300-360(1-4) 280-330(5-6)	1.17	0.38
9	6	3	320-360(1-4) 300-330(5-6)	1.13	0.37
10	6	6	280-360(1-4) 260-330(5-6)	1.25	0.42
11	6	6	300-360(1-4) 280-330(5-6)	1.19	0.40
12	6	6	320-360(1-4) 300-330(5-6)	1.15	0.38
13	9	3	340-360(1) 340-400(2-5) 320-360(6-7) 300-330(8-9)	1.55	0.54
14	9	3	360-360(1) 360-400(2-5) 340-360(6-7) 320-330(8-9)	1.52	0.53
15	9	3	400-360(1) 400-400(2-5) 360-360(6-7) 340-330(8-9)	1.46	0.51
16	9	6	340-360(1) 340-400(2-5) 320-360(6-7) 300-330(8-9)	1.57	0.55
17	9	6	360-360(1) 360-400(2-5) 340-360(6-7) 320-330(8-9)	1.53	0.53
18	9	6	400-360(1) 400-400(2-5) 360-360(6-7) 340-330(8-9)	1.47	0.51
19	12	3	400-360(1) 400-400(2-3) 400-450(4-5) 360-400(6-7) 340-400(8-9) 340-360(10) 340-330(11-12)	1.90	0.66
20	12	3	450-360(1) 450-400(2-3) 450-450(4-5) 400-450(6-7) 360-400(8-9) 360-360(10) 360-330(11-12)	1.78	0.62
21	12	3	500-360(1) 500-400(2-3) 500-450(4-5) 450-450(6-7) 400-400(8-9) 400-360(10-11) 400-330(12)	1.72	0.60
22	12	6	400-360(1) 400-400(2-3) 400-450(4-5) 360-400(6-7) 340-400(8-9) 340-360(10) 340-330(11-12)	1.90	0.67
23	12	6	450-360(1) 450-400(2-3) 450-450(4-5) 400-450(6-7) 360-400(8-9) 360-360(10) 360-330(11-12)	1.78	0.63
24	12	6	500-360(1) 500-400(2-3) 500-450(4-5) 450-450(6-7) 400-400(8-9) 400-360(10-11) 400-330(12)	1.72	0.61
25	15	3	500-300(1) 500-400(2-3) 500-450(4-5) 450-400(6-7) 400-400(8-12) 400-360(13-14) 400-330(15)	2.29	0.78
26	15	3	550-300(1) 550-400(2-3) 550-450(4-5) 500-400(6-7) 450-400(8-12) 450-360(13-14) 450-330(15)	2.22	0.75
27	15	3	600-300(1) 600-400(2-3) 600-450(4-5) 550-450(6-7) 500-450(8-9) 500-400(10-12) 500-360(13-14) 500-330(15)	2.10	0.72
28	15	6	500-300(1) 500-400(2-3) 500-450(4-5) 450-400(6-7) 400-400(8-12) 400-360(13-14) 400-330(15)	2.30	0.78
29	15	6	550-300(1) 550-400(2-3) 550-450(4-5) 500-400(6-7) 450-400(8-12) 450-360(13-14) 450-330(15)	2.21	0.75
30	15	6	600-300(1) 600-400(2-3) 600-450(4-5) 550-450(6-7) 500-450(8-9) 500-400(10-12) 500-360(13-14) 500-330(15)	2.10	0.72

#	n_s	n_b	columns and beams (see caption)	T_1/s	T_2/s
31	20	3	600-300(1) 600-400(2-3) 600-450(4-5) 550-450(6-10) 500-450(11-13) 500-400(14-16) 450-400(17) 450-360(18-19) 450-330(20)	2.82	0.97
32	20	3	650-300(1) 650-400(2-3) 650-450(4-5) 600-450(6-10) 550-450(11-13) 550-400(14-16) 500-400(17) 500-360(18-19) 500-330(20)	2.76	0.94
33	20	3	700-300(1) 700-360(2) 700-400(3) 700-450(4-5) 650-450(6-10) 600-450(11-13) 600-400(14-16) 550-400(17) 550-360(18-19) 550-330(20)	2.73	0.93
34	20	6	600-300(1) 600-400(2-3) 600-450(4-5) 550-450(6-10) 500-450(11-13) 500-400(14-16) 450-400(17) 450-360(18-19) 450-330(20)	2.75	0.96
35	20	6	650-300(1) 650-400(2-3) 650-450(4-5) 600-450(6-10) 550-450(11-13) 550-400(14-16) 500-400(17) 500-360(18-19) 500-330(20)	2.70	0.93
36	20	6	700-300(1) 700-360(2) 700-400(3) 700-450(4-5) 650-450(6-10) 600-450(11-13) 600-400(14-16) 550-400(17) 550-360(18-19) 550-330(20)	2.67	0.92

Table 2. Steel moment-resisting frames considered in parametric studies. In the central column, the expression 240-330(1-3) means that the first three storeys have columns with HEB240 sections and beams with IPE330 sections. The numbers in parentheses always refer to a range of storeys or single storey.

θ_{pl}/θ_y, where θ_y is the rotation at yielding expressed in FEMA [1997] as

$$\theta_y = \frac{M_{pl} L}{6EI}, \tag{10}$$

where L is the member length, E is the modulus of elasticity of the material and I is the moment of inertia of the section. When members, such as columns, are subjected to an axial compressive force P, the right-hand side of (10) is multiplied by the factor $1 - (P/P_y)$, where P_y is the axial yield force of the member.

This subsection presents the results of the parametric studies. Figure 5 shows the variation of the section damage index D_S versus the ratio θ_{pl}/θ_y for low-rise (3 and 6 storeys) and high-rise (9, 12, 15 and 20 storeys) frames, respectively. Figure 6 shows the variation of the overall damage index D_O versus IDR for low- and high-rise frames respectively. Using the method of least squares the mean values of these variations were determined and plotted as straight line segments in Figures 5–6. The analytical expressions of these lines are of the following form

For the low rise frames:

$$D_s = 12.526 \cdot \left(\frac{\theta_{pl}}{\theta_y}\right) \text{ for } \frac{\theta_{pl}}{\theta_y} \le 2.2 \qquad \text{and} \qquad D_s = 3.54 \cdot \left(\frac{\theta_{pl}}{\theta_y}\right) + 20.14 \text{ for } \frac{\theta_{pl}}{\theta_y} > 2.2 \tag{11}$$

$$D_O = 4.67 \cdot IDR. \tag{12}$$

For the high rise frames:

$$D_s = 2.42 \cdot \left(\frac{\theta_{pl}}{\theta_y}\right) \tag{13}$$

$$D_O = 0.94 \cdot IDR. \tag{14}$$

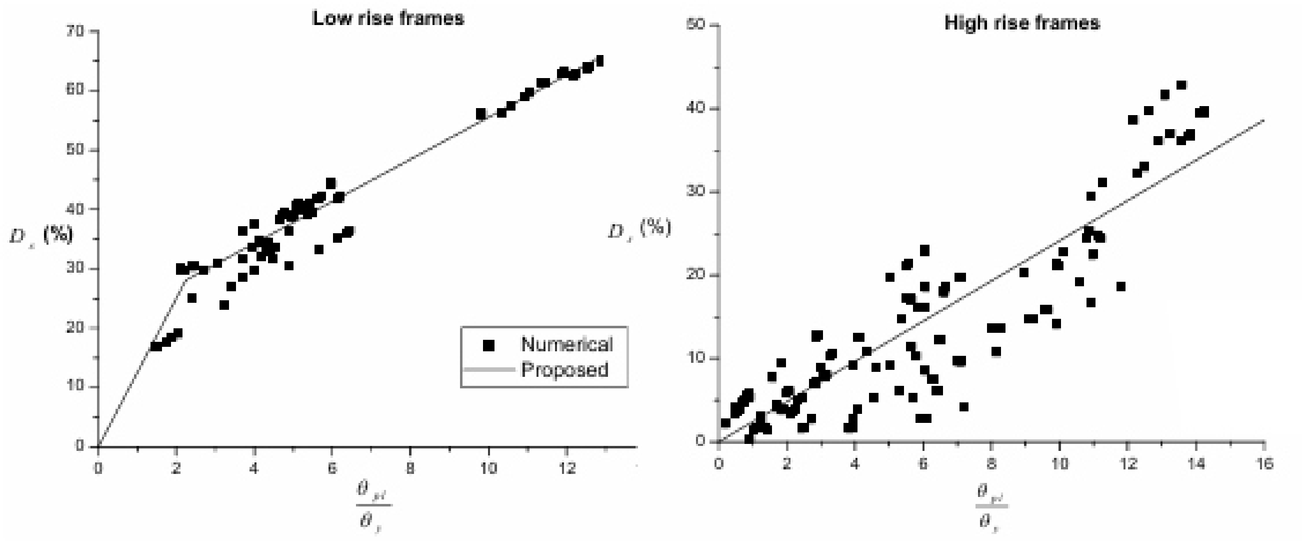

Figure 5. D_s versus θ_{pl}/θ_y curves for low- and high-rise frames.

The coefficient of determination R^2 in (11) and (13) is 0.96 and 0.79 respectively, showing that there is good correlation between the section damage and the plastic hinge rotation. On the contrary, the correlation between structure damage and the IDR is not so good as the coefficient of determination is 0.53 and 0.72 for (12) and (14), respectively.

Using the values of θ_{pl} and IDR given in FEMA [1997] for the three performance levels of Table 1 into (11)–(14), a section and overall damage scale is constructed for low- and high-rise frames and given in Table 4. The low values of damage in the high rise frames in that table can be explained by the instabilities caused in the analyses due to the concentration of damage in one or two sections and the P-δ and P-Δ effects. In the case of structural damage, this concentration combined with the definition of D_O in (9) explains these very small values. It is apparent from (9) that even if one has large values of

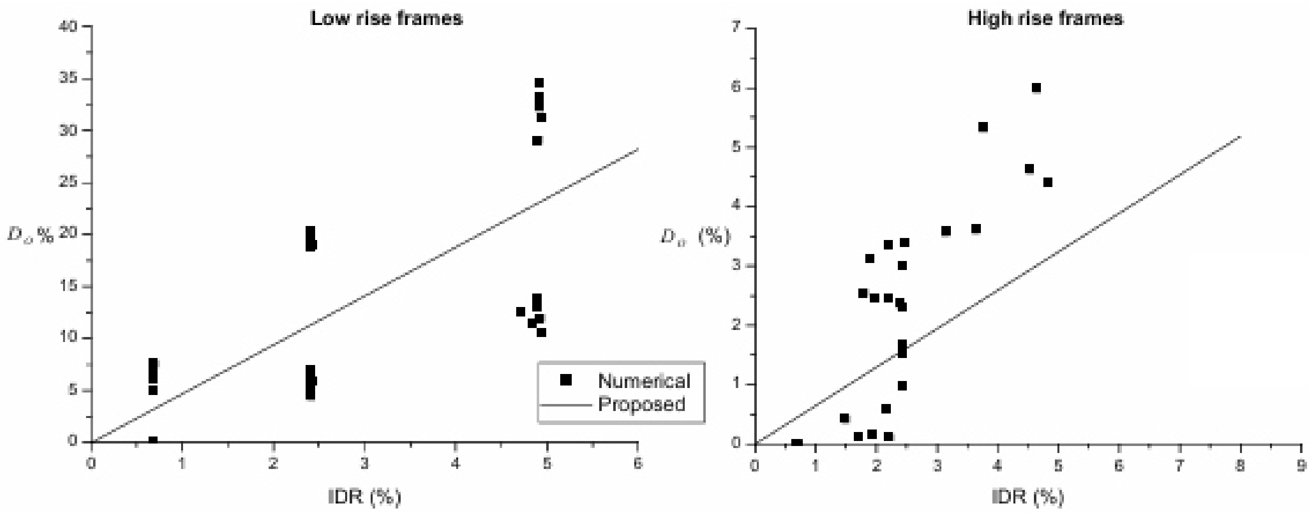

Figure 6. D_O versus IDR curves for low- and high-rise frames.

section damage in a few sections, the overall damage will have a small value because of the small or zero values in other sections. For this reason, the overall damage index is not considered as a representative one, and the section damage index is used in the applications.

6. Direct damage-controlled steel design

The application of the proposed DDCD method to plane steel members and framed steel structures is done with the aid of the DRAIN–2DX [Prakash et al. 1993] computer program, modified properly by the authors to perform both analysis and design. This program can statically analyze with the aid of the f inite element method plane beam structures taking into account material and geometric nonlinearities. Material nonlinearities are accounted for through fiber modeling of plastic hinges in a concentrated plasticity theory (element 15 of DRAIN–2DX). Geometric nonlinearities include the P-effect (influence of axial force acting through displacements associated with member bending) and the P-effect (influence of vertical load acting through lateral structural displacements), which are accounted for by utilizing the geometric stiffness matrix.

The beam-column section is subdivided in a user-defined number of steel fibers (Figure 7). Sensitivity studies have been undertaken to define the appropriate number of fibers for various types of sections. For example, for an I-section under axial force and uniaxial bending moment one can have satisfactory accuracy by dividing that section into 30fibers (layers). Thus, for every structural steel member, selected sections are divided into steel fibers and the stress–strain relationship of (1) is used for tension and compression.

In the analysis, every member of the structure needs to be subdivided into several elements (usually three or four) along its length to model the inelastic behavior more accurately. The analysis leads to highly accurate results, but is, in general, computationally intensive for large and complex structures. Figure 8 shows the flow chart of the modified DRAIN–2DX for damage-controlled steel design. Using this modified DRAIN–2DX, the user has three design options at his disposal in connection with damage-controlled steel design:

(i) determine damage for a given structure under given loading,

(ii) dimension a structure for given loading and given target damage, or

(iii) determine the maximum loading a given structure can sustain for a given target damage.

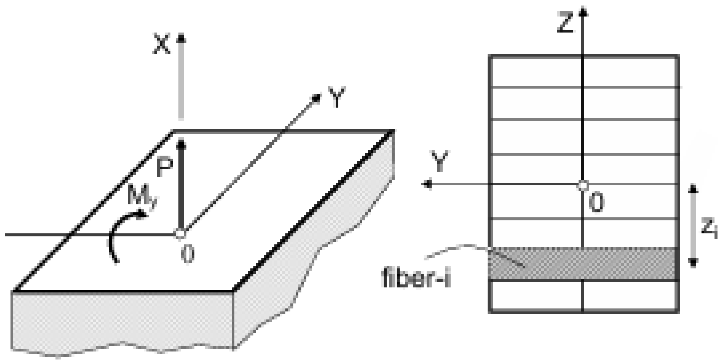

Figure 7. Fiber modeling of a general section.

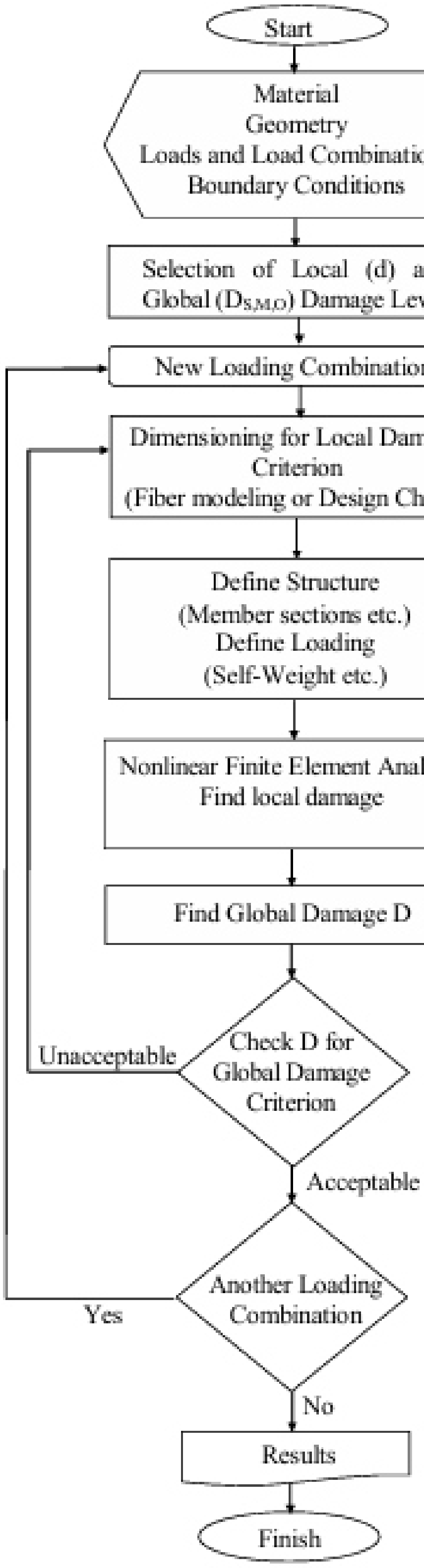

Figure 8. Flowchart of the modified program DRAIN–2DX [Prakash et al. 1993]

The first option is the one usually chosen in current practice. The other two options are the ones which actually make the proposed design method a direct damage-controlled one.

7. Examples of application

This section describes two numerical examples to illustrate the use of the proposed design method and demonstrate its advantages.

7.1. ***Static design of a plane steel frame.*** A plane two bay – two storey steel frame is examined in this example. Figure 9 shows the geometry and loading of the frame. Columns consist of standard HEB sections, while beams of standard IPE sections. The beams are subjected to uniform vertical loads $G = 15.0\,\text{kN/m}$ and $Q = 20.0\,\text{kN/m}$, where G and Q correspond to permanent and live loads, respectively. Additionally, the frame is subjected to horizontal wind loads $W = 12.6\,\text{kN}$ at the first floor level and $W = 22.2\,\text{kN/m}$ at the second. Steel is assumed to follow the material properties of steel grade S235 with trilinear stress-strain curve. Without loss of generality, only one loading combination of EC3 is examined here, that corresponding to $1.35(G + Q + W)$.

In the following, the frame is studied for the three design options of the proposed design method. Initially, the first design option, related to the determination of damage for a given structure and known loading, is examined. In this case, the structure is designed according to the EC3 method. In order to design this frame, four different member sections are determined, as shown in Figure 9: (a) columns of the first floor, (b) columns of the second floor, (c) beams of the first floor, and (d) beams of the second floor.

The most appropriate standard sections have been found to be those in Table 3. These sections have been obtained on the basis of a first order elastic analysis according to EC3. In order to determine the damage level, the structure is analyzed by the modified DRAIN–2DX program [Prakash et al. 1993], taking into account inelasticity and second order phenomena. The damage determined in all the members was found equal to zero (Table 3) indicating linear elastic behavior of the structure.

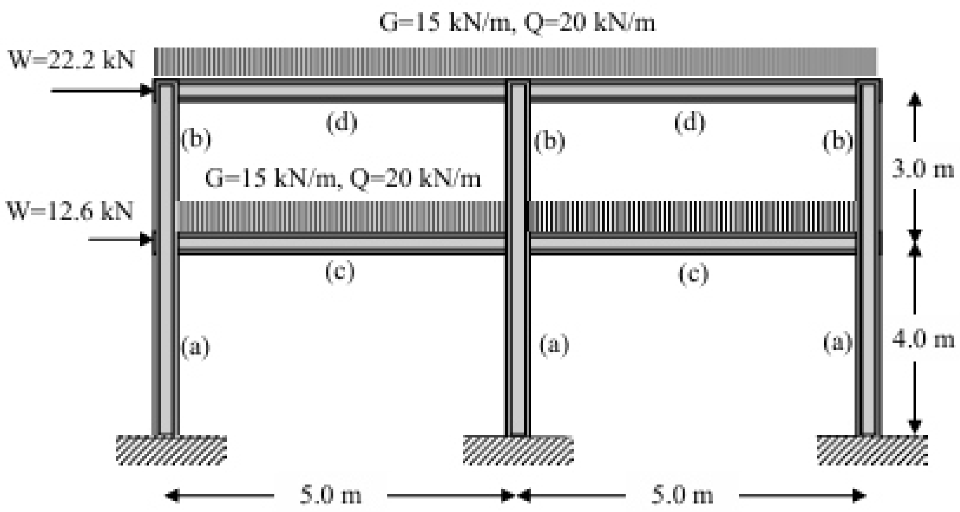

Figure 9. Geometry and loads for the frame of Section 7.1.

Member		EC3 Sections	EC3 Capacity ratio	EC3 Damage	Proposed method – DDCD Sections	Proposed method – DDCD Damage
columns	(a)	HEB-180	0.742	0.0%	HEB-160	0.0%
	(b)	HEB-140	0.821	0.0%	HEB-140	24.3%
beams	(c)	IPE-360	0.686	0.0%	IPE-240	73.7%
	(d)	IPE-330	0.842	0.0%	IPE-270	20.0%

Table 3. Design of two-dimensional frame for the structure of Figure 9.

The second design option has to do with member dimensioning for a preselected target damage level and known loading. Thus, using the modified DRAIN–2DX program, one can determine the most appropriate sections in order to have the selected target (maximum) damage at members, for the same loading combination as above. Two different damage levels are considered by setting the maximum member damage equal to 25% and 75% for columns and beams, respectively. The sections found appear in Table 3. For those sections, the computed values of maximum member damage D_S become 24.2% and 73.7% for columns and beams, very close from below to the preselected (target) values of 25% and 75%. It is evident that the acceptance of greater damage levels decreases the sizes of the sections.

Finally, the third design option associated with the determination of maximum loading for a given structure and preselected target damage is examined. Use is made again of the modified DRAIN–2DX program. The examined structure is assumed to consist of the standard sections obtained in the second design option (see Table 3). In this case, vertical (permanent and live) loads are assumed to remain the same. Thus, allowing maximum values of damage $D_S = 30\%$ and 0% for beams and columns, respectively, one can determine the maximum wind load. The allowable maximum wind load is found to be 11.5 and 20.2 kN for the first and second floor, respectively.

7.2. ***Seismic design of a plane steel frame by push-over.*** Consider an S235 plane steel moment-resisting frame of three bays and three storeys. The bay width is assumed to be 5 m and the storey height 3 m. The load combination $G + 0.3Q$ on beams is equal to 27.5 KN/m. HEB profiles are used for the columns and IPE profiles for the beams. The frame was designed according to EC3 [2005] and EC8 [2004] for a peak ground acceleration equal to 0.4 g, a soil class D and a behaviour factor $q = 4$ with the aid of the SAP2000 program [2005] in conjunction with the capacity design requirements of EC8. Thus, for a design base shear of 355 kN, the following column and beam sections were obtained for the three storeys: (HEB280-IPE360) + (HEB260-IPE330) + (HEB240-IPE300). The maximum elastic top floor displacement was found equal to 0.0465 m. Thus, according to EC8, the corresponding inelastic displacement will be $0.0465q = 0.186$ m, following the well known equal displacement rule.

The frame is subsequently analyzed using static inelastic push-over analysis with an inverted triangle type of profile of horizontal forces. The forces are progressively increased until the maximum inelastic displacement of the frame reaches the previously computed one of 0.186 m.

The damage distribution in the frame is shown in Figure 10. It is observed that plastic hinges are formed both in beams and columns, which implies that in reality the capacity design requirement is not satisfied. Damage values are up to about 47% in the beams and up to 26% in columns (44% at their

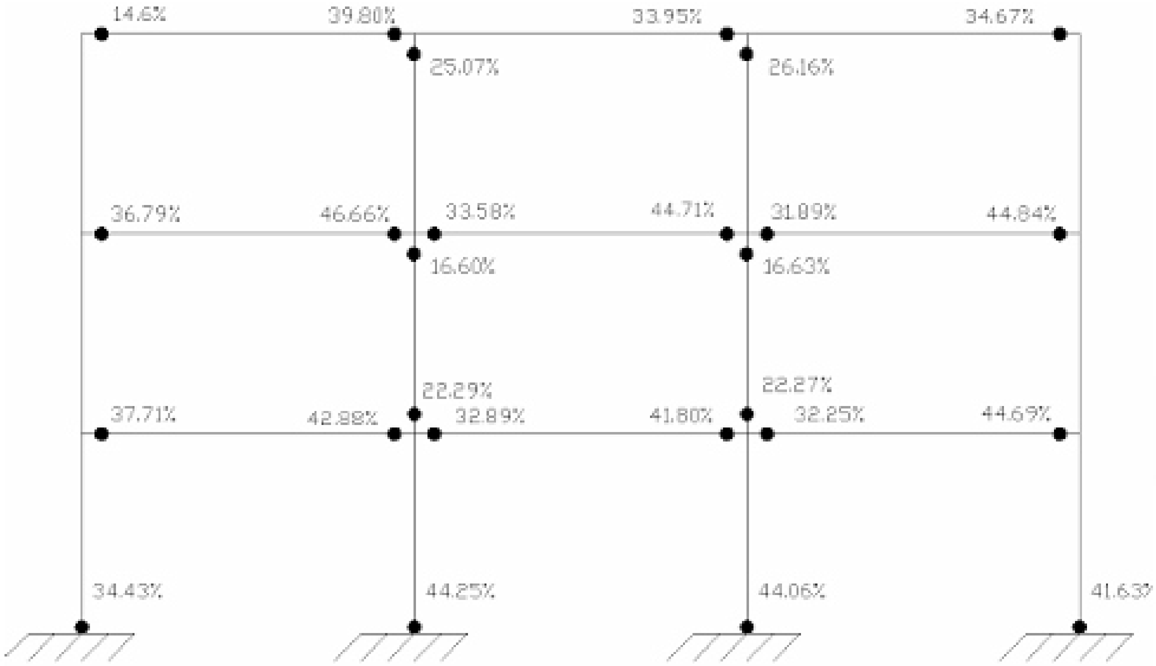

Figure 10. Damage distribution in the frame of Section 7.2 designed according to EC3 and EC8.

bases). The DDCD can overcome this drawback of formation of plastic hinges in the columns, because it can directly control damage and plastic hinge formation in the frame. Indeed, this frame is designed for the CP performance level of Table 4 by assuming target damage of 45% in the beams and 0% in all columns except those of the first floor where the target damage at their bases is 40%. For this target damage distribution and design base shear computed with the aid of the EC8 spectrum, the sections of the frame are obtained. For the resulting frame the push-over curve is used to determine the elastic displacement for the aforementioned base shear. This displacement is multiplied by q in order to find the maximum inelastic one and hence the corresponding base shear from the push-over curve. For this base shear the distribution of damage is obtained. If this distribution is in accordance with the target one, the selected sections are acceptable. Otherwise, the sections are changed and the previous procedure is repeated. Thus, for the damage distribution of Figure 11 with damage values up to about 44% in the beams and up to 37% in column bases, the column and beam sections for the three storeys of the frame were found to be (HEB300-IPE330) + (HEB300-IPE330) + (HEB280-IPE300). This selection results in a global collapse mechanism satisfying completely the capacity design requirement.

Performance level	Low rise frames D_s	Low rise frames D_O	High rise frames D_s	High rise frames D_O
IO	$\leq 13\%$	$\leq 3\%$	$\leq 3\%$	$\leq 1\%$
LS	$\leq 40\%$	$\leq 12\%$	$\leq 15\%$	$\leq 2\%$
CP	$\leq 50\%$	$\leq 24\%$	$\leq 20\%$	$\leq 5\%$

Table 4. Performance levels and corresponding section and structural damage.

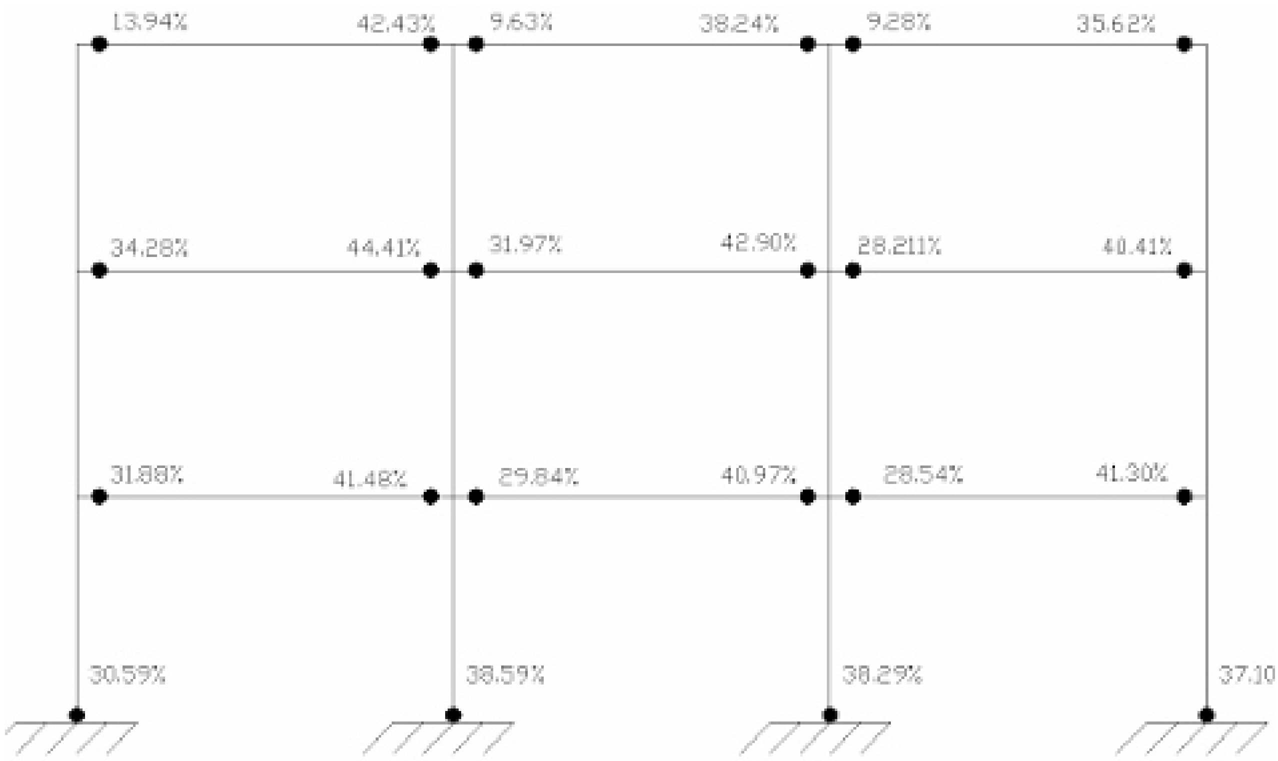

Figure 11. Damage distribution in the frame of Section 7.2 designed according to DDCD

8. Conclusions

This paper introduced the direct damage-controlled design (DDCD) method for structural steel design. The method

1.works with the aid of the finite element method incorporating material and geometric nonlinearities, a continuum mechanics definition of damage and a damage scale derived on the basis of extensive parametric studies;

2. allows the designer to either determine the damage level for a given structure and known loading, or dimension a structure for a target damage level and known loading, or determine the maximum loading for a given structure and a target damage level;

3.can also be used for the case of seismic loading in the framework of the static inelastic (push-over) analysis providing a reliable way for achieving seismic capacity design.

References

[AISC 1998] "Load and resistance factor design: structural members, specifications and codes", 2nd revision of the 2nd ed., American Institute of Steel Construction, Chicago, 1998.

[AISC 2005] "Seismic provisions for structural steel buildings", standard AISC 341-05, American Institute of Steel Construc tion, Chicago, 2005.

[ATC 1985] "Earthquake damage evaluation data for California", standard ATC-13, Applied Technology Council, Redwood City, CA, 1985.

[Benavent-Climent 2007] A. Benavent-Climent, "An energy-based damage model for seismic response of steel structures", Earthquake Eng. Struct. Dyn. 36:8 (2007), 1049–1064

[Cervera et al. 1995] M. Cervera, J. Oliver, and R. Faria, "Seismic evaluation of concrete dams via continuum damage models", Earthquake Eng. Struct. Dyn. 24:9 (1995), 1225–1245.

[Chen and Kim 1997] W. F. Chen and S. E. Kim, LRFD steel design using advanced analysis, CRC Press, Boca Raton, FL, 1997.

[DiPasquale and Cakmak 1990] E. DiPasquale and A. S. Cakmak, "Detection of seismic structural damage using parameter based global damage indices", Probab. Eng. Mech. 5:2 (1990), 60–65.

[EC3 2005] "Eurocode 3: Design of steel structures, part 1-1: general rules for buildings", standard EN 1993-1-1, European Committee on Standardization (CEN), Brussels, 2005.

[EC8 2004] European Committee for Standardization (CEN), "Eurocode 8: design of structures for earthquake resistance, part 1: general rules, seismic actions and rules for buildings", standard EN 1998-1, Brussels, 2004.

[FEMA 1997] "NEHRP guidelines for the seismic rehabilitation of buildings", standard FEMA-273, Building Seismic Safety Council, Federal Emergency Management Agency (FEMA), Washington, D.C., 1997, Available at http://www.wbdg.org/ccb/ FEMA/ARCHIVES/fema273.pdf.

[FEMA2000a] FEMA, "Recommended seismic design criteria for new steel moment-frame buildings", standard FEMA-350, Federal Emergency Management Agency (FEMA), Sacramento, CA, 2000, Available at http://www.fema.gov/plan/prevent/ earthquake/pdf/fema-350.pdf.

[FEMA 2000b] FEMA, "Recommended seismic evaluation and upgrade criteria for existing welding steel moment-frame buildings", standard FEMA-351, Federal Emergency Management Agency (FEMA), Washington, D.C., 2000, Available at http://www.fema.gov/plan/prevent/earthquake/pdf/fema-351.pdf.

[FEMA 2001] "HAZUS99 User's manual", Service Release 2, Federal Emergency Management Agency (FEMA), Washington, D.C., 2001.

[Florez-Lopez 1998] J. Florez-Lopez, "Frame analysis and continuum damage mechanics", Eur. J. Mech. A Solids 17:2 (1998), 269–283.

[Ghobarah et al. 1999] A. Ghobarah, H. Abou-Elfath, and A. Biddah, "Response-based damage assessment of structures", Earthquake Eng. Struct. Dyn. 28:1 (1999), 79–104.

[Gioncu and Mazzolani 2002] V. Gioncu and F. M. Mazzolani, Ductility of seismic resistant steel structures, Spon Press, London, 2002.

[Hanganu et al. 2002] A. D. Hanganu, E. Onate, and A. H. Barbat, "A finite element methodology for local/global damage evaluation in civil engineering structures", Comput. Struct. 80:20-21 (2002),

1667–1687.

[Hatzigeorgiou and Beskos 2007] G. D. Hatzigeorgiou and D. E. Beskos, "Direct damage-controlled design of concrete structures", J. Struct. Eng. (ASCE) 133:2 (2007), 205–215.

[Hatzigeorgiou et al. 2001] G. D. Hatzigeorgiou, D. E. Beskos, D. D. Theodorakopoulos, and M. Sfakianakis, "A simple concrete damage model for dynamic FEM applications", Int. J. Comput. Eng. Sci. 2:2 (2001), 267–286.

[Kappos and Manafpour 2001] A. J. Kappos and A. Manafpour, "Seismic design of R/C buildings with the aid of advanced analytical techniques", Eng. Struct. 23:4 (2001), 319–332.

[Karavasilis et al. 2007] T. L. Karavasilis, N. Bazeos, and D. E. Beskos, "Behavior factor for performance-based seismic design of plane steel moment resisting frames", J. Earthq. Eng. 11:4 (2007), 531–559.

[Leelataviwat et al. 1999] S. Leelataviwat, S. C. Goel, and B. Stojadinovi´c, "Toward performance-based seismic design of structures", Earthquake Spectra 15:3 (1999), 435–461.

[Lemaitre 1992] J. Lemaitre, A course on damage mechanics, Springer-Verlag, Berlin, 1992.

[Park and Ang 1985] Y. J. Park and A. H. S. Ang, "Mechanistic seismic damage model for reinforced concrete", J. Struct. Eng. .ASCE/ 111:4 (1985), 722–739.

[Powell and Allahabadi 1988] G. H. Powell and R. Allahabadi, "Seismic damage prediction by deterministic methods: concepts and procedures", Earthquake Eng. Struct. Dyn. 16:5 (1988), 719–734.

[Prakash et al. 1993] V. Prakash, G. H. Powell, and S. Campbell, DRAIN-2DX base program description and user guide, version 1.10, University of California, Berkeley, CA, 1993.

[Priestley et al. 2007] M. J. N. Priestley, G. M. Calvi, and M. J. Kowalsky, Displacement-based seismic design of structures, IUSS Press, Pavia, Italy, 2007.

[SAP2000 2005] SAP2000: Static and dynamic finite element analysis of structures, version 9.1.4, Computers and Structures, Inc., Berkeley, CA, 2005.

[SEAOC 1999] "Recommended lateral force requirements and commentary", known as the SEAOC Blue Book, 7th ed., Seismology Committee, Structural Engineers Association of California, Sacramento, CA, 1999.

[Vasilopoulos and Beskos 2006] A. A. Vasilopoulos and D. E. Beskos, "Seismic design of plane steel frames using advanced methods of analysis", Soil Dyn. Earthq. Eng. 26:12 (2006), 1077–1100. Corrigendum in 27:2 (2007), 189.

[Vasilopoulos and Beskos 2009] A. A. Vasilopoulos and D. E. Beskos, "Seismic design of space steel frames using advanced methods of analysis", Soil Dyn. Earthq. Eng. 29:1 (2009), 194–218.

Received 8 Dec 2008. Accepted 13 Mar 2009.

GEORGE S. KAMARIS: kamaris@upatras.gr

Department of Civil Engineering, University of Patras, 26500 Patras, Greece
GEORGE D. HATZIGEORGIOU: gchatzig@env.duth.gr
Department of Environmental Engineering, Democritus University of Thrace, 67100 Xanthi, Greece
DIMITRI E. BESKOS: d.e.beskos@upatras.gr
Department of Civil Engineering, University of Patras, 26500 Patras, Greec

Instructions for Authors

Essentials for Publishing in this Journal

1 Submitted articles should not have been previously published or be currently under consideration for publication elsewhere.

2 Conference papers may only be submitted if the paper has been completely re-written (taken to mean more than 50%) and the author has cleared any necessary permission with the copyright owner if it has been previously copyrighted.

3 All our articles are refereed through a double-blind process.

4 All authors must declare they have read and agreed to the content of the submitted article and must sign a declaration correspond to the originality of the article.

Submission Process

All articles for this journal must be submitted using our online submissions system. http://enrichedpub.com/ . Please use the Submit Your Article link in the Author Service area.

Manuscript Guidelines

The instructions to authors about the article preparation for publication in the Manuscripts are submitted online, through the e-Ur (Electronic editing) system, developed by **Enriched Publications Pvt. Ltd**. The article should contain the abstract with keywords, introduction, body, conclusion, references and the summary in English language (without heading and subheading enumeration). The article length should not exceed 16 pages of A4 paper format.

Title

The title should be informative. It is in both Journal's and author's best interest to use terms suitable. For indexing and word search. If there are no such terms in the title, the author is strongly advised to add a subtitle. The title should be given in English as well. The titles precede the abstract and the summary in an appropriate language.

Letterhead Title

The letterhead title is given at a top of each page for easier identification of article copies in an Electronic form in particular. It contains the author's surname and first name initial .article title, journal title and collation (year, volume, and issue, first and last page). The journal and article titles can be given in a shortened form.

Author's Name

Full name(s) of author(s) should be used. It is advisable to give the middle initial. Names are given in their original form.

Contact Details

The postal address or the e-mail address of the author (usually of the first one if there are more Authors) is given in the footnote at the bottom of the first page.

Type of Articles

Classification of articles is a duty of the editorial staff and is of special importance. Referees and the members of the editorial staff, or section editors, can propose a category, but the editor-in-chief has the sole responsibility for their classification. Journal articles are classified as follows:

Scientific articles:

1. Original scientific paper (giving the previously unpublished results of the author's own research based on management methods).
2. Survey paper (giving an original, detailed and critical view of a research problem or an area to which the author has made a contribution visible through his self-citation);
3. Short or preliminary communication (original management paper of full format but of a smaller extent or of a preliminary character);
4. Scientific critique or forum (discussion on a particular scientific topic, based exclusively on management argumentation) and commentaries. Exceptionally, in particular areas, a scientific paper in the Journal can be in a form of a monograph or a critical edition of scientific data (historical, archival, lexicographic, bibliographic, data survey, etc.) which were unknown or hardly accessible for scientific research.

Professional articles:

1. Professional paper (contribution offering experience useful for improvement of professional practice but not necessarily based on scientific methods);
2. Informative contribution (editorial, commentary, etc.);
3. Review (of a book, software, case study, scientific event, etc.)

Language

The article should be in English. The grammar and style of the article should be of good quality. The systematized text should be without abbreviations (except standard ones). All measurements must be in SI units. The sequence of formulae is denoted in Arabic numerals in parentheses on the right-hand side.

Abstract and Summary

An abstract is a concise informative presentation of the article content for fast and accurate Evaluation of its relevance. It is both in the Editorial Office's and the author's best interest for an abstract to contain terms often used for indexing and article search. The abstract describes the purpose of the study and the methods, outlines the findings and state the conclusions. A 100- to 250-Word abstract should be placed between the title and the keywords with the body text to follow. Besides an abstract are advised to have a summary in English, at the end of the article, after the Reference list. The summary should be structured and long up to 1/10 of the article length (it is more extensive than the abstract).

Keywords

Keywords are terms or phrases showing adequately the article content for indexing and search purposes. They should be allocated heaving in mind widely accepted international sources (index, dictionary or thesaurus), such as the Web of Science keyword list for science in general. The higher their usage frequency is the better. Up to 10 keywords immediately follow the abstract and the summary, in respective languages.

Acknowledgements

The name and the number of the project or programmed within which the article was realized is given in a separate note at the bottom of the first page together with the name of the institution which financially supported the project or programmed.

Tables and Illustrations

All the captions should be in the original language as well as in English, together with the texts in illustrations if possible. Tables are typed in the same style as the text and are denoted by numerals at the top. Photographs and drawings, placed appropriately in the text, should be clear, precise and suitable for reproduction. Drawings should be created in Word or Corel.

Citation in the Text

Citation in the text must be uniform. When citing references in the text, use the reference number set in square brackets from the Reference list at the end of the article.

Footnotes

Footnotes are given at the bottom of the page with the text they refer to. They can contain less relevant details, additional explanations or used sources (e.g. scientific material, manuals). They cannot replace the cited literature.

The article should be accompanied with a cover letter with the information about the author(s): surname, middle initial, first name, and citizen personal number, rank, title, e-mail address, and affiliation address, home address including municipality, phone number in the office and at home (or a mobile phone number). The cover letter should state the type of the article and tell which illustrations are original and which are not.